# In-situ High-Energy Diffraction Microscopy Study of Zirconium Under Uni-axial Tensile Deformation

by

Jonathan F. Lind

Submitted in partial fulfillment of the
requirements for the degree of
Doctor of Philosophy
at
Carnegie Mellon University
Department of Physics
Pittsburgh, Pennsylvania

Advised by Professor Robert M. Suter

July 29, 2013

**Abstract**

The ability to predict a material's performance while being subject to complex thermo-mechanical processing is of great importance for material design and implementation in the real world. A material's behavior and performance has been shown to depend on its underlying microstructure. Recent advances in x-ray-based characterization of bulk microstructures while in service has lead to validation and constraints of models used for predictive responses. Specifically the use of Near-Field High Energy X-ray Diffraction Microscopy (nf-HEDM) with Forward Modeling Method (FMM) to obtain spatially-resolved microstructures and microtextures has been a break-through in fully characterizing bulk metals in-situ. New advanced data processing methods have been applied to nf-HEDM diffraction images to assist in fidelity of microstructure reconstructions returned via the FMM. Here we present the development and results of one study of pure Zirconium as it is subjected to several states of uni-axial loading. The local feature tracking, including tensile twin nucleation and void formation, as well as global evolution is discussed.

# Acknowledgments

As any huge endeavor in life goes, it cannot be done without the help and assistance of countless friends, family, and colleagues. I wish to thank them all for the educational and emotional support that, without it, would have made this journey much less enjoyable. I would like to thank some of the more important components, and I hope that I have not left out any of the integral parts.

First I must thanks my parents, my brother, and my sister for being there and encouraging me from day one. I have the great privilege of parents, Carol and Joe, who were both always proud but never stopped expecting the best from me. Their exceptional work ethic has always been something I strive to emulate. I also had the great timing of being the youngest of three with both my brother, Joe, and sister, Jen, being great role models while growing up. I attribute lots of my intellectual abilities to having smart older siblings who kept me ahead of the learning curve for so many years.

I am also indebted to the fellow graduate students who provided the social fabric that made graduate school fun. Some of my fellow classmates, Megan Friend, Sam Rauhala, Cem Yolcu, Ricky Wong, and Chang-You Lin, who specifically were always there to chat about anything when procrastination was needed. Our adventures in Wean and off-campus made for great times. As these special people have all moved on, I am less saddened to depart.

Our broad base of collaborators at many different universities, national laboratories, and industry made grueling shifts during beam runs much more bearable. Conversations with these people in the materials community has helped give me an appreciation for the broader research field. I am glad to know I will see these colleagues again and again at conferences. The one collaborator who must be thanked specifically is Dr. Ulrich Lienert, whose presence at APS made it possible for the experiments envisioned to come to fruition. His personality, meticulous attention to detail when possible, and practical ability to compromise when not possible, made beam times incredibly efficient and also entertaining.

I cannot begin to express my gratitude toward the fellow graduate students in Professor Suter's research group who have had the most profound impact on my research development. I wish those that still remain, David Tan, Siddharth Maddali, and David Menasche, all the best with continuing the tough task of further advancing HEDM research. I must thank individually (but have little space to do it properly) those that have graduated from the group during my tenure, Reeju Pokharel, Christopher Hefferan, and Frankie Li. Our shared experiences during those beam runs really created a sense of camaraderie that I am not sure I will ever be able to reproduce. Reeju, your ability to juggle two bosses (still) is amazing to me. Heff, your skill at summoning random facts and spinning your own narrative has always been a source of amusement. Frankie, your insane work hours and technical ability have always been standards I aspire to.

How do I begin to thank my wife, Bridget? She is the woman who keeps me grounded. Without her influence in keeping me distracted from research and engaged in real life, I would fall into an endless research cycle that would be disastrous to my social and physical health. She has always been the one who I can turn to when things were not going well or want to turn to when its time to celebrate.

I owe a great deal of gratitude to my committee members, Dr. Joel Bernier, Prof. Steve Garoff, and Prof. Tony Rollett. The time commitment involved in cultivating and scrutinizing Ph.D. students is a (mostly) thankless job. But your efforts spent on me are deeply felt and deeply appreciated. Without them, I do not know where I would be right now.

Last but not least, a special thank you has to go to my thesis advisor, Prof. Robert Suter. I am extremely delighted that he took a chance on a student like me. I am also really glad that he is the kind of person with a great sense of humor; it has made our meetings much more amusing and usually much longer due to getting lost on random unrelated tangents. The rapport he has built with his students (not just me) made for excellent times, and for that, I am personally profoundly thankful.

Thank you all, so very much.

# Contents

# List of Tables

# List of Figures

# Chapter 1

# Introduction

The following brief introduction chapter is meant to motivate the bulk of the work presented here. The purpose is to broadly and briefly explain

1. why metals research is important
2. why microstructure research is necessary
3. ways in which microstructures are studied

3a. Near Field High Energy Diffraction Microscopy technique specifically

4. why plasticity is studied
5. and why specifically zirconium is interesting to study

Research into development of new next-generation metals requires a confluence of theory, simulation, experimentation, and characterization in understanding about metal properties so as to predict and control their behavior. Specifically, interest in structural materials has widespread industrial support through research and development. The study of metallurgy and material science has attempted to match physical phenomenology with physics-based models to explain material behavior. The earliest uses of alloys was driven by observation. Even now some materials research is driven by phenomenology with models attempting to predict observed material behavior. Materials research is currently seeing validation and extinction of theoretical models through advanced experimental methods. It is only through the merging of simulation and experiment that the predictive capability of these models can be fully be employed. Improvement in functionality of everyday metals can only come through research which is exactly why so many people study metals.

People depend and rely on structural materials constantly. The chair you sit in, the car you ride in, and the building you work in, to name a few examples, rely on the structural properties of metals to perform their intended function. Polycrystalline

materials are ones which are composed of many crystals (or grains) each with different orientations and sizes. The way in which this ensemble of individual crystals, defined as a microstructure, responds to stimuli has been shown to depend on the microstructure itself. Single crystal properties are routinely studied; however, the reason there is considerable interest in microstructure science is that the polycrystal does not behave as exactly like the sum of its parts. This tells us that the composition of materials to define their properties is important, but their microstructure cannot be neglected. The processing of metals, so-call "heat and beat" is done in specific prescribed ways to obtain desired microstructure properties (grain size, dislocation content, alloy content, texture, etc) that equate to desired macroscopic properties.

Until recently microstructure study was limited by the capability to characterize them. New characterization technique have allowed for probing how material properties are dependent on microstructure. Initial microstructure science involved simple optical microscopy to see grain structure and shape on surfaces. Techniques such as scanning electron microscopy (SEM), transmission electron microscope (TEM), and atomic force microscope (AFM) have allowed for more higher spatial resolution resolution studies of microstructures.

Orientation imaging microscopy (OIM), the ability to resolve the grain orientations in a microstructure, has only very recently been applied to the TEM and SEM. TEM-OIM is concerned with determining the orientation of very small microstructures($nm$ sized grain, $\mu m^2$ sized samples) thin film. Electron back-scatter diffraction (EBSD-OIM) in the SEM is slightly lower spatial resolution on a sample surface ($100nm$ and larger sized grains, $\sim 1mm^2$ sized surfaces). The former involves diffraction pattern through transmission, and the latter with surface back-scattered diffraction to determine crystal orientation. These techniques are extremely useful at revealing the grain structure and network. However, they lack the ability to probe the dynamics of grains in the bulk.

Even more recently, x-ray and neutron diffraction techniques have allowed for probing non-destructively in the bulk of polycrystalline materials. Neutron diffraction, due to large wavelength of incident beam of neutrons, lacks the ability to spatially resolve the grain structure. It is able to perform texture measurements on extremely large samples ($\sim m$). Neutron diffraction can observe texture evolution of samples without resolving the orientation of individual grains.

In the past ten years, several synchrotron-based x-ray techniques have been developed which take advantage of the ability of hard x-rays to penetrate bulk samples non-destructively to probe the grain structure. These techniques include Three-Dimensional X-ray Diffraction Microscopy (3D-XRD), Differential Aperture X-ray Microscopy (DAXM), Diffraction Contrast Tomography (DCT), and Far-Field High Energy Diffraction Microscopy (ff-HEDM). These techniques operate a different length scales to allow for 3D probing of a sample volume non-destructively. These characterization probes while still in their infancy, have the capability to measure the underlying grain structure of a material while performing dynamical experiments. As

they continue to develop, they should be able to constrain material models while complementing other material characterization methods.

Another synchrotron x-ray technique developed for studying microstructures is Near-Field High Energy Diffraction Microscopy (nf-HEDM). It is a rotating crystal method using a monochromatic planar focused x-ray beam which utilizes a series of small ($\sim 5-10$) detector-plane-to-rotation-axis distance. A sample plane is defined by the plane of the beam. The sample is rotated to bring crystals into Bragg diffraction conditions which is collected on the CCD camera through a series of small angular integration step. Samples are typically ($\sim 1mm$) due to the penetration depth of high energy x-rays (50–100keV). A typical sample plane is measured, the sample is translated perpendicular to the beam plane, and successive planes (or layers) are measured. Coupled with the Forward Modeling Method, nf-HEDM is able to produce layers of spatially-resolved orientation maps at a resolution of $\sim 1\mu m$. The author has been intimately involved in its development and will focus on its recent development in the coming chapters (see Chapter 2).

One important study of structural materials is plasticity which is the phenomena when a material fails to return back to its original shape after forces are released. To the physicist, this is what happens when one goes beyond the limit where Hooke's Law applies. Plastic deformation is a permanent change in the lattice whereas elastic deformation is completely reversible. Preventing and controlling the on-set of plastic deformation is one important goal of structural materials research. The recently developed x-ray techniques including nf-HEDM have the ability to measure microstructures at the on-set of plastic deformation. Chapter 3 describes one experiment which demonstrates the capability and sensitivity of studying 3D deformation using nf-HEDM.

The deformation experiment involves a series of uni-axial strain measurements of a zirconium microstructure non-destructively with nf-HEDM. Zirconium is studied because it is a model hexagonal close-packed (HCP) structure, exhibits strong crystal anisotropy, and has engineering applicability in the nuclear industry. Observing HCP deformation mechanisms in the bulk, spatially-resolved, and in 3D, will represent a first ever insight into how different bulk plastic deformation is to surface deformation. Comparison with simulation will be performed.

In the following chapters, focus will be placed on advances in the nf-HEDM technique and initial scientific output from this developing technique. One significant contribution to the advancement of the nf-HEDM technique will be discussed. The uni-axial zirconium strain experiment will be described in detail.

# Chapter 2

# Experimental Data and Image Processing

## 2.1 Introduction

The advent of the CCD camera and digital imaging has allowed for unprecedented speed in data collection. The term “data“ here can span a range from personal picture taking to surveillance data to scientific signal capture. In some cases, the image itself is the final step in the chain of data handling. In the case of experimental sciences, the images collected generally hold some signal which needs to be extracted. The image, or digital signal, is segmented accordingly to obtain whatever information it holds. The image is the beginning (or perhaps intermediate) step in a chain of processing meant to extract something meaningful about what is being studied.

This data pipeline flow with image processing as one of the initial steps requires robust processing. Without reliability at this stage, all results from here are jeopardized. At all costs, one wants to avoid the "garbage in, garbage out" [1] problem when dealing with 2D and 3D images. When months or even years worth of analysis might be invested into a single piece of data, initial handling should be done with care. Generally this type of analysis has been neglected by scientists who are uncomfortable or untrained in simple segmentation techniques. They naively hope that the effect will not change the results.

Access to higher quality image processing algorithms have been beneficial to the processing pipeline of near-field High Energy X-ray Diffraction Microscopy (nf-HEDM). The writer pessimistically sees many ways in which a nf-HEDM dataset can be corrupted. At the first stage, poor sample handling or choosing is where things can go wrong immediately and potentially never recovered even after months of time and effort are put in. If a high caliber sample is chosen, a poor or inexperienced Advanced Photon Source (APS) user could potentially collect terabytes (TBs) of unanalyzable data. At this point if everything has been done in a satisfactory way, simply put all that exists is a large stack of images with spots. At the current collection rate in a

given week of beamtime at the APS, roughly 1 million nf-HEDM experimental images can be captured leading to potentially 10 TBs of spot data.

Images are segmented a into collection of pixels representing a spot. The spots are cataloged and then input into FMM reconstruction algorithm. This step serves to select diffraction signal and filter out the rest. For this experiment, image segmentation serves as the first step in digital processing.

Each spot in the images corresponds to a part of the sample satisfying a Bragg diffraction condition. Collections of intensity coming from regions with the same orientation (grains) will project onto the camera giving a cross-sectional projection of the grain. These projections will tend to appear crushed or contracted vertically depending on which *(hkl)* crystal plane is diffracting. If put another way, the projection and location of the spot is a function of $2\theta$ which by Bragg's law is a function of the crystal lattice itself and the X-ray beam energy. As a simple case, imagine a circular grain of diameter, $d$, incoming beam such that $\hat{k_i} = \hat{z}$, $xy$-plane being the detector plane, and $\hat{k_f}$ completely in the $zy$-plane. See figure 2.1 for a visual schematic . From the viewpoint of the $zy$-plane, the diameter of the grain as seen in the $y$-direction is reduced to $d \times \tan(2\theta)$. However in the $xy$-plane the grain dimensions are still $d$. The grain with originally circular cross-section is projected on the detector plane as an ellipse with eccentricy,

$$\begin{aligned} e &= \sqrt{1-(\frac{b}{a})^2} \\ &= \sqrt{1-(\frac{d\sin(2\theta)}{d})^2} \\ &= \sqrt{1-\sin^2(2\theta)} \\ e &= \cos(2\theta) \end{aligned} \tag{2.1}$$

In this case, small-angle scattered (low $|\vec{Q}|$) will appear as high aspect-ratio ellipses on the detector. As $\{2\theta, |\vec{Q}|, (hkl)\}$ all increase, eccentricity decreases and the projection of the circular grain appears more like a circle. Due to the scaling of shape along the $y$-direction by $\tan(2\theta)$, shape sensitivity along this dimension suffers by a factor of $\frac{1}{\tan(2\theta)}$. As $2\theta$ becomes large, the $x$- and $y$-dimensions become commensurate. More accurate shape information can be obtained from these projections at the expense of intensity decreasing as function of $|\vec{Q}|$. See figure 2.2 for experimental images of a circular cross-section grain.

In nf-HEDM, the 3mm x 3mm detector lies about 5mm downstream of the rotation axis. This effectively limits the observable diffraction $2\theta$ such that $2\theta \leq 30°$. For $2\theta = 30°$, $\frac{1}{tan(2\theta)} = 1.73$ represents the smallest compression factor for diffracted spots. Clearly the information density in the vertical and horizontal dimension of detector data in this configuration are not equal and should not be treated equally.

While information compression is one important aspect to consider when handling nf-HEDM images, another concerns contaminating experimental effects. One of the

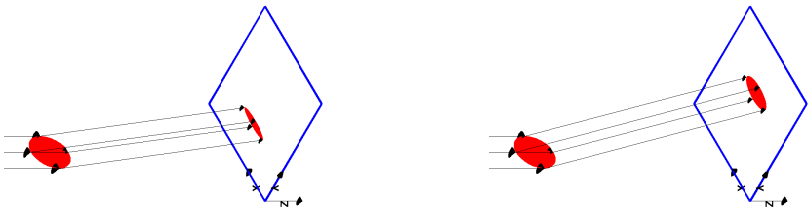

(a) (b)

Figure 2.1: (a) and (b) represent a schematic of the geometry of a circular grain and its diffracted projection on the camera. (a) corresponds to $2\theta = 10°$ and (b) corresponds to $2\theta = 20°$

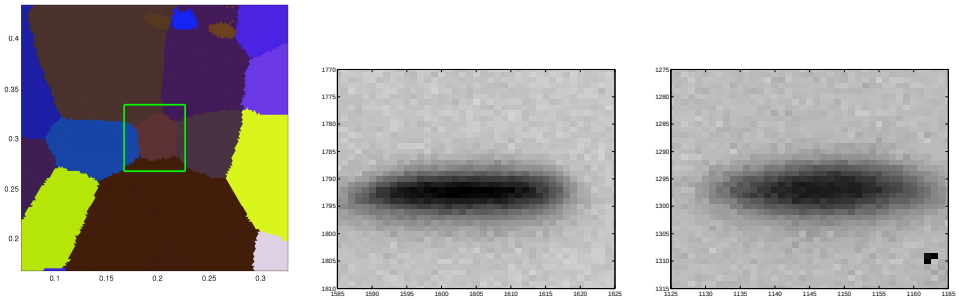

(a) (b) (c)

Figure 2.2: (b) and (c) are raw experimental Bragg peaks emanating from the boxed grain in (a). The grain here is roughly circular in this cross-section with a diameter of $\sim 50\mu m$. (b) corresponds to a $2\theta$ of about 8.5°, and (c) corresponds to 12.2°. Note the broader vertical extent of (c) compared with (b).

most noticeable of these effects is the broadening of peaks in the detector plane due to the finite thickness of the scintillating material. Experimental diffraction peaks appear broader in detector space, and their intensity profiles drop off gradually. The peaks appear to have a shadow that can extend further than the actual peak size. This widening of peaks is more dramatic as the intensity of the particular diffracted peak

increases. High intensity peaks will not affect their signal detection but will effect those nearby. Since these kinds of effects are peak dependent, they will not show up in any systematic way which is why they are deemed random errors. Uniform background subtraction will not help remove them.

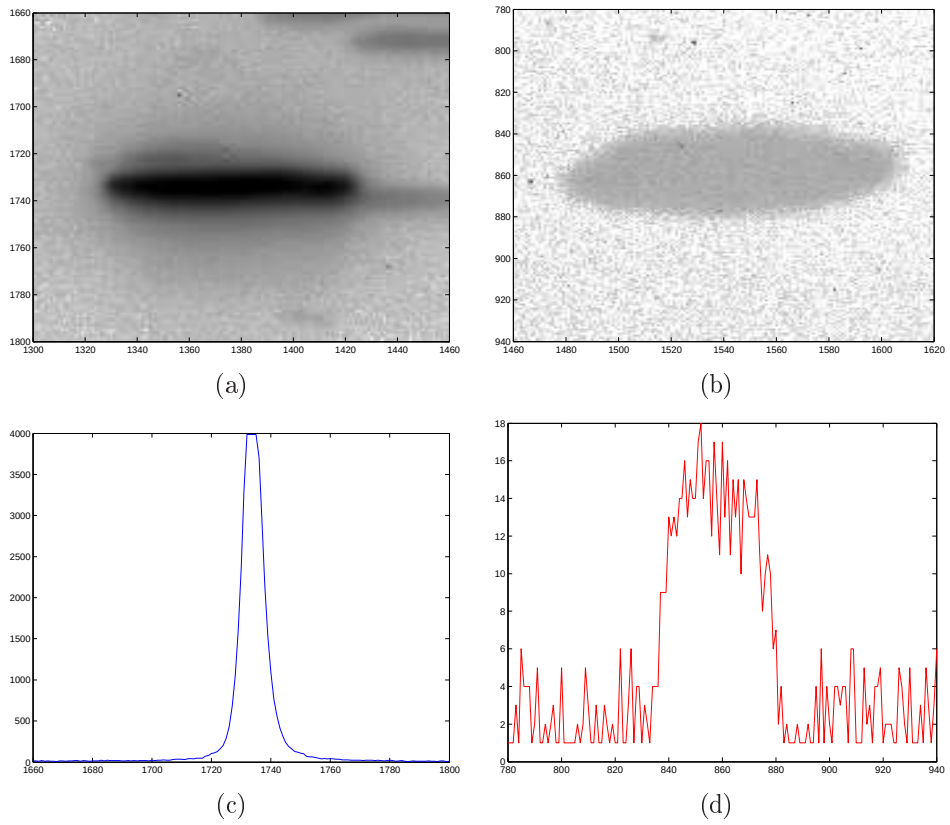


Figure 2.3: Presented here are two peaks from the same image, one of high intensity (a) and the other of low intensity (b). Note the intensity shadow present in (a) and absence in (b). 2.3(c) and 2.3(d) represent a single vertical intensity profile of these peaks. Intensity scales are much different for these separate figures.

This problem is further complicated by the fact that for a given image, high intensity scattered peaks can inhabit the same region of the detector as a low intensity peaks. The higher intensity peak has the potential to completely overwhelm the lower intensity peak and potentially be missed by segmentation routines. Separating these two peaks becomes more difficult the closer they are spatially on the detector and the larger the difference between their relative intensities. The experimental peak blooming generates a shoulder allowing for the collection of peaks to be merged into a singly categorized peak defined by the strongest peak intensity. The archipelago of peaks is classified as a single peak and much of the information of the weaker peaks is comprimised or lost. Corrections for these types of experimental but predictable errors need to be taken into account when processing experimental signals.

Other factors to consider when handling near-field images include material symmetry, grain size, and deformation level which all contribute to the number of peaks per image and consequently their likelyhood of overlap. Simply put, there is no single prefered way to handle signal captured from the nf-HEDM experiments. In general, there are no preferred segmentation algorithms that fit all problems best. Conversely the optimized algorithm which best suits one dataset might perform miserably when applied to even a similar dataset. Being able to define the general working space of a problem allows for the best tuneability of algorithm that is both robust and broad for a given problem. Incorporating common features of all collected data into processing algorithms will improve how well segmentation of near-field images proceeds but will not necessarily be fully-optimized for the specific dataset at-hand. This necessity to optimize is reduced by the fact that the Forward Modeling Method [2, 3] reconstruction is robust and less sensitive to image reduction routines as other polycrystalline x-ray reconstruction algorithms [4, 5, 6]. Still higher quality experimental inputs to the FMM will result in more detailed microstructural features that can be studied. Ideally optimal data processing algorithms would be produced for every collected dataset, however given the neglect in this area altogether, a generic approach is presented which is more robust, highly adaptable, and with higher throughput than previously used methods for nf-HEDM image processing.

The case for developing a robust, adaptable, and high throughput nf-HEDM image processing algorithm comes naturally from the fact that such large datsets are produced readily from samples with very different microstructural character. One needs to be fairly confident that given algorithms will work given potentially drastically different sample types and able to have results quickly so as not to slow down the data pipeline. Having high quality, quickly obtained, results from the near-field experiments allows for more time spent on scientific discovery and less on fundamental technique development.

## 2.2 Original peak extraction method

Until recently, little attention was paid to the subject of image segmentation as applied to nf-HEDM. Most of this was due to lack of resources and a focus on developing other aspects of the technique. As the nf-HEDM technique began to mature, some necessary compenents were reassessed. Initially the original method of image segmentation worked adequately. Initially components of the nf-HEDM analysis were functional but not optimal, and no single component of the nf-HEDM technique could be completely removed from the others for systematic study. As the technique developed, failings of specific components could be assessed independently. This led to the inevitable removal of the original image segmentation method.

nf-HEDM data collection can be described generically as a rotating crystal method [7] experiment. A polycrystalline sample is exposed to a planar monochromatic X-ray beam. A camera collects diffraction patterns as the sample is rotated in small

rotation intervals (typically $\delta\omega = 1^\circ$). Diffraction images tagged by rotation interval define reciprocal space mapping of each of the Bragg diffractions emanating from crystal planes. Typically 180 contiguous intervals are collected at a single rotation-axis-to-detector distance ($\sim$ 5mm). The detector is then translated downstream a few mm, and the same 180 interval measurement is repeated. The sample can then be translated vertically and another slice measurement made in the same way. Since many images are collected, a single pixel on the detector can be described by more than its physical location. One could specify it via P(S,z,L,$\omega$,x,y) where S is the sample investigated, z is the measured layer, L specifies the detector plane, $\omega$ specifies the rotation interval, and x & y are the location on the camera. While smaller individual rotation intervals are currently being used in some experimental setups with total number of intervals compensating to obtain a complete 180° sweep, we will henceforth call the collection of intervals for a complete 180° sweep at fixed detector distance, measured layer, and sample as "single detector distance."

Before processing of diffraction images proceeds, a simple background subtraction method is employed. A simulated background image is generated from the collection of intervals in a single detector distance. The median value of each (x,y) pixel position in the image across the entire interval defining the single detector distance is assigned back to that (x,y) pixel position in the simulated background image, defined in the algorithm 1. Simply put, the background image is purely a median image across the interval direction for a given single detector distance. Each image in this interval will then have the background image subtracted, removing the spatially-varying but $\omega$-independent portion unrelated to the diffraction measurement. These constant background counts are due to beam-block absorption and emission, beam-block diffraction, scintillator imperfections, detector electronic noise, ambient light, etc. Since these components are stable during the sample rotation, their contribution to background can reasonably be assumed to be constant. The median filter ignored high intensities due to sample diffraction as log as these are not spread over a large fraction of the $\omega$ range.

**Algorithm 1** Background creation

**for** $i = 1; i \leq nX; i++$ **do**
  **for** $j = 1; j \leq nY; j++$ **do**
    Bkg[i][j] = median( P(S,z,L,[$\omega_{start} \rightarrow \omega_{stop}$],i,j);
  **end for**
**end for**

Segmentation of individual images proceeds after background removal. The original method used can be classified as a cluster-based image thresholding segmentation technique [8]. For each image in a detector distance, each background-subtracted image is subjected to a 3x3 spatial median-filter smoothing operation. A small, $\sim 5$ count $= 2\sigma$ , amount is further removed which typically corresponds to the fluctuation in pixel count around its average. The dynamic range of the current detector

is a 12-bit CCD camera with range from 0 to 4095. At this point, this image is binarized labeling pixels above 0 as lit (1), and the rest as background (0). Spatially-connected clusters of lit pixels are assigned unique labels. Of the pixels in each cluster, thresholding by some factor of the cluster maximum intensity is performed leaving only those pixels above the specified threshold. The value typically used ranges from $0.02 \rightarrow 0.25$ with 0.25 being a more restrictive reduction parameter. The remaining pixels are written out as a list giving location (x, y), intensity, and cluster ID. See algorithm 2 for implementation details. This method is considered one of the simplest methods of image segmentation and generally occurs as the first example of segmentation in standard image processing textbooks [9].

**Algorithm 2** Image segmentation

```
nBaseSub = 2σ;
fThreshPercent = 0.10;
for i = ω_start; i ≤ ω_stop; i++ do
    Im_sub = Im_i - Bkg;
    Im_base = Im_sub - nBaseSub;
    bIm = Im_base > 0;
    vListClusters = ConnectedComp( bIm );
    vAcceptedPixels = [];
    for j = 1; j ≤ nNumberOfClusters; j++ do
        nThreshVal = fThreshPercent * max( vListClusters[j].Pixel[:] );
        for k = 1; k ≤ vListClusters[j].Pixel.length(); k++ do
            if vListClusters[j].Pixel[k].Intensity > nThreshVal then
                vAcceptPixels.Add( vListClusters[j].Pixel[k].{x, y, Intensity, ID} );
            end if
        end for
    end for
    WriteToFile( vAcceptedPixels );
end for
```

A list of above threshold pixels is generated for each image collected experimentally. Depending on a lot of different factors (sample size, sample symmetry, grain size, single rotation interval sizes, deformation level), the images produced will vary in how sparse or dense they are in spot data resulting in accordingly small or large pixel lists returned. Even in cases of abundant numbers of spots, list data will at its largest size still take up less than 10% that of full image data. This is one reason for processing the nf-HEDM images and why these lists are commonly referred to as "reduced data". For an single image which is typically $8MB$, its reduced data can range from $40kb \rightarrow 800kb$. This algorithm was originally implemented in Matlab by former research group member S.F. Li (following earlier work by C. Xiao and D. Hennessy) with processing of images taking varying amounts of time to process depending on the sample character.

As illustration, see figures in 2.4 for visual examples of the data processing pipeline. The two examples provided here include an image with relatively sparse spot population from a $30\mu m$ diameter gold wire, and another with more dense spot population from a $\sim 1mm$ diameter zirconium wire. Clearly the segmentation does well in both cases when comparing segmented reduced image with the raw image. The occurrance of accidental overlapping or connecting peaks is much less frequent in the gold case because the number of peaks is much smaller. Figure 2.4(e) is not an example of a severally overlapping peak case, but merely a demonstration of the variety of complexity of collected images. A more extreme case would required more attention to local image features rather than complete images shown.

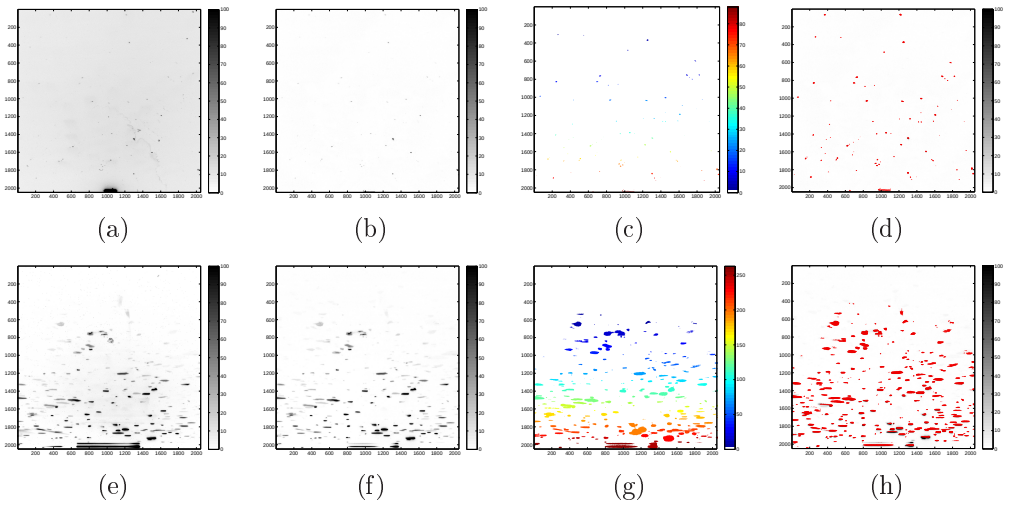

Figure 2.4: (a) shows the raw nf-HEDM image from a single interval of $30\mu m$ diamter Au wire. (b) shows the same image after background subtraction and median filtering. (c) shows the image after binarization and connected component labeling. Distinct colors represent uniquely labeled spots or peaks. (d) shows the background subtracted image overlayed with red dots for every point which is part of the reduced data. (e)-(h) represents a similar dataflow for a $\sim 1mm$ diameter Zr sample.

This image analysis method survived for many years by being suffient at the early stages of development for nf-HEDM. Initially many of the components for the measurement and analysis were constructed in an ad-hoc way because of the necessity of having them in place. The number of samples measured, diversity of sample character, and overall number of slices measured per sample greatly increased when experimental proceedures improved and data reconstruction became more reliable. Only when reconstruction of simple materials could be verified and produced quickly were more complex measurements undertaken. These more extreme cases showed the robustness of the technique, but clearly showed the failing of the image processing to that point. Data is now being collected at a more rapid pace with more complexity. Data collection went from $\mathcal{O}(100Gb/year)$ to $\mathcal{O}(5Tb/year)$. From an engineering standpoint, the

$50x$ increase in raw data called for faster data processing which is later accomplished via code porting and parallelization, the more complex samples measured required the processing to be highly adaptable to varying diffraction patterns, and the recognition of this method's failure modes required more robust handling of images.

## 2.3 Motivating a new approach

The main reason for robust orientation reconstruction from the Forward Modeling Method lies in the number of signal projections used per orientation resolved [3]. For an incorrect orientation to be accepted purely from noise instead of signal is highly unlikely from the noise. If we assume the noise to be mostly random, having 100+ projections match physically significant scattering from a specific orientation would be vanishingly unlikely unless many things which are not signal peaks are mislabeled.

At this point a stastical treatment of peaks in nf-HEDM diffraction images is needed. For segmentation routines, there exist two failure modes, the false positive (type-I) and false negative (type-II). The false positive is when a pixel or group of pixels is classified as a peak when that region does not have any actual diffraction signal. This is when background or noise is classified as signal. The false negative is the failure to classify a pixel or group of pixels as a peak when that region does have actual diffraction signal. This is when a diffraction signal is not picked out of the background. Both refer to misclassification of pixels which both can have negative impact on orientation reconstruction. However, assuming their penalty is equal is incorrect.

The Forward Modeling Method has been shown to be much less sensitive to type-I than type-II errors [3]. This knowledge allows for relaxed conditions regarding accepted peaks. It is extremely unlikely enough type-I errors will result in a single high caliber (high confidence) orientation to be selected even if no other better solution exists. This does not give one carte blanche to indiscriminatly accept all pixels that could even remotely be signal.

The best way to explore how these errors occur would be to draw from experiences. Type-I errors tend to come from over-estimation of peak extent rather than as inclusion of independent blobs. While the description of peak shape extent is not rigorous and completely debatable, there are cases where fluctuations in the background are larger than the prescribed intensity cutoff leading to regions being erroneously classified as peaks. See figure 2.5 for an illustration of this experimentally. These misclassifications of background as signal will most likely be ignored because it is not consistent with any actual sample scattering and is completely random in nature.

Type-II errors tend to come from merging of peaks and under-segmentation which results mainly where there is strong peak overlap in experimental images. Figure 2.5(b) shows a case of this kind of error where a peak is completely lost due to spot overlap. These seemingly separate peaks are merged as a single connected component by the original segmentation routine and reduced as prescribed. Due to the described

shadowing effects, in some cases several peaks will tend to be clumped together as a single connected component, and since the shadowing occurs around higher intensity peaks, most of the information of unintentionally connected peaks is lost.

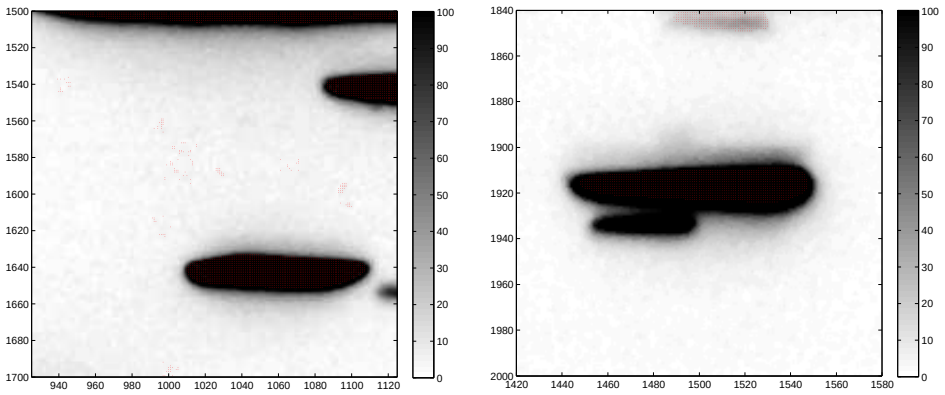


(a) (b)

Figure 2.5: Illustration of two types of errors, (a) for Type I-error and (b) for Type II-error. (a) shows pixels labeled as peaks which come from shadows produced from stronger peaks. (b) shows two clearly separate peaks which have overlap on the detector and are merged in the segmentation routine. Since one of the peaks is much higher in intensity, all information from the other peaks is lost when thresholding is performed based on the stronger peak's intensity. In less dramatic cases where intensities are not so disproportionate, the shape of the the weaker peak will be misrepresented. Here red dots represent pixels classified as signal that will be kept in the reduced data.

Next we would like to quantitatively study how these errors might affect reconstruction results. While Fig 2.5(a) is an illustration of this type of signal misclassification, its effects are minimal due to the fact that they are not systematic. Since these effects come from the experimental setup (scintillator thickness, focusing optics) and all peaks are processed in the same way, peak size over-estimation can be a systematic error. For example, in the original method method of segmentation *Image Segmentation*, lowering the threshold fraction parameter ($fThreshPercent$) from say $0.25 \rightarrow 0.10$ would have the effect of increasing the size and shapes of every diffraction spot. In an effort to study how that will change grain shape and sensitivity, a synthetic circular grain's scattering was simulated and then peaks allowed to grow by marching out. The position and uncertainty in the grain's boundary were analyzed as a function of peak growth (see figure 2.6).

The coupling between grain size and spot size is seen clearly in Fig 2.6(c) where the spot growth amount correlates to size of the grain with 100% spot overlap (red curve). Figure 2.6(d) shows the spot overlap for extreme cases of no dilation and large dilation. For no dilation, the falloff of the spot overlap can be attributed directly to discretization of scattering data onto a pixelized camera. Effectively the pixel size

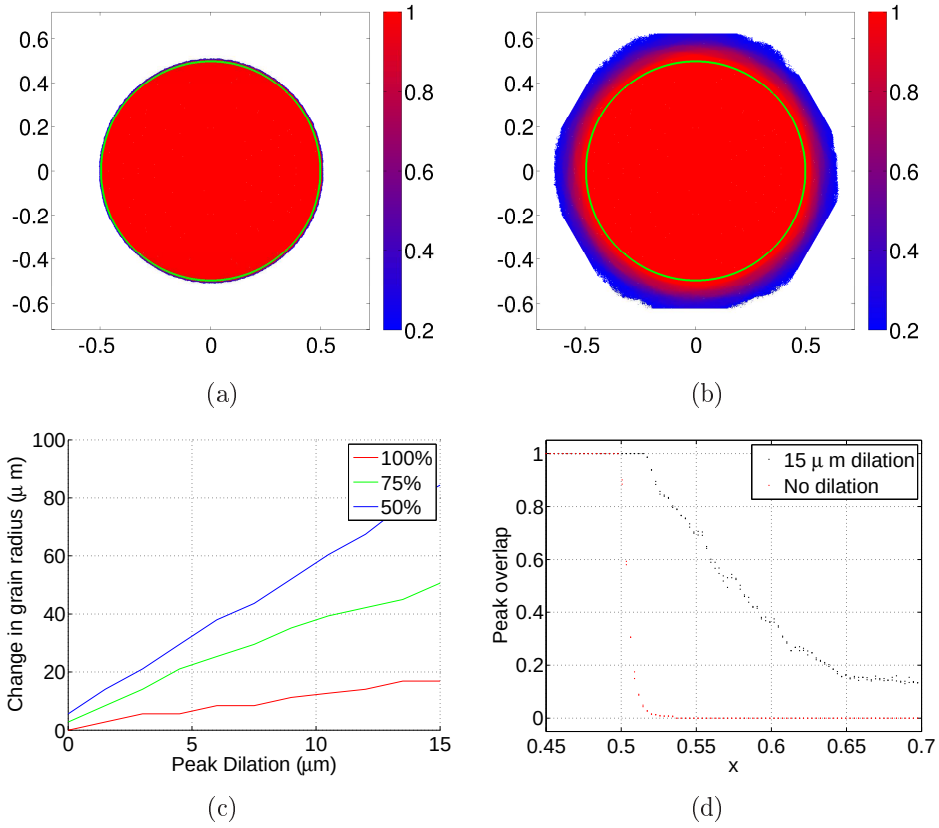


Figure 2.6: Simulation involving a single 1mm diameter grain (similar to one described in figure 2.1) and how its extent is dependent on peak definition. (a) shows the confidence map based directly on the simulated scattering. (b) shows the same plot as (a) with all experimental peaks enlarged by $20\mu m$. The green circle shows the original extent of the grain. (c) shows the measured diameter at each dilation step at different criteria of overlap. When all peaks grow $15\mu m$, the grain grows by that amount with complete coverage of every simulated peak. It grows more than $100\mu m$ if one considers 50% overlap as acceptable, for example. (d) shows the extent of fuzziness, or spatial drop-off, that an orientation can have if peaks are too liberally defined.

determines the lower bound for resolving a microstructure edge. For large dilation, the edge moves by that amount but also the resolving ability for that edge becomes smoothed out.

Seeing the location of boundaries move as peaks are dilated, their uncertainties also increase with dilation. Figure 2.7 shows evolution of boundary width in smaller dilation steps from start to finish as introduced in Fig 2.6(d). Quantifying this width by full-width half-maximum (FWHM) of the confidence parameter, $\mathcal{C}$, versus dilation amount produced figure 2.7(b). $\mathcal{C}$ is just the ratio of experimentally observed pixel to

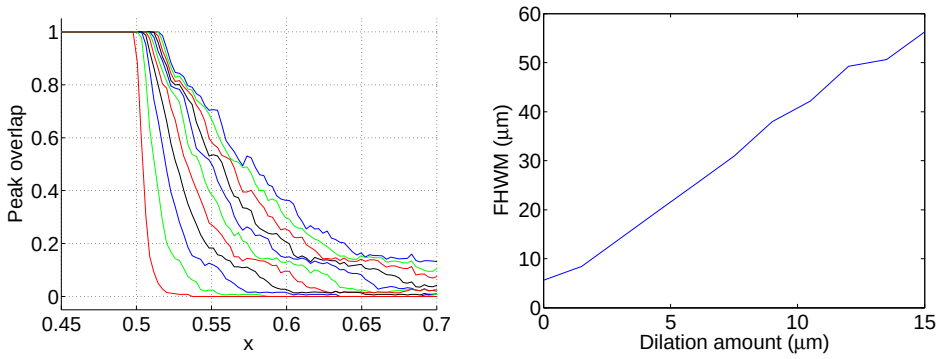


(a) (b)

Figure 2.7: (a) Extension of figure 2.6(d) showing the grain interfacial extent for various levels of peak dilation. The narrowest red profile corresponds to no dilation with each successive profile representing $1.5\mu m$ steps in peak dilation up to a total of $15\mu m$. (b) Shows the FWHM of the boundary as a function of dilation.

those simulated. In the study, the interface position moves proportionally to the dilation amount, and the interface width grows roughly $4\times$ that of the dilation amount. The factor of 4 results from a uniform dilation being performed while peak shapes are reduced in vertical size by a factor $\tan(2\theta)$ when producing diffraction spots. Therefore in cases of small-angle scattering for dilation amount $d$, the interface can appear to grow by an amount $\frac{d}{\tan(2\theta)}$.

Now quantification of the result of type-I errors result on interface position and width has been performed. A similar simulation is performed looking at type-II errors which corresponds to lost signal (see figure 2.8 for details). Fig 2.5(b) shows a case where two peaks are merged but only one is classified due most likely to large differences in scattered intensities. If two overlapping peaks (P1 and P2) are represented by their maximum intensity values ($P1_{max}$ and $P2_{max}$ such that $P1_{max} > P2_{max}$), if $P2_{max} < fThreshPercent \times P1_{max}$, then none of the pixels in P2 will be classified as lit, and P2 will not be included in the reduced data. In the case where $P2_{max} > fThreshPercent \times P1_{max}$, P2 is still measured against $P1_{max}$, which will gives P2 an effectively larger threshold percentage ($fThreshPercent_{P2,effective} = \frac{P1_{max}}{P2_{max}} \times fThreshPercent$). This will have the effect of decreasing the size and shape of those diffraction spots, or in extreme cases removing those diffraction spots.

This analysis was extended to look at simulated grain boundary movement for a bicrystal as either set of crystals peaks were dilated or eroded. The position of their interface (expected grain boundary) is studied by taking two crystals and varying the level at which either's peaks are eroded or dilated, . This is defined to be the position in the sample where the ratio is are equal for both grains. Figure 2.9 shows the erosion on one set of peaks and dilation on another affecting the position of grain boundaries. One notable result is that minimal movement of the grain boundary

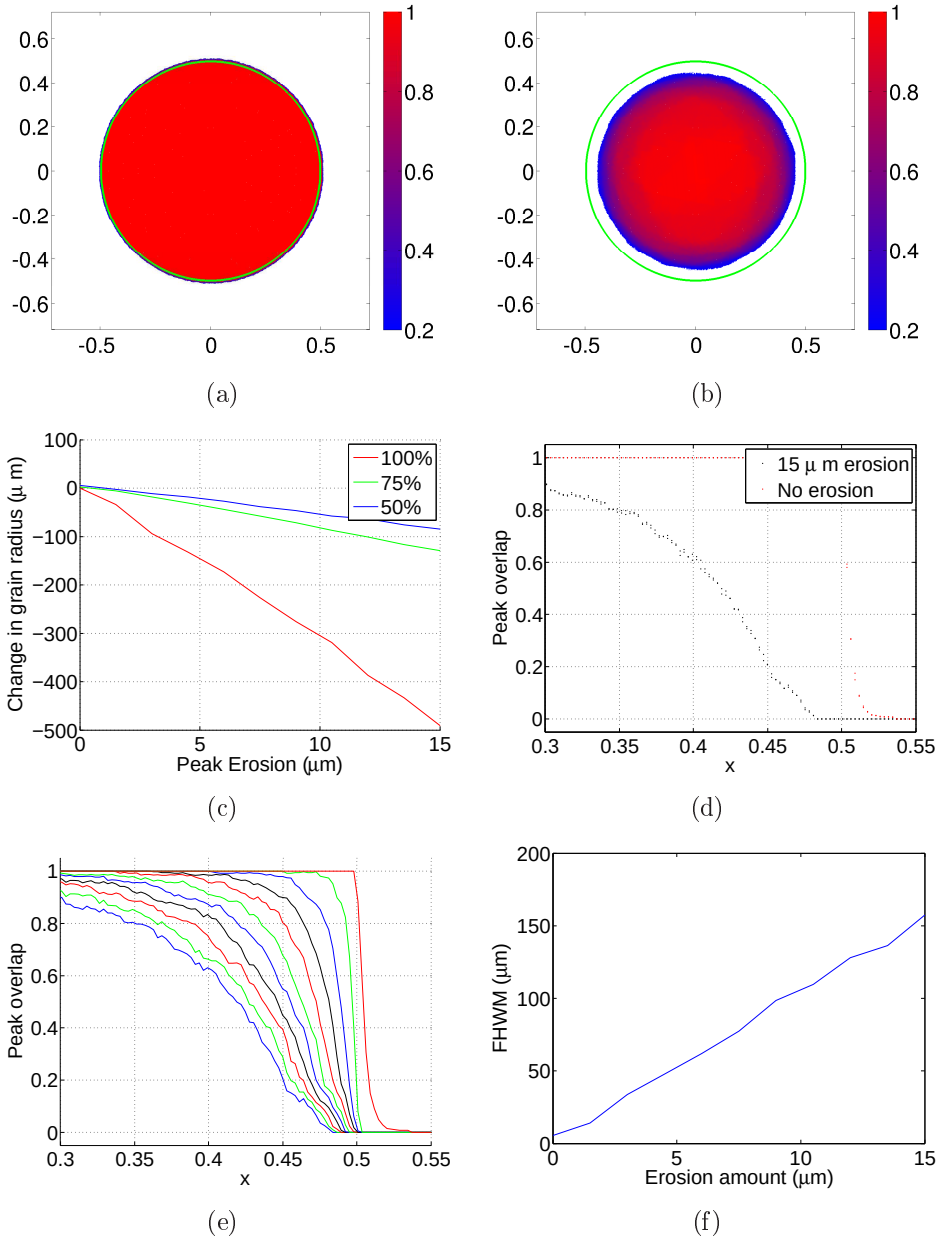


Figure 2.8: Analysis comparable to figures 2.6 and 2.7 except uniform erosion is performed.

from expected position is found when all peaks are processed in a similar way (both dilated or both eroded), and divergence in position occurs when processing varies (some eroded while others dilated). This seems to point to a conclusion that with constrained and consistent shape definition low variation in grain boundary position is obtained, and therefore accurate microstructure shapes are reconstructed which are

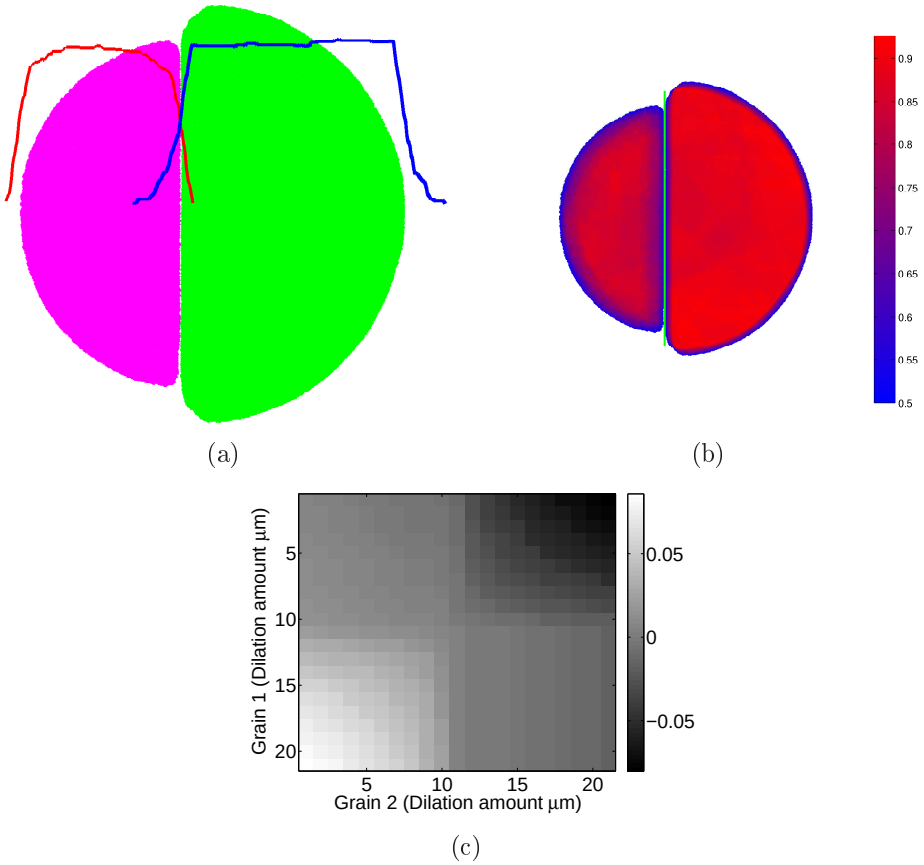


Figure 2.9: (a) represents a bicrystal where the peaks of the pink grain (Grain 1) have all been eroded by $7.5\mu m$ and the green grain (Grain 2) peaks dilated by that amount. The overlayed red and blue profiles represent the line profile of $\mathcal{C}$. (b) shows this ratio with a green vertical line representing the crossing of the two overlap profiles which should correspond to the interface (or grain boundary). (c) represents the movement of the interface as a function of erosion or dilation of either Grain 1 or Grain 2. (a) & (b) correspond to a single tile in (c). Scale is in $mm$ moved.

not artifacts of image processing

We find that this type of failure mode, under-estimate of merged peaks, is most common with nf-HEDM images processed in the way described by *Image Segmentation*. In the case of no spot overlap or intersection, *Image Segmentation* works with very minimal problems. When peak density in images increases, spot overlap and subsequent merging will happen. This can happen for many different reasons; for example fine-grained materials, low-symmetry materials, operating at higher X-ray energy, higher grain defect content. One further complication is that peaks of differ-

ent $|\vec{Q}|$ can intersect in near-field images. In the case of far-field scattering images, spots lie on rings of constant $|\vec{Q}|$ (Debye-Scherrer rings), and spot overlap generally occur only on these rings. Since the intensity of peaks varies with $|\vec{Q}|$, near-field images can have spot overlap with greatly varying scattering intensities. Far-field image analysis might be able to recover easily from overlaps because of this constraint that overlapping peaks be on similar intensity scales. The shadowing issue already described earlier coupled with high peak densities and varying intensities of merged peaks leads to clustering of experimental signal which is difficult to segment using *Image Segmentation*. Unfortunately small $2\theta$ peaks are more frequently subject to overlapping other peaks making them more likely to be poorly represented in the reduced form, and they suffer further due to shape amplification issues due to $\frac{1}{\tan(2\theta)}$ compression.

There are two ways to mitigate the current segmentation shortcomings which involve human intervention by way of tweaking the two available parameters of the current segmentation routine. They are

1. lowering $fThreshPercent$ to a very small number (<0.02). However, this also has the effect of lowering $fThreshPercent_{P2\rightarrow N,effective}$ for all peaks which are clustered together. This has the effect of retaining almost all intensity above background at the cost of marking all peaks artificially larger than their true extent. Further since the clustered peaks are still not segmented, each peak is represented by differing effective shape-defining parameters. This operation amounts to the case of peak dilation detailed earlier with uncertainties in the shapes/boundaries present. The only positive to this method would be that a completely filled-in reconstruction would be returned. The downside is that one hopes that correct boundaries are chosen due to the signal-averaging done during reconstructing using 100's of projections. A tell-tale sign of using this correction would be that grains on the outer edge of samples extend out much further than the physical limit of the sample and there will be minimal reduction in $\mathcal{C}$ on the grain boundary network.

2. raising $nBaseSub$ to remove intensity bridges that connect peaks. This has the effect of removing weaker signal that is present to be able to potentially segment connected peaks. Those peaks which remain, if assuming they are completely segmented, will be defined by a consistent shape-defining parameter for each peak at the cost of missing experimental peaks. This strategy does not fully work as some peaks may be connected by intensities that are more than 100 counts above background. Raising $nBaseSub$ this high would remove a significant amount of the experimental signal. Raising this value also puts an effective upper limit on $|\vec{Q}|$-space which can be searched. Both orientation and spatial resolution would suffer as a result of lost high-$|\vec{Q}|$ scattering.

Neither of these solutions are acceptable because they offer a loss in grain shape sensitivity or orientation resolution.

One final discussion to be made regards further peak segmentation. For example in FCC twins, one will typically see striations in scattered peaks where dips in intensity correspond to the twin regions not satisfying the Bragg condition while the parent grain does. If the segmentation is insensitive to these intensity variations due to twin structures, the segmented peaks will correspond to the grain shape of the parent grain as if no twins were contained within. The user of FMM for nf-HEDM reconstructions relies on some decreases in intensities due to twins within parent scattering along with extraction of finer twin peaks and the robust character of FMM algorithms to be able to faithfully choose between parent and twin. The development of intensity-based FMM reconstructions would mitigate this problem, but this discussion is beyond the scope of this work. Being able to distinguish internal structure of peaks has the potential to make resolving internal grain structure much easier for FMM algorithms. In this way, better segmentation routines are complementary to FMM and its reconstruction results. Clearly a better representation of the raw scattering data in reduced form should lead to a more accurate microstructure representation.

At this point it should be agreed that effective segmentation is necessary for high quality FMM reconstructions. As image reduction is the first step in the data pipeline, the need for automated and robust algorithms to process scattering images is essential to accuracy of microstructure results. Through simulation of changes in diffraction spot sizes, reduction in peak shape or even missed peaks can lead to drastically different grain shapes. We have discussed how type-II errors more negatively affect FMM algorithms, and how the current image segmentation algorithm is prone to these kinds of errors. In the next section, we will discuss an improved method for nf-HEDM image segmentation and its results on microstructure reconstruction.

One can pinpoint the motivating factor in developing newer image processing for nf-HEDM. This occurred when a reconstructed grain (from experimental data) was used to produced its simulated scattering pattern. It was found that a few of its low-$|\vec{Q}|$ peaks were not present in the reduced data, but they were present when one looked in the raw images. This failure at the image segmentation step seemed like it could be limiting the resolution of the FMM algorithm. Finally, a study of deformation in low symmetry (HCP) zirconium (see Chapter 3) was performed which further necessitated more advanced image segmentation of nf-HEDM scans.

## 2.4 A new peak extraction method

In the previous section, many of the shortcomings of the simple thresholding image segmentation as applied to nf-HEDM images were pointed out. In an effort to address those problems, the following items represent what a more robust reduction routine would take into consideration.

1. Ability to detect local variations. Weaker peaks that are caught in the shadow of strong peaks should detectable this way.

2. Concept of peak is necessary. Since grain/subgrain shapes are what is being looked at, the concept of space-filling closed-contours should be respected.

3. Minimization of the number of tunable parameters. A fully-automated reduction routine is desired that requires little human intervention. Results should not depend much on various variables.

4. Incorporation of scattering geometry. Taking into account that peaks are compressed in the image vertical direction will allow for better vertical peak sensitivity.

5. Need to process faster. A newer algorithm most likely will be more time consuming per image, and more images being collected per run/sample/year. Any way to keep image processing from becoming a bottleneck in the data pipeline should be explored.

Many advanced segmentation techniques were tested on nf-HEDM images, but in most cases with little success. A variety of methods were pursued including but not limited to mutual information, watershed, and level set methods with varying degrees of success. No attention will be payed to these algorithms as they were unable to satisfy the above items after initial testing. In the future, these methods after more careful study could replace what will be presented here but until they can be proven to be an improvement, they will be abandoned.

To incorporate local variation on peak detection, the class of gradient-based edge detection segmentation routines was investigated. These include Canny, Sobel, Prewitt, Roberts, and the Laplacian of Gaussians [10, 11, 12] and many more which are all similar in their ability to estimate where edges exist from taking the gradient or laplacian of an image. Depending on the approach, some prefer to use on the gradient since it is less sensitive to image noise. Edges are then defined by regions of maximal gradient magnitude and direction. In nf-HEDM images, boundaries between background and diffraction signal is the edge that needs to be detected.

### 2.4.1 Laplacian of Gaussian Implementation

The Laplacian of Gaussian (LoG) edge detection falls into a category of blob detectors. It incorporates the laplacian of the original image to find edges and so is more susceptible to image noise. This is purely due to the fact that numerical derivates are taken, and each successive one will be more sensitive to fluctuations due to noise. To minimize the effects of image quality, a convolution of the image with a Gaussian is performed on the image initially with a smoothing kernel ($\sigma$). Then the laplacian is operated on the resulting image ($\bigtriangledown^2 Im$). The image is further binarized by taking zero-cross contours which correspond to edges. The zero-cross of the LoG is called a blob detector because the zero contours produced in the binarization stage gaurantee closed contours around objects (blobs).

The only tunable parameter in this method would be the gaussian kernel which sets the scale at which edges can be detected. In an effort to remove reduction parameters, one can use $\sigma = 0.75$ pixels to achieve minimal smoothing with a kernel which is effectively smaller than results from the initial median filter process. Results do not vary much with changing the gaussian width especially given edges are only returned at integral positions.

One interesting incorporation that can improve edge detection would be weighting the horizontal component of the laplacian $(\bigtriangledown^2 Im)_{xx}$ by $\frac{1}{tan(2\theta)}$ to make x-direction edge transitions of similar numerical value as y-direction edges. Currently edge detection along the vertical direction is much stronger than the horizontal direction due to the small angle scattering geometry described.

Finally this data reduction routine was implemented in C++ using the image segmentation library Insight Toolkit (ITK) [13] which provided a much faster framework than Matlab. Initally it was implemented and tested in Matlab, but the desire for performance demanded that it be written in a compiled language. Further, the code was parallelized using the Message Passing Interface (MPI) [14] to take advantage of high performance computing (HPC). Given that each image is segmented independently from the rest, the code is parallelize by image meaning each processor in a working group segments an allotted list of images.

Algorithm 3 is the modified form of the new segmentation algorithm with zero-cross LoG added filter (algorithm 4). Examples in one dimension are shown in section 2.4.2.

The new implementation still retains reduction parameters $nBaseSub$ and $fThreshPercent$ for mostly legacy reasons. Table 2.1 shows for a given experimental dataset ( a low solvus high refractory [LSHR] nickel superalloy) the number of accepted peaks and pixels as $nBaseSub$ and $fThreshPercent$ were varied in both the original reduction and newly implemented LoG reduction. The main purpose of this table is to point out that the average size of reduced peaks remains relatively stable for the LoG reduction as compared to changes in the original reduction. Since the average size of peaks $(\frac{N_{pixels}}{N_{peaks}})$ can be directly linked to the grain size distribution, variations in reduction parameters should keep this value constant but cause more or fewer peaks to be accepted. Going futher, figure 2.10 shows a zoomed-in region of the segmented image for each of the three baseline values in 2.1. The pixels returned from the reduction algorithm are a subset of those contained in figure 2.10(g). The LoG binary segmented images appear to be less sensitive to baseline changes. The table also reflects this fact. Clearly the reduction parameters do not define the character of a peak in the new LoG reduction scheme

A quick note needs to be inserted here to understand the speed-up involved with porting reduction code from a Matlab version to C++ version. The original algorithm took $\sim 5s/image/processor$ in Matlab compared to $\sim 1s/image/processor$ in C++. The new LoG algorithm takes $\sim 65s/image/processor$ in Matlab compared to $\sim 5s/image/processor$ in C++. While the newer algorithm is more computationally

**Algorithm 3** Zero-Cross Laplacian of Gaussian-based Image segmentation

```
nBaseSub = 2σ;
fThreshPercent = 0.10;
for i = ω_start; i ≤ ω_stop; i++ do
    Im_sub = Im_i - Bkg;
    Im_base = Im_sub - nBaseSub;
    Im_LoG = ZeroCrossLoG( Im_base );
    bIm = Im_LoG > 0;
    vListClusters = ConnectedComp( bIm );
    vAcceptedPixels = [];
    for j = 1; j ≤ nNumberOfClusters; j++ do
        nThreshVal = fThreshPercent * max( vListClusters[j].Pixel[:] );
        for k = 1; k ≤ vListClusters[j].Pixel.length(); k++ do
            if vListClusters[j].Pixel[k].Intensity > nThreshVal then
                vAcceptPixels.Add( vListClusters[j].Pixel[k].{x, y, Intensity, ID} );
            end if
        end for
    end for
    WriteToFile( vAcceptedPixels );
end for
```

**Algorithm 4** Zero-Cross Laplacian of Gaussian

```
ZeroCrossLoG( im ){
    im = GaussianImageFilter( im, σ=0.75 );
    im = LaplacianImageFilter( im );
    im = im < 0;
    return im;
}
```

expensive, it is currently on par for processing time with the original reduction as originally implemented and run in Matlab. One final note is multi-core processing in Matlab is (at least as of now) is restricted to using a maximum of 4 processors at one time. The MPI-C++ version can theoretically run on as many cores as available, but is restricted at the point when the entire scan can be processed by all processors faster than a single processor can generate statistical background images. If all background images already exist, then the parallelized algorithm can run on $N_\omega$ (number of images per scan) cores at most since each core must reduce at least one image.

A few minor points should be made here which are that the original segmentation algorithm and the LoG segmentation algorithm are effectively the same except for the use of the zero-cross Laplacian to further segment the processed image. This has the effect of guaranteeing that any image processed by the new

| $nBaseSub$ | $fPercentThresh$ | Original | | | LoG | | |
|---|---|---|---|---|---|---|---|
| | | $N_{peaks}$ | $N_{pixels}$ | $\frac{N_{pixels}}{N_{peaks}}$ | $N_{peaks}$ | $N_{pixels}$ | $\frac{N_{pixels}}{N_{peaks}}$ |
| 5 | 0.05 | 100k | 25.5M | 255 | 325k | 20.2M | 62 |
| 5 | 0.10 | 100k | 19.9M | 199 | 325k | 19.1M | 58 |
| 5 | 0.25 | 100k | 11.8M | 118 | 325k | 15.3M | 47 |
| 10 | 0.05 | 93k | 16.7M | 180 | 180k | 14.2M | 79 |
| 10 | 0.10 | 93k | 13.7M | 147 | 180k | 13.2M | 73 |
| 10 | 0.25 | 93k | 8.7M | 94 | 180k | 10.2M | 57 |
| 20 | 0.05 | 75k | 9.8M | 131 | 108k | 8.7M | 81 |
| 20 | 0.10 | 75k | 8.3M | 111 | 108k | 8.0M | 74 |
| 20 | 0.25 | 75k | 5.5M | 73 | 108k | 6.0M | 56 |

Table 2.1: Comparison of number of peaks and pixels returned from original reduction and new LoG reduction on an entire 180° scan as $nBaseSub$ and $fThreshPercent$ are varied. This test was performed on images from a fine-grained deformed LSHR sample.

method will automatically have more segmented peaks than processed the original way ($N_{peaks_{LoG}} \geq N_{peaks_{Original}}$). Because of the second phase of segmentation in the LoG algorithm, the number of possible pixels that will be accepted into the reduced data is smaller than from the original reduction. The LoG step serves as a second refinement removing more potential signal but retaining only those pixels that are considered signal by more than just being above background. These pixels have some differential feature that distinguishes them from the background. In this way, one might expect the LoG reduction to contain fewer pixels in reduced form ($N_{pixels_{LoG}} \leq N_{pixels_{Original}}$) ignoring the nature of these pixels being more qualified because the binary mask of the LoG is by definition smaller than the original binary mask.

Table 2.1 shows that indeed for different reduction parameter values, $N_{peaks_{LoG}} \geq N_{peaks_{Original}}$. However, at low values of $fPercentThresh$, $N_{pixels_{LoG}} \leq N_{pixels_{Original}}$ holds because the original reduction is effectively keeping almost all pixels above the background. This ceases to be the case as $fPercentThresh$ is increased indicating that cutting off the tails of peaks in the original reduction has a more pronounced effect on reduced area in the reduced data as compared to the newer reduction. This supports the assertion that the shapes returned by the new LoG algorithm are more matched with the shape of the actual spots and less dependent on reduction parameters. Shapes are defined by noticeable changes in scattered intensity rather than arbitrary parameters thereby making the results less depended on how the image was processed. In this way, stability of input to the FMM should result in less variability in the reconstructed microstructure.

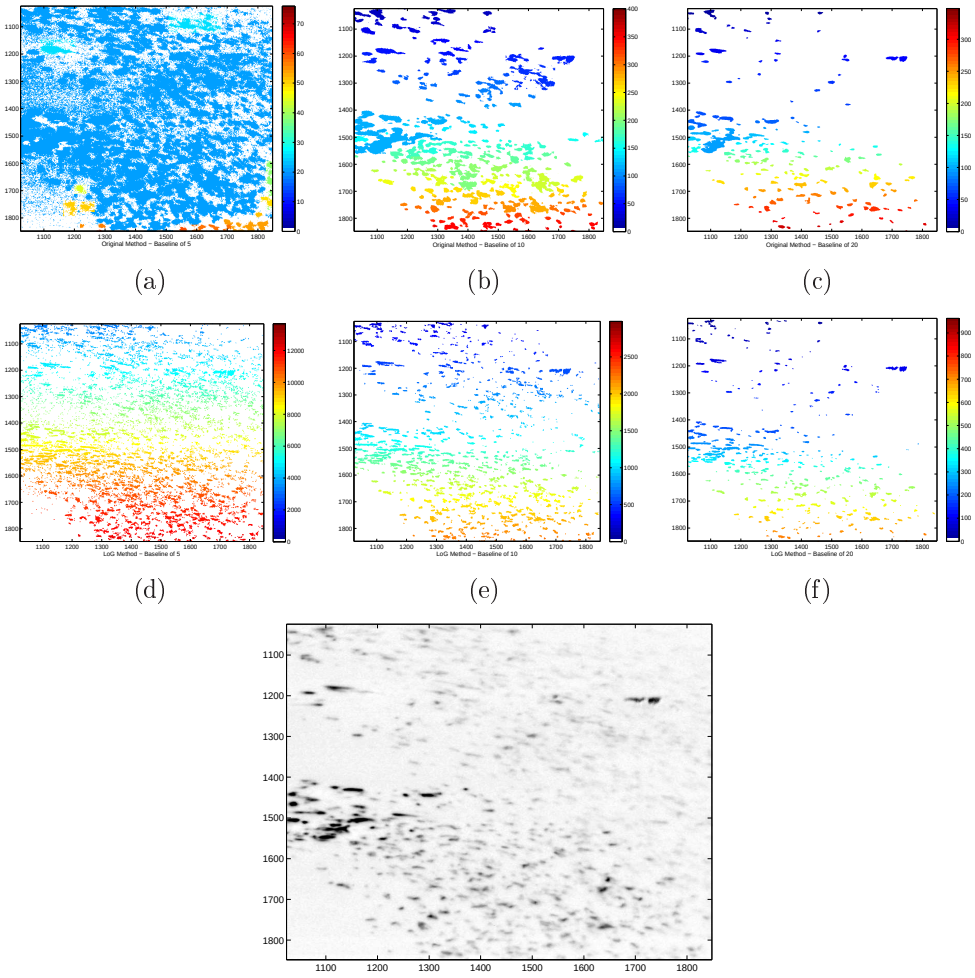

Figure 2.10: (a) - (c) show the segmentation of (g) using the original thresholding method at baseline levels of 5, 10, and 20, respectively. Each unique color represents a single segmented peak. Note that for (d) the baseline of 5 is insufficient to prevent many peaks from being merged into a single peak. (d) - (f) show the segmentation of (g) using the LoG method at baseline levels of 5, 10, and 20, respectively. Note the difference in color scales due to the dramatic variation in the number of distinguishable peaks.

### 2.4.2 Laplacian of Gaussian Operator in 1D

To appreciate how an input image responds to the Laplacian of Gaussian operator, one demonstrative example would be to see its response in 1D. Extending that to 2D (or 3D) is straight-forward. See figure 2.11 for extension from a simple 1D example to algorithm application on image shown previously in figure 2.10(g).

For figure 2.11 notice how edges, defined by where the laplacian crosses zero,

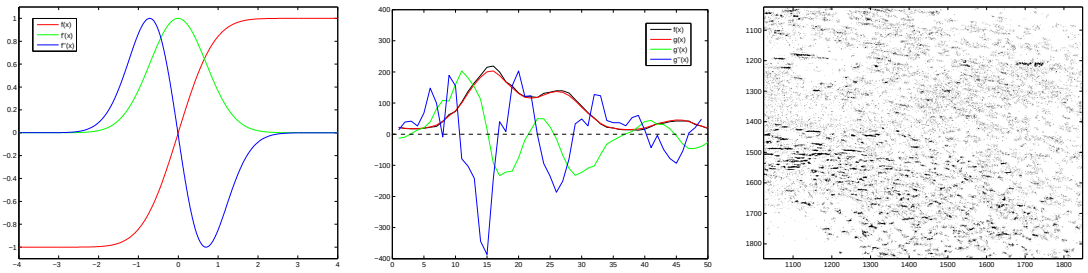

(a) (b) (c)

Figure 2.11: Demonstration of a 1D LoG to and its application to a linear segment on an image. (a) shows the response of the first and second derivatives on an idealized edge as represented by an error function. (b) shows (in black) a 1D raw intensity profile from figure 2.10(g). The red profile represents the profile after gaussian smoothing with $\sigma = 0.75$; the green profile is the first derivative of the red function (scaled for presentation here) the blue profile is the second derivative of the red function (also scaled). The black dashed line at zero is presented to show where zero-cross will define peak edges. (c) represents the binary form of the image in figure 2.10(g) after zero-cross has been performed.

generate an envelope around a peak in 1D, and in 2D they generate closed contours around peaks (or blobs). The three peaks clearly identified in figure 2.11(b) would not have been segmented properly via the simple thresholding method. Test cases such as this LSHR dataset show the failings of the original segmentation method. At this point, the newer method has been described, an illustration of its response on images demonstrated, and a comparison with the original method has been performed. In the next section, results from FMM reconstructions using each segmentation method will be compared with emphasis on different microstructural sensitivities and conclusions drawn on the effectiveness and robustness of LoG segmentation routines.

It must be emphasized that the requirement is to detect intensity *variations* rather than the previously used threshold on intensity *values*. Any special kind of boundary or edge in a microstructure (grain boundary, twin boundary, dislocation wall, phase transition, etc) should be accompanied by a drop in scattered intensity at the edges of associated diffraction spots. In cases of boundaries, this intensity transition should be abrupt. For other cases such as small twin boundaries, a small drop in intensity within a parent peak will correspond to this feature. Sub-grain formation associated with domains within a grain showing small lattice rotation will show small intensity drops at these sub-grain boundaries. Figure 2.11(b) showing the segmentation of two peaks with similar maximum intensities makes it clear that subtle features in the scattering can be detected at the image reduction stage. Seeing this segmentation gives reassurance to any user of nf-HEDM that sensitivity to microstructure features below the grain scale are possible and believable.

While derivate-based edge detection is not a new concept, its implementation for

processing nf-HEDM images has been shown to better segment diffraction peaks and be less sensitive to reduction parameters as compared to previous methods. The use of inflection points rather than user-defined flood levels to define shape edges seems to be a more natural way to represent the peak shape. The speedups and improvements have allowed for more diverse microstructure investigations using nf-HEDM with more sophisticated methods while reducing the amount of user effort needed to process data at the raw image stage.

## 2.5 Microstructure feature sensitivity

The original motivation for replacing the simple thresholding image segmentation algorithms with a more sophisticated algorithm came from the need to study deformation in hcp zirconium. However, improvement from the new segmentation in FMM results is not restricted to that study. The application of the new segmentation method has, in general, shown improvement in many different type of materials studied. The following subsections will show diverse microstructures studied with nf-HEDM as reconstructed with the FMM. The results will be linked to expected physically observed phenomena as a way of comparing results using the two segmentation methods.

### 2.5.1 Boundary position definition

Even in a fully-recrystallized state, the zirconium sample initially (pre-deformation) suffered from accidental overlap of diffraction peaks which is more common in lower symmetry materials than in cubics. Further nf-HEDM allows for reflections of high order scattering to intersect with those low which corresponds to mismatch in intensities. This leads to completely missed peaks in the reduced data due to issues described earlier. Given that in the initially undeformed state individual grains showed no orientation variation, this would lead to diffraction peaks with uniform intensity distributions (flat-top peaks). If two of these uniform intensity peaks were to intersect, the peaks with the lower intensity would either be completely found by the condition $P2_{max} > fThreshPercent \times P1_{max}$ or completely missed. Due to little intensity variation in the $P2$, it can be seen that any pixel in $P2$ will be close in value to $P2_{max}$. Rather than having a gradual failure of the peak shape, the acceptance of weaker overlapping peaks was more of a binary nature.

This has the effect of lowering the total amount of overlap possible between the FMM simulation and what has been accepted into reduced data set. Overall this did not appear to affect the microstructure result, either boundary positions or orientation. This case could be classified as a simple reconstruction where no orientation variation is present and large convex grains were being mapped. The only noticeable difference between the two is the absolute confidence parameter, $\mathcal{C}$.

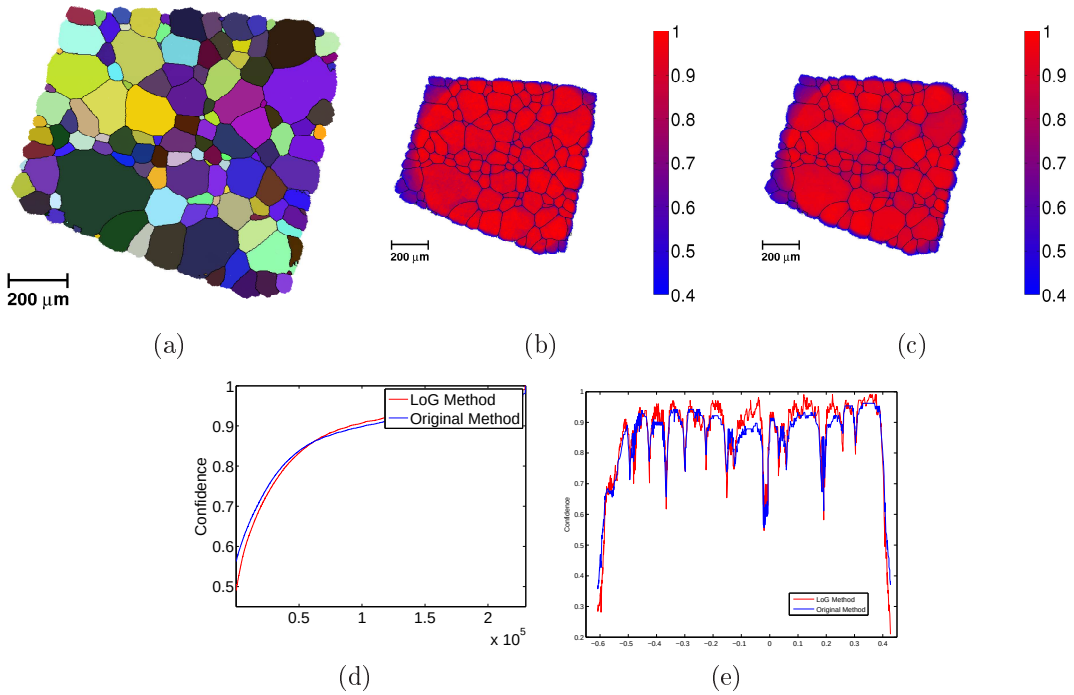


Figure 2.12: (a) shows the FMM reconstruction of a single layer of zirconium before deformation. (b) & (c) represent the confidence parameter for the orientation of each individual voxel fit using the LoG method and original method of image segmentation, respectively. (d) shows the sorted confidence of voxels above a threshold between the two methods. Note that there is very little difference in performance. (e) represents the confidence profile through a single line through the sample for each of the two methods showing drops in $\mathcal{C}$ at grain boundaries, as is expected.

Looking closely at figure 2.12(d), we see that the LoG method has slightly higher confidences than the original method (especially in higher confidence regions). For the given plot, the average confidence of voxels with the new method is 87.11% compared to 85.90% for the original method. Of the orientations reconstructed in this slice with the FMM, there are between 90 and 110 peaks simulated per orientation. An average confidence difference of $\sim 1\%$ then corresponds to about one missing peak per orientation resolved. A minimum error rate for the original method can then also be estimated by, $E = \frac{87.11-85.90}{87.11} = 1.39\%$. This is acceptable, however this estimate is expected to go up in cases of scattering that is less trivial than this. This test serves as a baseline for differences between the two methods.

Notice that figure 2.12(e) demonstrates two features motivated in section 2.3 and might explain the transition in confidences in figure 2.12(d). At the edges of the

sample where there is no competition between two grains to define a boundary, grains might extend outward unchecked. one can note that the the confidence drop-off of the blue curve is somewhat more gradual than the red curve. This corresponds to the study of a single grain undergoing peak dilation. The other feature from this plot is that dips in the confidence profile generally correspond to grain boundaries. It can be noted that confidences in the grain interior tend to be higher for the LoG method consistent with observations made in the previous paragraph. Conversely, confidence at the grain boundaries for the LoG method are lower, perhaps explaining the cross-over that appears in figure 2.12(d). From the bicrystal study, it was shown that better defined peaks lead to sharper transition from high confidence to low confidence at interfaces (smaller FWHM). Note that any FMM reconstruction where the confidence does not dip at boundaries is bad sign even if those confidences are both close to 100% on both sides. Diffraction spot edges are inherently nosiy due to discretization (finite pixel size) and counting statistics. Ideal thresholding should reflect that noise. The fact that confidences drop more precipitously at grain boundaries in the LoG method compared to the original method is then a good indicator of the quality of the reduction method.

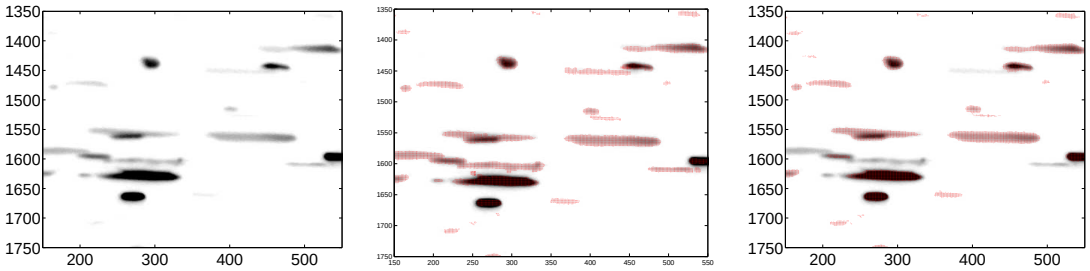


(a) (b) (c)

Figure 2.13: A region of a single scattering image collected from the datset shown in 2.12. (a) represents the image after background subtraction. (b) & (c) show only the pixels selected out by LoG and original methods of reduction, respectively.

Reduced data for the FMM reconstructions shown in figure 2.12 can be seen in figure 2.13. The region shown here illustrates missed peaks in the original reduction which can lead to overall lower confidences. The number of missing peaks in this region is much higher than the quoted $E = 1.39\%$ because this is, this is a region where lower-$|\vec{Q}|$ peaks are more likely to intersect. This implies that the error rate for missing peaks falls off as $|\vec{Q}|$ is increased. Clearly the quoted $E = 1.39\%$ is then the averaged error rate which is more heavily weighted at low-$|\vec{Q}|$. The thinner reduced peaks from the LoG reduction demonstrates the shape definition imposed by by the LoG filter. While the LoG method appears to identify and retain many more peaks than the original method, the size of reduced files are roughly 10% smaller than the original method returns.

Even in this simple case where peak overlap is not severe, a pronounced difference between segmentation methods is found in sensitivity to grain edges. While the positions of grains boundaries remain the same in this comparison case, the new method of image reduction appears to assist the FMM by providing more constrained peak shapes as its input. This should and appears to result in better defined confidence drops at grain interfaces.

### 2.5.2 Ability to reconstruct deformed materials

Since tracking of the same physical volume of microstructure was desired in the zirconium deformation experiment, another important motivation in replacing the original image segmentation method with the new one was the ability to continue to reconstruct as the sample was subject to large plastic deformation. As plastic deformation proceeds, dislocations move and pile-up in grains resulting in orientation gradients. This results in broadening of peaks in both $\eta$ and $\omega$ and loss of peaks entirely at high-$|\vec{Q}|$. Further, residual elastic strains can produce broadening in $2\theta$. Those peaks not lost due to dramatic intensity decreases are then more likely to overlap other peaks. This is a case where advanced peak segmentation is crucial as type-II errors are increasing likely.

Figure 2.14, shows the zirconium sample reconstruction at an engineering strain of 13% for LoG and original image segmentation. Images are segmented using the same reduction parameters ($nBaseLine$, $fPercentThresh$) for consistency of comparison. On first glance, the overall confidences in the LoG-segmented reconstruction are higher than those of the original method. The scales are also different; no voxels are returned in the FMM reconstruction using the original segmentation method with 100% confidence. While it was shown earlier that overly extending peaks can lead to artificially high confidences, this should not be the case for figure 2.14(b) as the pixels returned from LoG segmentation are selected from a subset of those initially available to the original segmentation method and defined by the same shape parameter. The discrepancy in confidence must come from the further peak segmentation occurring after LoG filter is applied. Not only are these newly segmented peaks found but are crystallographically consistent with other identified scattering from grains. This suggests that fewer type-I errors occur for the new method over the previous, as expected. Comparing to the measurement of this volume before the onset of deformation, there is agreement in shape, extent, and orientation of grains between pre- and during-deformation levels (to be discussed further in chapter 3). The comparison of results suggests that extreme overlapping is artificially eroding peaks in the deformed structure and this is causing grains to be lost or eroded in the FMM reconstruction, and this effect is strong for the original method than the LoG method.

Figure 2.15 gives an example of the contrast between reduced data sets. The region shown in figure 2.15 illustrates missed peaks in the original reduction which leads to overall lower confidences. From figure 2.14(d), the average confidence of voxels with

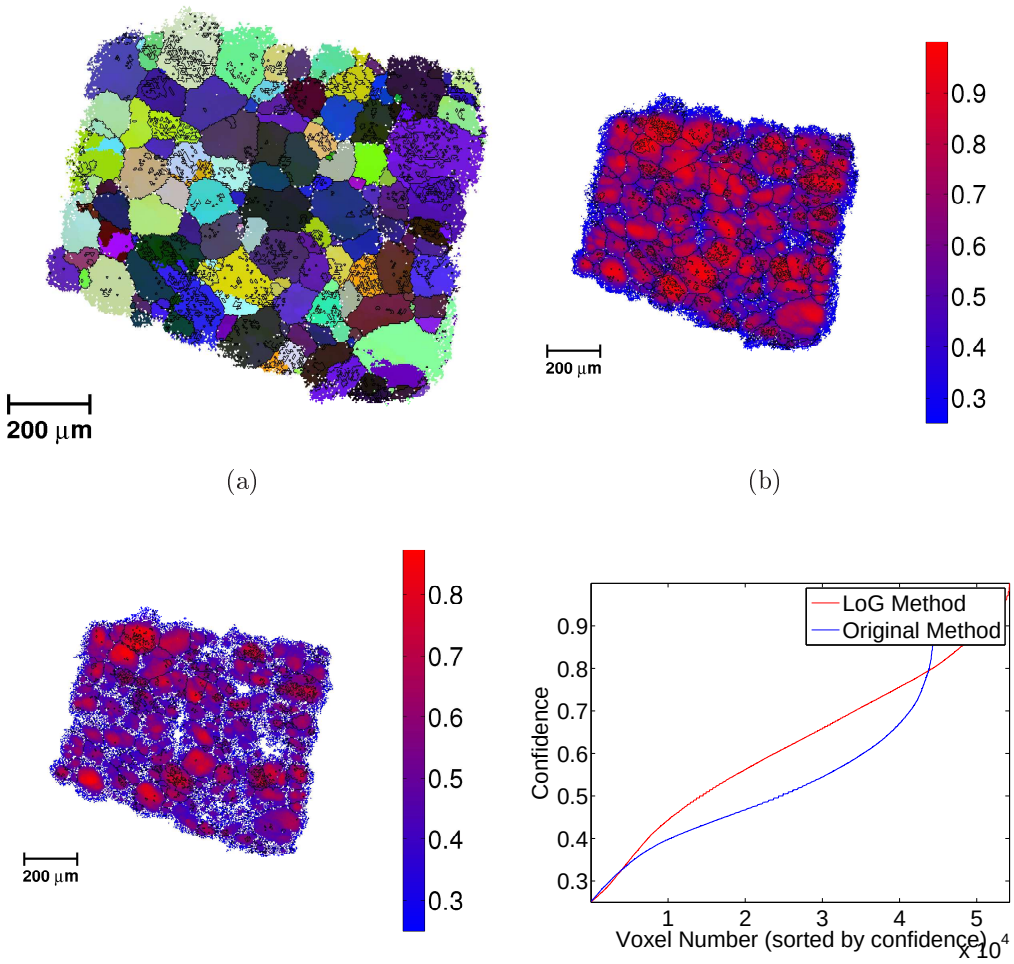


Figure 2.14: (a) show the FMM reconstruction of a single layer of zirconium at 13% engineering strain reconstructed using LoG segmented images. (b) & (c) represent the confidence parameter for the orientation of each individual voxel fit using the LoG method and original method of image segmentation, respectively. (d) shows the sorted confidence of voxels above a 25% threshold between the two methods. The black lines are drawn between voxel that have $\geq 5^\circ$ misorientations. Note that there is a very large difference in performance.

the new method is 63.1% and original method is 48.2%, and the new method finds 22.3% more voxels above the $\mathcal{C} \geq 25\%$. As quoted before, a minimum error rate can be calculated for the original method of $E = \frac{63.1-48.2}{63.1} = 23.6\%$. Each orientation resolved is being done so with an additional 15 peaks in the LoG reduced experimental

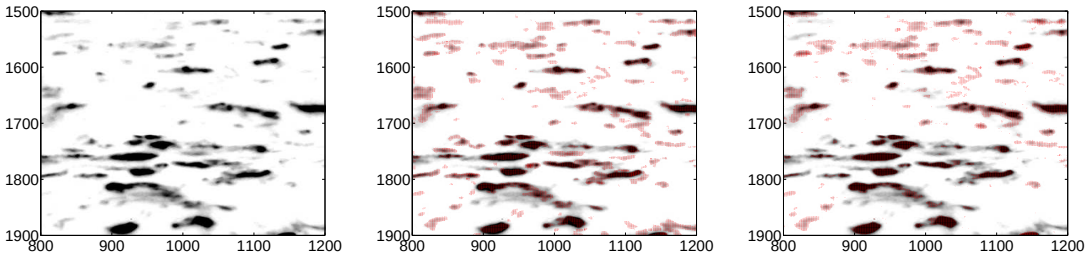


(a) (b) (c)

Figure 2.15: A region of a single scattering image collected from the datset shown in figure 2.14. (a) represents the image after background subtraction. (b) & (c) show, in red, the pixels selected by LoG and original methods of reduction, respectively.

data. This represents a significant difference between the two segmentation methods. The LoG method definitely identifies and retains many more peaks than the original method, and its number of experimental pixels returned in this case is comparable to the original method ($\pm 2.5\%$).

One last striking demonstration of the inability for FMM to reconstruct a highly-deformed material given poor reduced input would be the example of a piece of copper which has been ballistically-shocked. This copper sample was mapped in its undeformed state using nf-HEDM, then it was subjected to a high strain-rate deformation at Los Alamos National Laboratory. The same volume of the sample was then re-measured. Figure 2.16 shows the reconstructed microstructure for a layer of material in the deformed region (which contain voids) compared side-by-side where the only difference between how the two were processed was at the image processing stage. Initially this dataset was abandoned in the belief that microstructure data could not be reconstructed in the deformed region, which is the region of most interest. When the LoG method of reduction was applied, this dataset could be salvaged and new science investigated. Current work is being done to register pre- and post-deformation microstructures to pin-point where void formation occurs. This registration, at the preliminary stage, appears to match quite well.

In cases where considerable deformation is present, and hence peak overlap is present, a pronounced difference between segmentation methods is found in the overall ability to reconstruct using the FMM. Size and shape correspondence to measured undeformed states serves to justify that the larger extent of grains obtained from the newer method are physical. The performance of the new method of segmentation in cases of deformed microstructures shows an ability to segment many more physically and crystallographically consistent peaks. This leads to an overall better ability to reconstruct with FMM. Deformed microstructure reconstruction should not be attempted without advanced image processing to ensure high-fidelity FMM input. The original method should be abandoned even if reconstruction is possible.

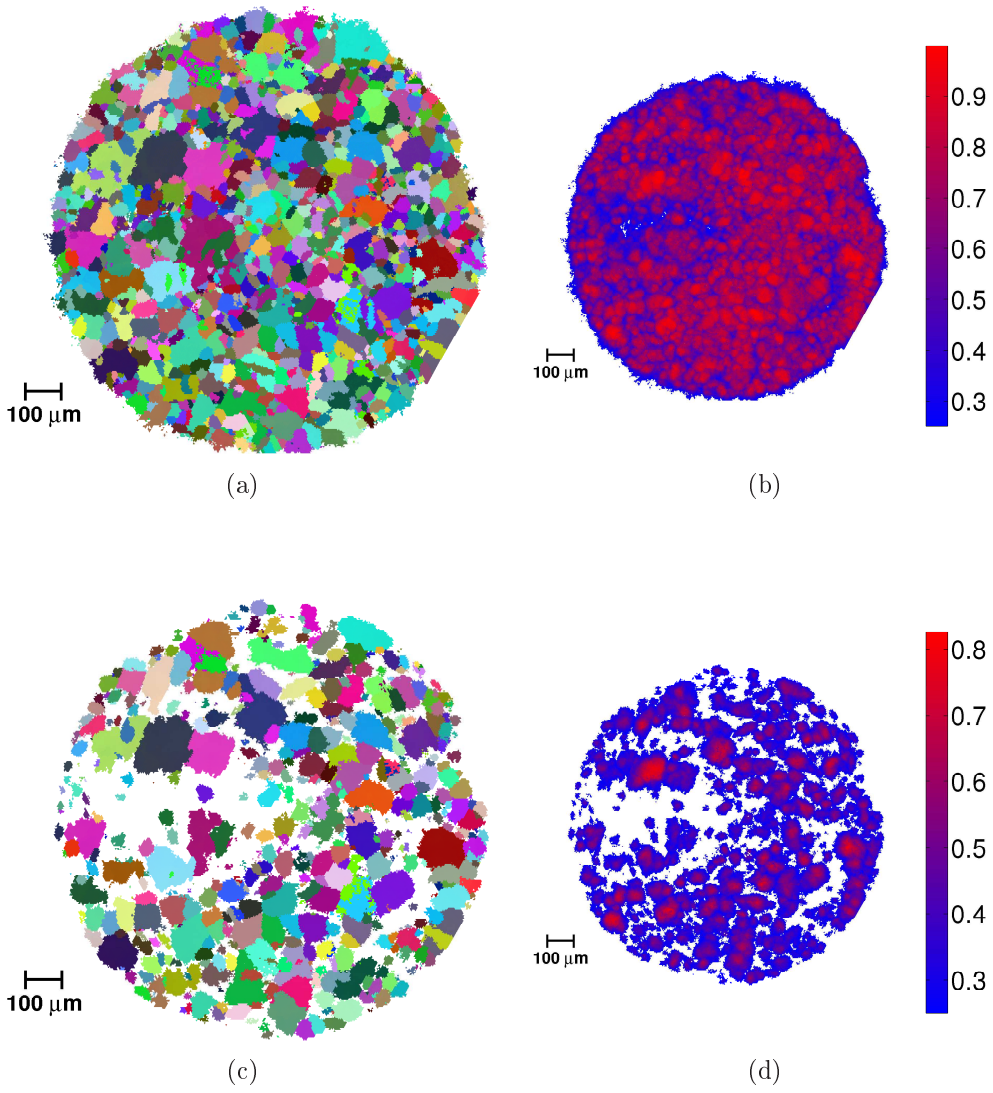


Figure 2.16: Above are the Rodrigues-colored orientation map and confidence maps for the post-shock copper processed with the LoG method ((a) & (b)) and the original method ((c) & (d)). As in 2.14, again upper end of confidence scales do not match.

### 2.5.3 Shape representation

While the subject of the stability of boundary position was discussed in section 2.5.1 and with relatively little scattering complexity, some discussion should be made about what to believe when the boundary shapes diverge depending on image processing. An initial inclination would be that the boundary shapes reconstructed by the LoG method are closer to that of the true microstructure because the variability of its

reduced data results are much less dependent on reduction parameters. Given that the microstructure returned by the FMM is mostly independent of reduction parameter in the LoG method but not in the original method, its returned microstructure is much more stable but not necessarily the true microstructure. In this section, linking of expected microstructure grain boundary shapes will be used to confirm this initial expectation.

One important geometrical feature in face-centered cubic (FCC) metals is the appearance of coherent annealing twins which are energetically-favorable [15]. These occur when low stacking fault energies are associated with certain crystal planes; for FCC the lowest stacking fault energy plane is the {111} which commonly gives rise to coherent $\Sigma 3$ twins. They are generally understood as "growth accidents on {111} planes propagating" during grain growth [16]. Coherent twin boundaries are identified in orientation imaging microscopy (OIM) by their misorientation (60° about <111>) and by their common flat {111} boundary. The coherent twins are seen as distinct lamella shaped features spanning parent (host) grains. The expectation of a large population of annealing twins in FCC metal is inversely related to the energy of the boundary [17].

The nf-HEDM group has studied annealing twins for several years at this point since annealing twins have a specific orientation relation and morphology that are based in physical reality. They have linked the twin misorientations found in reconstructed microstructures against the expected misorientation as one way of defining the orientation resolution of the nf-HEDM as it depends on other things like $\delta\omega$ [18]. The concept of the 5 parameter grain boundary character distribution (GBCD) has been shown to be an important metric for characterizing microstructures [17, 19]. Briefly the GBCD consists of specifying and binning all boundary patches in a microstructure by their local misorientation relation (3-parameters) and the local boundary normal (2-parameters). Since complete microstructure characterization is the goal of nf-HEDM and $\frac{3}{5}$ of the GBCD concept (local misorientation) have been used to justify the techniques orientation relation, the other $\frac{2}{5}$ of the GBCD concept (local bounday normal) will be used here to link boundary position and shape with segmentation routine efficacy. To this end, two nf-HEDM slices of a fractured nickel superalloy were collected at the APS in December of 2010 (one at the fracture surface, and one $1mm$ below it). Presence of annealing twins could be noticed even during diffraction data collection by visual inspection of peaks as they were being collected.

Figure 2.17 presents differences between FMM reconstructed maps depending on how images are initially processed. Up to this point, boundary differences shown were deemed either exactly the same or completely different. One difference that should be pointed out is the difference in character of the two confidence maps. The confidence map for the reconstruction with the original method of image segmentation appears to have higher confidence fit voxels compared with return LoG method voxels. However, confidence drops are not pronounced at boundaries for the original method, while

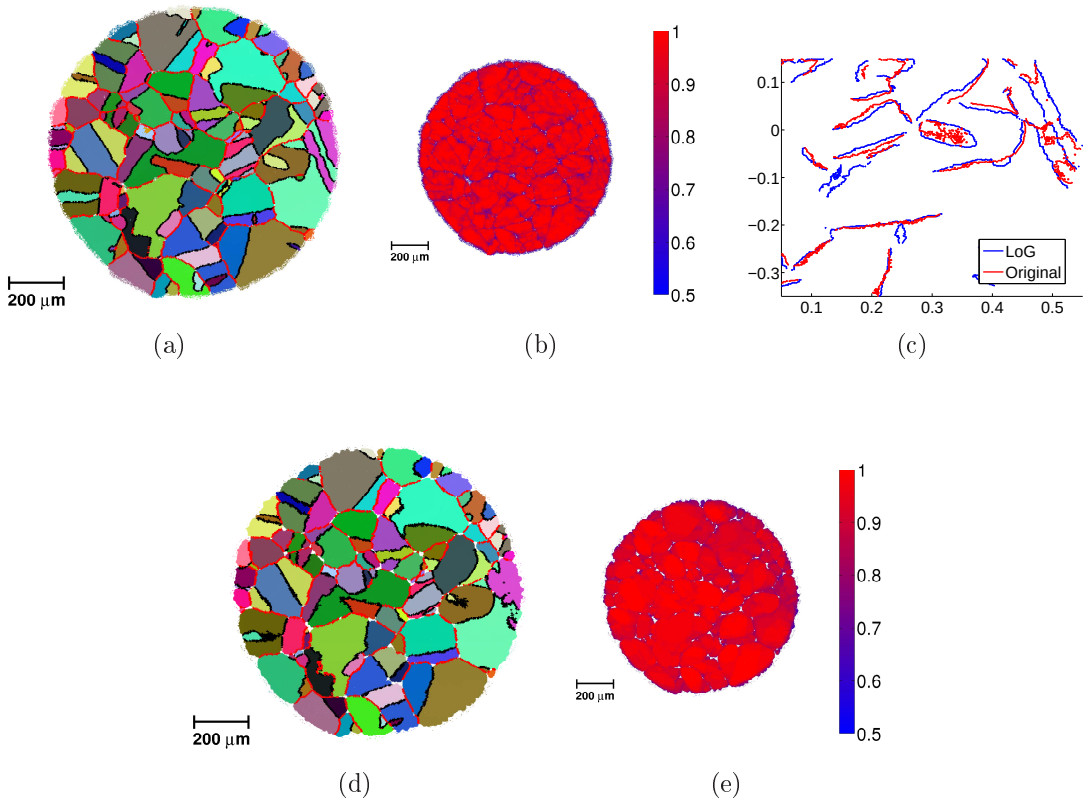


Figure 2.17: Presented here are the FMM reconstructed orientation and confidence maps for a layer of a superalloy sample that was measured $1mm$ below a fatigue fracture surface. (a) & (b) were generated using reduced data from the LoG method and (d) & (e) from the original method with same reduction parameters for comparison. Black lines in (a) & (d) represent boundaries satisfying the $\Sigma 3$ annealing twin misorientation criteria within $0.5°$; red lines represent all other grain boundaries. (c) shows the set of $\Sigma 3$ boundaries for each case of reduction method in a zoomed in $0.5mm \times 0.5mm$ region of the sample.

noticeable drops occur at grain boundaries and twin boundaries. Further, confidences vary within grains for the LoG method whereas they appear to be constant in grains from the original method. This second observation will be addressed a little later.

One can recognize from figure 2.17(c) that more twins are classified in FMM reconstruction using the LoG method over the original method. For a parent grain with a single annealing twin in the center, some diffraction spots will have intensity profiles that are shaped like a camel's back (akin to the black profile in range [5 35] of figure 2.11(b)). The width and depth of the valley depend directly on the twin size. Depending on reduction parameters, this valley in the intensity will still be accepted

as experimental signal in the reduced data if processed via the original method. Retaining these pixels corresponds to keeping pixels which bolster confidences for the parent grain orientation in spatial regions where intensity drops are present. Fitting orientations by way of intensity fitting should help correct for errors like this. While pixels for the twin orientation *should* also be present, any missing twin peaks could lead to choosing the parent orientation over the twin orientation. In this way, twins can be lost due to degraded signal which is input to the FMM. One final observation should be made that since annealing twins are generally smaller than their parent (host) grains, their scattered intensities should be proportional to their cross-sectional area.

Next, focus is drawn on a single annealing twin boundary in this dataset in figure 2.18. As introduced earlier, energetics dictates that coherent $\Sigma 3$ interfaces will have higher populations than incoherent $\Sigma 3$ interfaces. Incoherent $\Sigma 3$ interfaces are when the boundary satisfies the expected misorientation relation, $60^\circ$ about <111>, but fails to occur on a common {111} plane as the interface. The boundary shown in this figure has a misorientation of $59.98^\circ$ about $[-0.5775, 0.5784, 0.5761]$ in axis-angle representation. This misorientation represents a deviation in $0.017^\circ$ in angle and $0.4389^\circ$ in axis from the expected $\Sigma 3$ misorientation. The black boundary trace shows the ideal shape of a coherent interface for the given grain orientation. Performing simple statistics on the histograms shown in figure 2.18, a standard deviation for distances from the true boundary plane is calculated with results $\sigma_{LoG} = 1.50\mu m$ and $\sigma_{Original} = 2.95\mu m$. These reconstructions were performed with voxels of $2.8\mu m$ side-width (sw). If one assumes Gaussian statistics and computes a confidences interval between [-sw sw], 93.9% of boundaries from the LoG method fall in this interval as compared to only 65.8% for the original method. It seems boundary precision for the LoG method is limited by the grid resolution used here whereas it seems the spatial precision of boundary position is limited by the reduction method in the case of the original method. One could perform this test at higher grid resolution where either pixel size or reduction method might define the limiting spatial sensitivity.

Another link needs to be made here to the simulation study at the beginning of this chapter, specifically what was shown in figure 2.6. A parent and its accompanying twin are pulled out of the FMM reconstructed map. The parent and twin orientations are then averaged separately and assigned to a region $30\mu m$ larger than its reconstructed extent. For each point in the sample space, overlap from the given averaged-orientation with experimental reduced data is calculated and presented in figure 2.19. One thing that must be emphasized is that the confidence profiles presented here do not represent the FMM returned confidence profiles which should have confidences $\geq$ to those in the figure. Two main features should be pointed out, the first is again that the boundary returned from the LoG method appears to be straighter with much less ambiguity at the twin boundary than compared to the original method. The other is that the spatial profile of confidence drops off much more gradually for the original method as compared with the LoG method. Strikingly, in

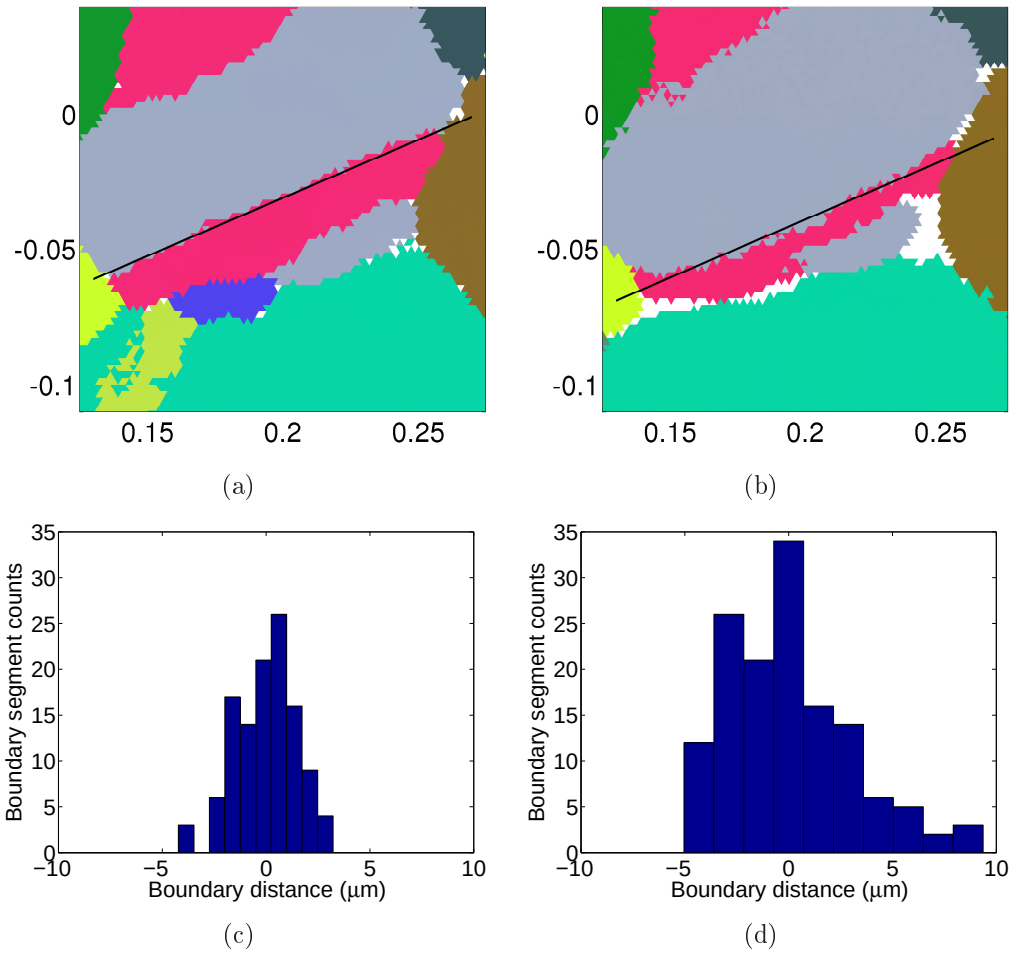


Figure 2.18: (a) & (b) represent the same $150\mu m \times 150\mu m$ region of the reconstructed microstructure as processed by LoG method and original method of image segmentation, respectively. The gray-pink interface represents a boundary satisfying the misorientation criteria of a $\Sigma 3$ within the orientation resolution of the FMM. The black line shows the intersection of the gray grain's $(\bar{1}11)$ plane with the sample plane. (c) & (d) represent the histogrammed distance for each boundary segment from the true coherent twin plane for processing by LoG method and original method of image segmentation, respectively.

the former case, confidences for the parent orientation of greater than 50% extend past the twin boundary into the twin more than $30\mu m$. Notice that the confidence profile drops off much more slowly at twin boundaries for the original method as opposed to non-$\Sigma 3$ boundaries (see regions around red boundary lines in figure 2.19). LoG method appears to distinguish $\Sigma 3$ and non-$\Sigma 3$ boundaries with similar sensitivity.

Appealing to the physical geometry of the coherent $\Sigma 3$ boundaries present in

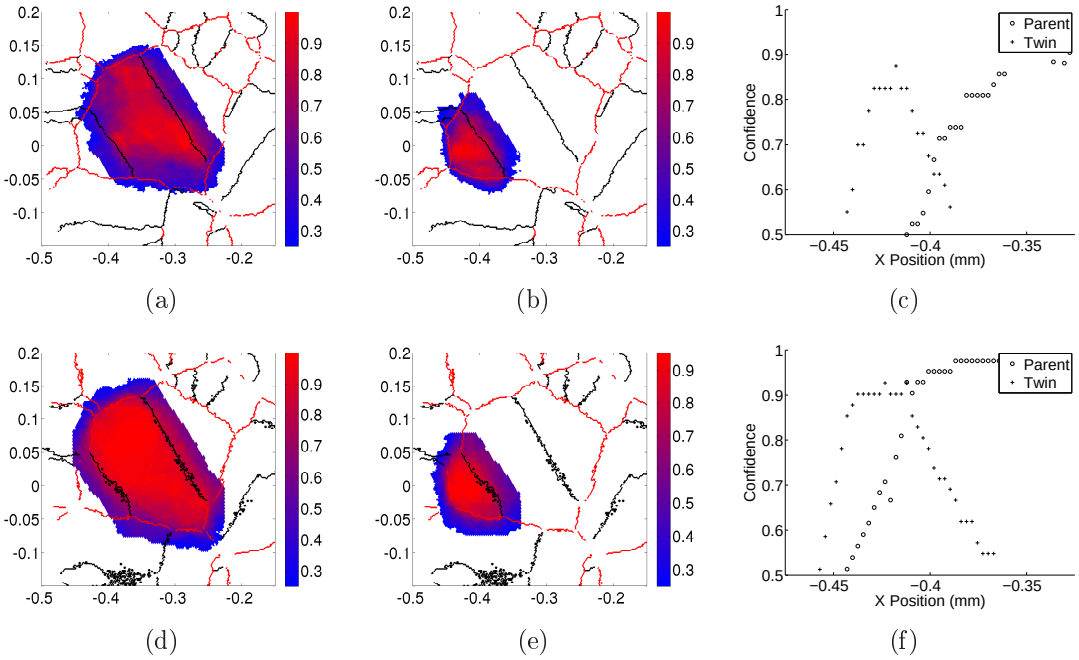


Figure 2.19: (a) & (d) show the spatial confidence extent of the average orientation using the parent grain for LoG method and original method of image segmentation, respectively. (b) & (e) show the spatial confidence extent of the average orientation for the twin grain using the LoG method and original method of image segmentation, respectively. Black lines in (a) & (d) represent boundaries satisfying the $\Sigma 3$ annealing twin misorientation criteria within 0.5°; red lines represent all other grain boundaries. (c) & (f) show the line-out confidence profiles for both parent and twin grain along the x-direction. These plots are analogous to what is shown in figures 2.6, 2.7, & 2.8.

FCC materials, the resulting spatial resolution from each type of image segmentation routines was estimated by this. The original method appears to be the limiting factor for spatial resolution of the FMM, while grid size is limiting spatial resolution for the LoG method. Further, it was shown that $\Sigma 3$ boundary sensitivity was greater in the LoG method due to the precipitous drop off in confidence for a grain's orientation beyond the boundary point.

### 2.5.4 Small features

After showing that the inherent spatial resolutions of the two image segmentation methods are different, the next logical steps would be to compare FMM ability to resolve small features (small grains). One way of studying this is to take advantage of the fact that grains have 3D shapes, but nf-HEDM only produces 2D cross-sectional orientation maps. For this demonstration, a fine-grained ($\sim 50 \mu m$ diameter grains) grain-boundary engineered (GBE)[20] copper sample is used. GBE samples

are thermo-mechanically processed to produce higher boundary fraction of CSL $\Sigma$ boundaries. The specifics of grain-boundary engineering is not relevant here, but rather the point that a microstructure with small grains that has large amounts of annealing twins is investigated with nf-HEDM.

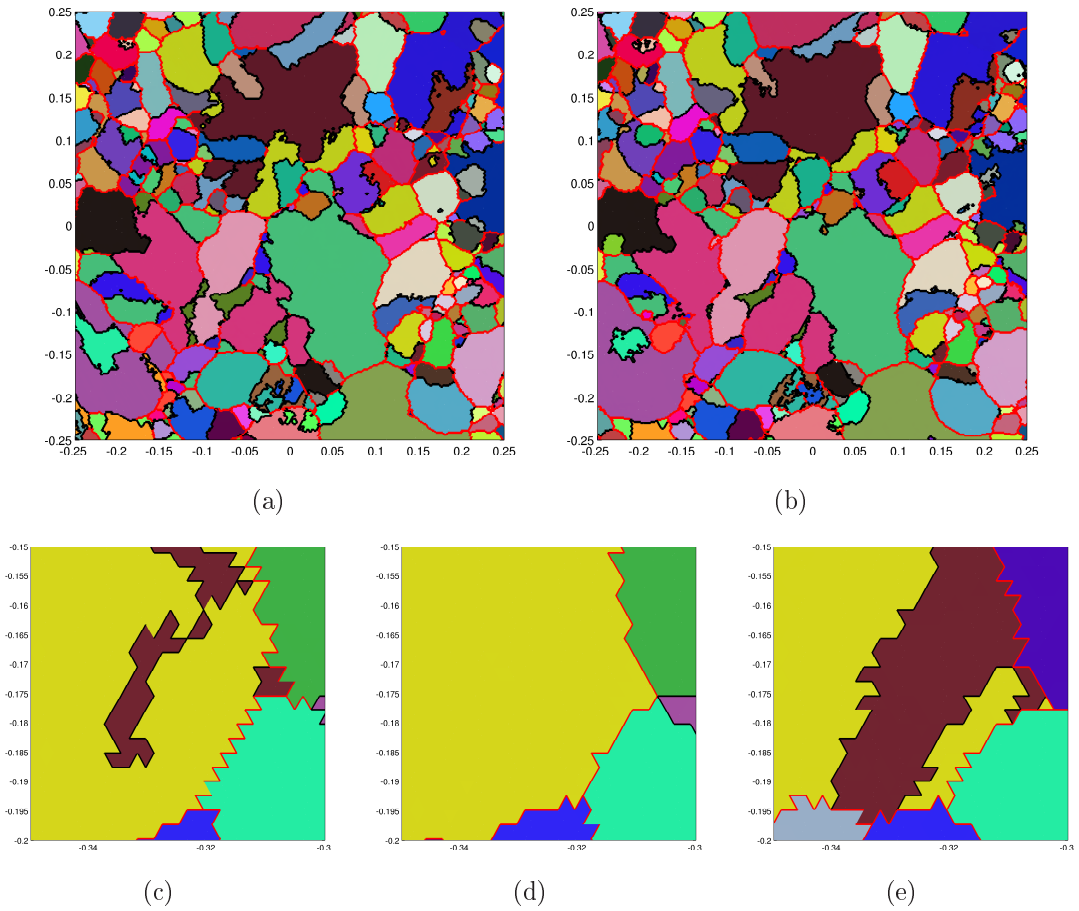

Figure 2.20: (a) & (b) represent the same $500\mu m \times 500\mu m$ region of the reconstructed GBE copper microstructure as processed by LoG method and original method of image segmentation, respectively. (c) & (d) shows a $50\mu m \times 50\mu m$ smaller region of interest, processed by LoG and original methods, respectively. Figure 2.20(e) shows the same $50\mu m \times 50\mu m$ smaller region of interest for the next successive slice of microstructure reconstructed using the original method. This represents a region $4\mu m$ vertically below the previous slice. Black lines represent boundaries satisfying the $\Sigma 3$ annealing twin misorientation criteria within 0.5°; red lines represent all other grain boundaries.

Determining by inspection whether small features returned from FMM are real or artifacts can be difficult. Figure 2.20 shows the complicated twinned GBE copper microstructure as image segmentation routine is varied. On first observation, there

are slight differences between the two zoomed-out regions and which one represents the actual sample measured is not clear. One will notice shapes and locations of boundaries are not the same between the two, and in either case, each shows some new small features where the other does not. If one compares the two visually, the LoG method map seems to have many more unique small features compared with the original method. Since we expect many annealing twins, specifically looking for $\Sigma 3$, embedded in parent grains, the twins should represent, on average, a smaller spatial features. Calculating the length-fraction of $\Sigma 3$ boundaries is done simply by $\frac{\text{Length of all } \Sigma 3 \text{ boundaries in slice}}{\text{Length of all grain boundaries in slice}}$ yields 49.7% for the LoG method and 47% for the original method. A slightly larger (0.5%) overall boundary length is returned from the LoG method compared to the original. Given that the size distribution of twins should be smaller than non-twin grains, the increase in twin boundary length for LoG method points at its ability to better resolve smaller features. A larger fraction of the twin size distribution resides at the $\sim 2\mu m$ scale compared to the general size distribution, meaning that accessing smaller features should disproportionately bolster the number of twins, and consequently number of twin boundary lengths.

Finally figures 2.20 (c) - (e) present anecdotal evidence that the LoG method is indeed finding small features, $\mathcal{O}(sw = 2.81\mu m)$, that are missed by the original method. The brown twin within the yellow parent in this figure is found in the layer where LoG method segmentation was used as input to the FMM. This twin was absent when processed with the original method. The twin appears to be 1-2 voxels wide which would be within the spatial resolution of the LoG method but closer to or below the resolution for the original method. However, $4\mu m$ vertically below this slice, the original method detected this twin when it is then 5-6 voxels wide. This is perhaps a situation where the tip of the twin was being measured. This example, along with prior evidence for spatial resolution depending on segmentation, demonstrates the fact that the LoG method produces input data for the FMM that results in better spatial resolution.

### 2.5.5 Orientation variation

At this point is has been shown that improved image processing in the pre-FMM results in a more accurate representation of the grain boundary shape with finer resolution. Concern has focused on boundaries between grains with completely distinct sets of diffraction spots, or $\Sigma 3$ boundaries where there is some amount of overlap. This is to say that for $\text{grain}_\text{A}$ and $\text{grain}_\text{B}$ which share a boundary, since they represent different direct lattices, their Bragg peaks will in all likelihood be independent of each other on the detector plane. Phrased in another way, nf-HEDM collects projections of the direct lattice in reciprocal space. Their reciprocal lattices will inhabit their own region of reciprocal space with little overlap. When perturbation of the real space lattice changes rapidly in sample space (grain boundaries, twin boundaries, phase difference), FMM is sensitive to the abrupt changes in reciprocal space.

The FMM has already been shown to be sensitive to intra-granular orientation variations especially in heavily deformed materials [3, 21, 22]. Given that the real space and reciprocal space measurement of grains are done simultaneously in nf-HEDM, a consequence of the increase in spatial resolution due to constrained peak shapes might equally signal an increase in orientation resolution. Constraint of peak shape also removes instrumental broadening in reciprocal space which leads to uncertainty in orientation measurement. Signs of improved orientation resolution in deformed materials will be discussed below in the context of a physically observed phenomena in materials science using the electron back-scatter diffraction technique (EBSD). On this basis intragranular misorientation is expected to depend on image processing, and so a null-hypothesis is presented that intragranular features produced through FMM do not depend on image processing.

The case of nf-HEDM orientation resolution has been studied in the trivial case of no deformation by way of *intergranular* misorientation. It would benefit future deformation studies to understand how much image processing can improve the ability to resolve small lattice rotations within grains (*intragranular*). Numerous studies using EBSD have attempted to quantify the geometrically-necessary dislocation (GND) or stored energy content of individual grains via orientation gradients observations [23, 24, 25]. During deformation, researchers have observed subdivision of grains by fragmentation during deformation ascribed to the necessity of mechanical compatibility in tests. Quantification of orientation gradients has been performed in various ways to obtain damage metrics [26, 27]. Some basic tools for interpreting local and long-range lattice distortions include the kernel-average misorientation (KAM) and intra-granular misorientation (IGM). KAM at any given point is defined as the average misorientation with every element in the local kernel (typically $1^{\text{st}}$ or $2^{\text{st}}$ nearest neighbors) including only those elements below some threshold misorientation (typically $\theta_c \leq 5^\circ$) to ignore elements in neighboring grains. IGM at any given point is defined as the misorientation of that element with its associated grain's average orientation. IGM requires every element in an orientation map to be assigned a grain ID.

Within grains, fragmentation subdivides the grain into subgrains with small misorientations between them. With different orientations, the subgrains deform differently from each other showing small continuous lattice rotations induced due to slip. This has a result of having large ($\mathcal{O}(0.5 - 1.0^\circ)$) KAM values at the boundaries of subgrains and a discontinuous jump in orientation. Within subgrains, KAM values are lower than at subgrain boundary, but across their interior there is a gradual orientation change. These qualitative features of deformation will be studied in the previously shown nickel-superalloy introduced in section 2.5.3. This particular sample is used for this purpose owing to expected low plastic strain content since it was a fatigue sample studied away from the crack region.

Qualitatively looking at the gray-scale KAM and IGM plots in figure 2.21, subgrain boundaries are easily seen in the top KAM figure (2.21(a)) while the bottom KAM

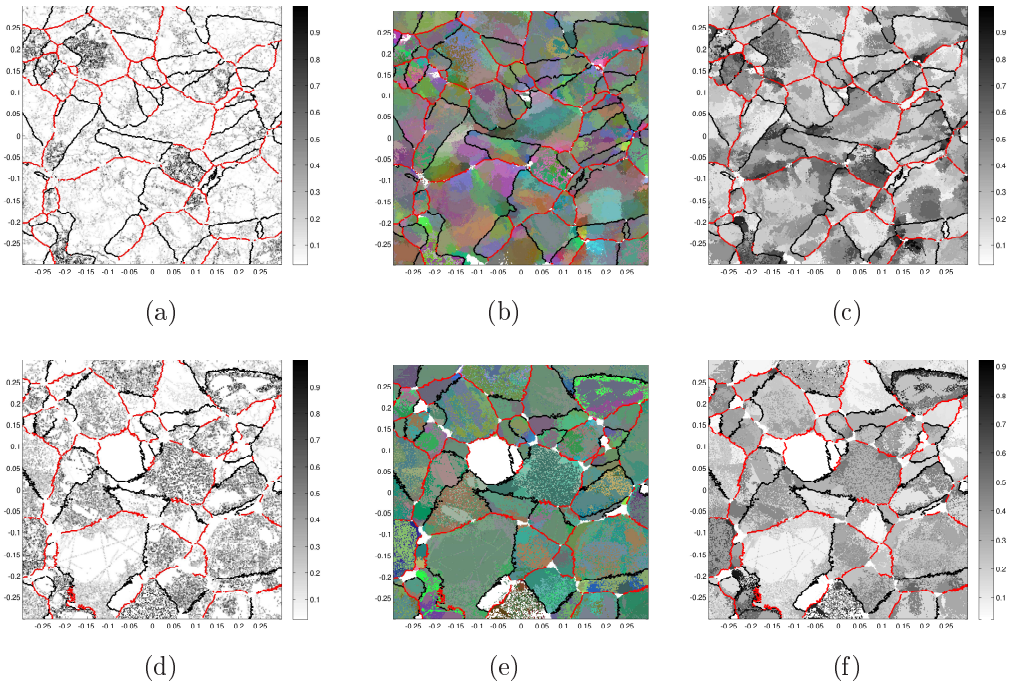

Figure 2.21: A $600\mu m \times 600\mu m$ area of a fatigued nickel superalloy analyzed with KAM and IGM. (a) & (d) shows the KAM for the orientation maps shown in fig. 2.17(a) & 2.17(d), respectively. (c) & (f) shows the IGM as a scalar value in the same order as the previous pair of figures. 2.21(b) & 2.21(e) shows the IGM as colored by Rodrigues vector in the same order. All figures are plotted on scale of $0 - 1°$. Boundary line plotting is consistent with previous figures and shown to indicate where grain boundaries exist.

figure (2.21(d)) appears to be somewhat random. One expects and notices that high-KAM values in the top figure correspond to walls around similar gray-scale level in the IGM figure (2.21(c)). Within subgrains there appears to be gradual changes in gray-scale level. Subgrains are not so easily defined in the bottom figure (2.21(f)).

Returning to figure 2.19, it is evident that the gradual drop-off of cost before boundaries in the case of the LoG method is due to deviation of the local orientation from the grain average. Since this test was performed assuming a single grain orientation, the small differences in cost within the grain can be ascribed to local orientation variations. The absence of this in the original method case supports the lowered intragranular orientation resolution.

The center figures visually represent how the lattice is changing orientation within grains. Common colors depict regions (or voxels) with similar rotation axes from their grain average. The gradual change in colors in subgrains represents the continuous lattice rotation one expects to see in deformed materials. The fact that regions bounded by high-KAM values have similar color in figure 2.21(b) but appear less correlated in

figure 2.21(e) suggests that the deformation level of this sample is resolvable with the LoG method but not with the original method.

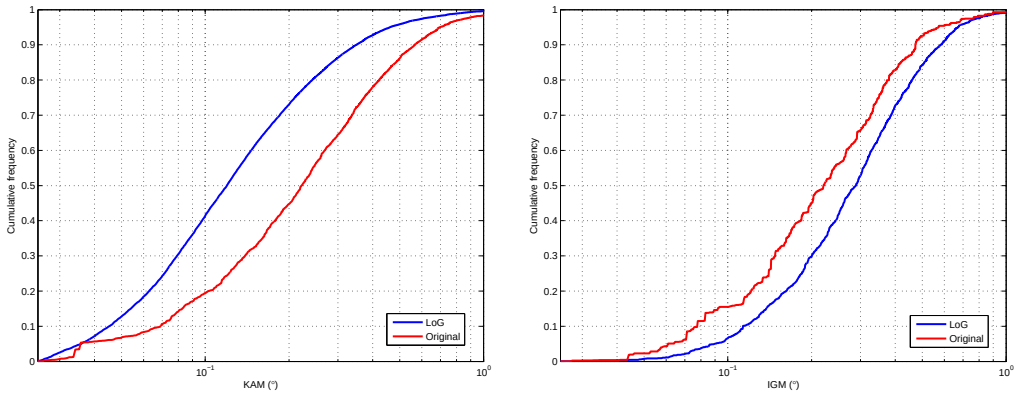


(a) (b)

Figure 2.22: Cumulative distribution for KAM and IGM taken from the data shown in figure 2.21.

Since the only variable changed between the two fits was the image processing method, one can compare the width in KAM distributions to determine an upper-bound on orientation resolution in this deformed case. From figure 2.22 we can find the median ($Q2$) and standard deviations ($\sigma$) of KAM and IGM for the LoG and original methods (see table 2.2).

| | $Q2_{KAM}$ | $\sigma_{KAM}$ | $Q2_{IGM}$ | $\sigma_{IGM}$ |
|---|---|---|---|---|
| LoG | 0.12° | 0.16° | 0.29° | 0.32° |
| Original | 0.22° | 0.24° | 0.22° | 0.19° |

Table 2.2: Median and standard deviation values for measured KAM and IGM.

One would expect given large enough statistics, that the median or mean values of the KAM distributions would match since sampling is being done from the same physical microstructure; however, this is not the case. Noting first that $Q2_{KAM,Original} = Q2_{IGM,Original}$ and more definitively the red (original) KAM and IGM curves are very similar, one expects a large median and broader distribution of IGM values than KAM due to the scales on which these metrics operate. Long-range gradual orientation gradients would manifest themselves by a peaked KAM distribution near the resolution of the orientation measurement, and a peaked IGM distribution near the $\sim 0.25 \times OrientationRange$. Only if the intragranular orientation range is below or at the orientation resolution, will KAM and IGM match. For defining orientation resolution bounds, $Q2_{KAM}$ should be used as opposed to $Q2_{IGM}$ to put an upper-bound on the orientation resolution. For the LoG case given that the IGM and KAM distributions differ, an upper-bound on intragranular orientation resolution can be

defined at $Q2_{IGM,Original} = 0.12°$. This is in good agreement with the previously quoted intergranular misorientation resolution of the FMM, and suggests that internal grain features are equally resolvable as grains themselves. For the original case given than IGM and KAM distributions are similar, an upper-bound on intragranular orientation resolution **cannot** be defined. Since comparisons are being made from the same sample, one concludes that the orientation resolution is dependent on image processing.

While arguments to this point have suggested differences between the two results, a Kolmogorov-Smirnov test (ks-test) [28] is employed here to validate or invalidate the null-hypothesis. A P-value is the result from any statistical test which represents the likelyhood that a test statistic comes from the observed distribution. First a ks-test is performed between KAM distribution results via LoG and original method (figure 2.22(a)); this results in a rejection of the null-hypothesis with P-value = 0. Next a ks-test is performed between IGM distributions between results via LoG and original method (figure 2.22(a)); this also results in a rejection of the null-hypothesis with P-value = 0. With the null-hypothesis rejected, we can claim that intragranular features produced through FMM do depend on image processing, and those produced through the LoG method appear to match what has been physically observed in similarly deformed materials with an independent measurement technique (EBSD).

A measurement of an aluminum sample with similar deformation content to the superalloy sample was performed at three differents states of annealing [19, 29]. This is one of the original in-situ nf-HEDM experiments performed which showed the FMM capability to resolve orientation gradients. It was through much required user-intervention that optimal reduction parameters in the original reduction method were found so as to see orientation gradients of character similar to those shown in figure 2.21. KAM and IGM trends were tracked as recovery and recrystallization took place. As the new method was implemented, further improvement in what could be extracted from this dataset was found. Previously unresolved bulk recrystallization events were found and validated through observations of the scattering signal (see section 2.5.4), and also more physically-representative FMM reconstruction were returned in terms of the qualitative nature discussed earlier. The differences in reconstructed microstructure for the aluminum across image processing was not nearly as stark as the nickel superalloy presented above. The nickel superalloy was not reduction-parameter-optimized in such a detailed manner to the aluminum due to infeasibility of human time required. The nickel superalloy's diffraction images were processed in a generic "rule-of-thumb" way that most other samples have been processed in the past; no user intervention to optimize images, only relying on what has worked previously as a guide.

To summarize, the result of the FMM's sensitivity to intragranualar orientation variation is dependent on how the diffraction images are processed. The LoG method appears to match (qualitatively) more closely to the expected physicality of a deformed microstructure. Since the actual microstructure does not depend on data

processing, one hopes that there is an ability to define a correct result and that the output of the nf-HEDM microscope depends only loosely on the initial image processing details. If the results do depend on the image processing method, as shown in this section, the next natural question would be to quantify by how much they vary with detailed parameter variations. The stability in the reconstructed microstructure as a function of image processing parameters leads to the next section.

### 2.5.6 Sensitivity to reduction parameters

To quantify the effect on the reconstructed microstucture dependence of image processing, a study on a fine-grained, fully-recrystallized nickel superalloy was performed. A $200\mu m \times 200\mu m$ patch of sample space is selected and grided with $1\mu m$ side-width triangles to be reconstructed while varying the segmentation method (LoG, Original), the reduction parameter $nBaseLine$ (2, 5, 10), and the reduction parameter $fThreshPercent$ (0.05, 0.1, 0.25). These values span a normal working range of reduction parameters that have been used to process nf-HEDM images. This represents a study of $\sim 2 \times 3 \times 3 \times 100k$ voxels. For each of the reduction methods, comparisons were made between the varied reduction parameter and the baseline case ($nBaseLine = 2$, $fThreshPercent = 0.05$). Point-by-point misorientation and point-by-point confidences were computed as well as boundary distance moved.

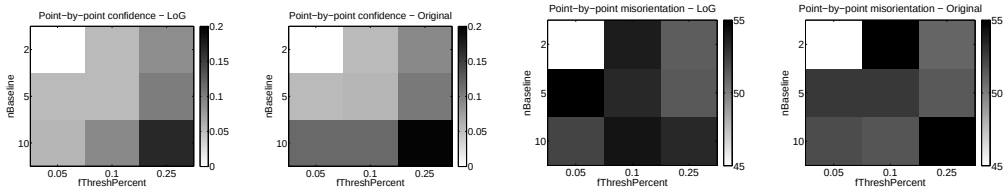


(a) (b) (c) (d)

Figure 2.23: (a) & (b) represent the median confidence difference in the reduction parameter space of varied $nBaseline$ and $fThreshPercent$ for LoG and original methods, respectively. (c) & (d) represents the median misorientation difference in parameter space. Differences were considered against the baseline case where $nBaseLine = 2$, $fThreshPercent = 0.05$ (upper left tiles) which is why they are white (0). In calculating the median confidence difference, values with $\Delta\mathcal{C} \leq 0.5\%$ are ignored. For median misorientation differences, values with $\Delta\theta \leq 1.0^\circ$ are ignored.

While the trends in microstructure difference as reduction parameter is varied is shown in Figure 2.23 using point-by-point confidence difference and misorientation, there is little to no significant difference at this level. The range in confidence differences across the parameter space are only slightly less for the LoG method compared to the original (16.7% vs. 19.4%), but most of this is likely due to the removal of

experimental signal by those reduction parameters themselves. The difference in misorientation starts off large (close to 55°) near the baseline case and becomes lower toward the more extreme reduction case (lower right tiles). This can be attributed to the fact that $\Sigma 3$ boundary positions are more sensitive to changes in reduction which skews the distribution towards a higher value. When reduction parameters are varied minimally, the contribution of $\Sigma 3$ boundary motion is much larger than normal grain boundary motion. As the reduction parameters are varied to a larger degree, contributions of both $\Sigma 3$ and regular boundaries are found. In the more extreme cases, the contribution of point-to-point misorientation with values $\Delta\theta \geq 1.0°$ represent 18% and 24% of the total measured area for LoG and original methods, respectively. This initially appears to be a very large percent of the total area to change, but the boundary voxels represent 24% of the total area since this is a fine-grained material.

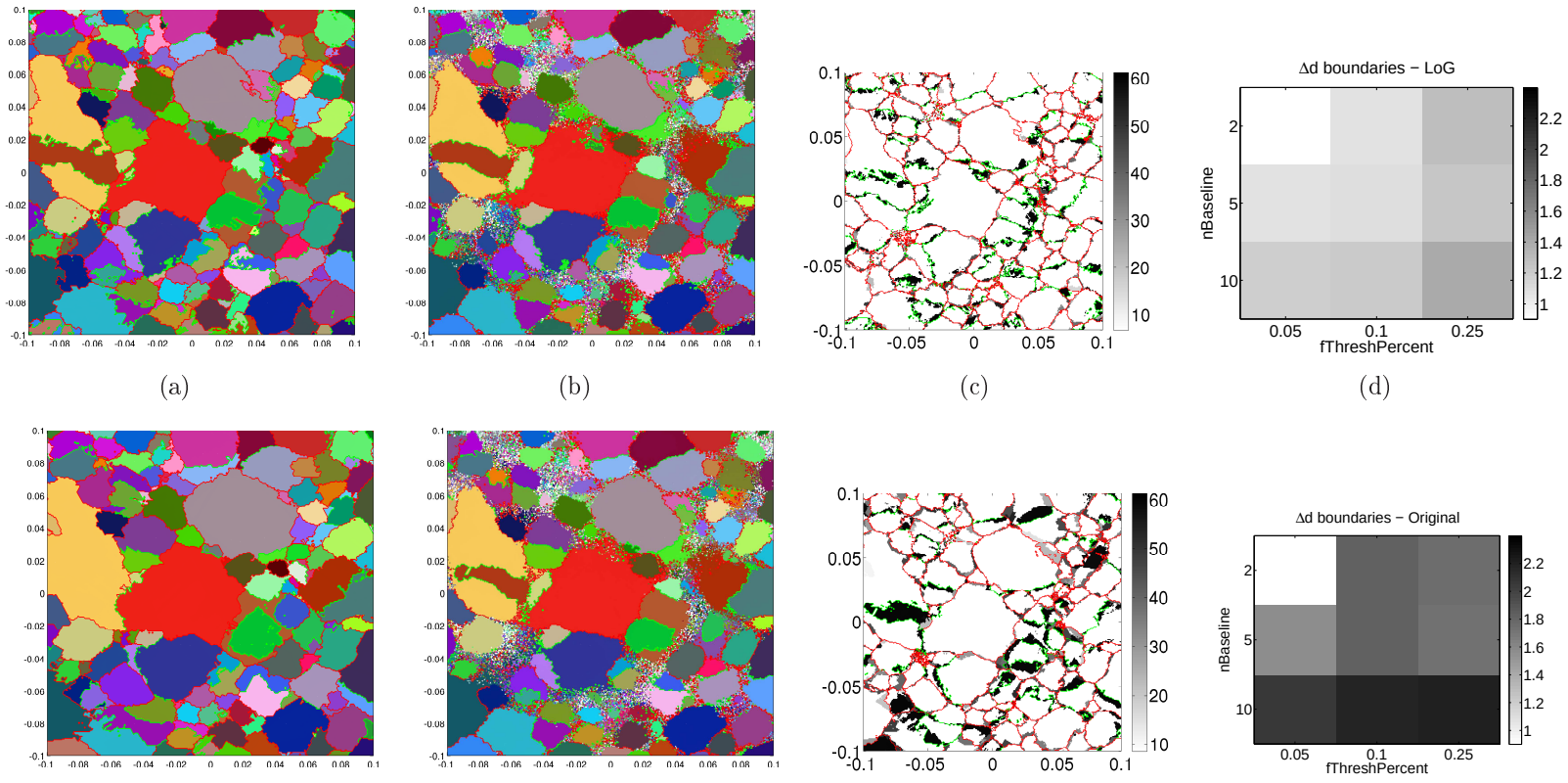


(a) (b) (c) (d)

(e) (f) (g) (h)

Figure 2.24: Each row in order left to right represents the $200\mu m \times 200\mu m$ patch of reconstructed microstructure for $nBaseline = 2$, $fThreshPercent = 0.05$, the patch for $nBaseline = 10$, $fThreshPercent = 0.25$, point-by-point misorientation of the first two microstructures with boundaries overlayed for the $nBaseline = 10$, $fThreshPercent = 0.25$ reconstruction, and mean boundary distance in the reduction parameter space of varied $nBaseline$ and $fThreshPercent$. The $1^{st}$ row (a)-(d) represents results from the LoG method, and the $2^{nd}$ row (e)-(h) represents results for the original method. The scale for (c) & (g) is in degrees (°); the scale for (d) & (h) is in microns ($\mu m$).

While the metrics to study microstructure variation initally presented in Figure 2.23 do not capture any significant changes between the two image processing methods, their quantification of microstructure and microstructure differences are somewhat basic. Figure 2.24 represents a better quantification and visual representation of the microstructure change as a function of image processing. Figures 2.24(a) & 2.24(b) present side-by-side the microstructure returned at the extremes of the reduction paramter space for the LoG method; figures 2.24(e) & 2.24(f) present that for the original method. By visual inspection, one notes the degradation of the microstructure by way of hashy regions when going from loose reduction parameters to more restrictive ones. While some regions suffer as expected with the loss in signal, focusing on several sub-regions, one notices subtle differences in boundary positions as well as grains appearing and disappearing. Figures 2.24(c) & 2.24(g) shows visually the difference between the two microstructures both in boundary moved, new grain appearance, and grain disappearance. One notices that figure 2.24(c) is much lighter than figure 2.24(g) showing little change in the microstructure returned even in extreme changes in reduction parameters. One example of this is the brown twin within the yellow parent grain in the upper-left region of the orientation maps whose boundary changes slightly for the LoG method, but only appears as reduction parameters become more restrictive in the original method. This is manifested by the large black stripe within that region in the point-by-point misorientation figure.

Seeking a more quantitative approach, the degree to which boundaries move as reduction parameters is studied. Those boundaries which do not move, defined here as moving less than $\frac{1}{2}$ of the voxel size, are ignored. Movement of boundaries is studied against the baseline case ($nBaseLine = 2$, $fThreshPercent = 0.05$) in a similar presentation to that in figure 2.23. Boundary segments are classified by the coordinate of their mid-point, and the orientation of the grain on each side of the segment. $0.5\mu m$ is used as the minimum distance criteria for observable motion; in an equilateral triangle mesh with side-width, $sw$, the minimum distance between any pair of unique mid-points is $\frac{1}{2}sw$. Matching boundaries from one microstructure to another required a minimization of distance between the mid-point of a given boundary segment in one microstructure and all others in the other microstructure while enforcing that the orientations on both sides of the given boundary segment must match with the segment in the other microstructure. This is accomplished by requiring the misorientations to both be $\leq 0.5°$.

Of those boundary segments that had moved more than $0.5\mu m$, their mean value is found and shown as a function of reduction method and reduction parameters in figures 2.24(d) & 2.24(h). Movement of between 50% to 90% of boundaries is found for each method depending on reduction parameters, with 90% moved when $nBaseLine = 10$ and $fThreshPercent = 0.25$. The figures clearly show that distance moved as reduction parameters are varied is much less for the LoG method. Mean distances between boundaries in different cases with the LoG method vary between 1.1 to 1.4 $\mu m$, while the original method varies between 1.6 and 2.2 $\mu m$.

The range of mean distances moved is $0.3\mu m$ for the LoG method and $0.6\mu m$ for the original method, again indicating stability in microstructure returned for the LoG method. Mean distances between corresponding boundaries across reduction method are calculated between figures 2.24(a) & 2.24(e) as well as figures 2.24(b) & 2.24(f) resulting in $\Delta d = 2.12\mu m$ and $\Delta d = 1.17\mu m$, respectively.

In this section, a study of microstructure difference as reduction method and parameters varied was presented. Quantifying the differences involved measuring distances moved as reduction type was varied. It was found that overall microstructure change was minimal for the LoG method across a large range of reduction parameter as compared to the original method. The fact that the LoG method results in a more stable returned microstructure (less sensitive to image processing) suggests it represents more faithfully the actual measured microstructure. Since nf-HEDM is thought of as a microstrucutural microscope, one can liken the LoG method as a lens with sharper focus and larger focal depth than the original method.

## 2.6 Conclusion

In this chapter, the importance of image processing and segmentation to the near-field High Energy X-ray Diffraction Microscopy (nf-HEDM) experiment pipeline was motivated. The salient features of nf-HEDM images was discussed. The original method of segmentation was reviewed. Discussion of the type of errors in image segmentation and how they might affect the output of the Forward Modeling Method (FMM) proceeded. A guideline was presented showing the requirements to upgrade the segmentation method which would accommodate robust high through-put while incorporating salient scattering features into the method.

The Zero-Cross Laplacian of Gaussian (LoG) method, implemented in C++ with MPI capability was introduced to solve some of the original method's deficiencies. The remaining parts of the chapter involved a side-by-side comparison of the newly proposed method and the original method. Initially an example of how this new method operates on images was shown and resulting segmentation of the same image with both methods was compared. At this point, claims of better segmentation via the LoG method could only be validated in the context of comparing resulting FMM reconstructions which would indicate segmented signal was consistent with single crystals diffraction in a polycrystalline material.

Comparisons began at a coarse microstructural level being examined and proceeded into a more fine detailed look. The LoG method was shown to have improved sensitivity to grain boundary position by way of more rapid decrease in spot overlap. The LoG's ability to extract enough signal in deformed materials allowed for microstructure to be successfully reconstructed with FMM when previously it failed. Improved spatial resolution was found for the LoG method by looking at how boundary positions varied from an expected physical phenomena, the coherent $\Sigma 3$. With improved spatial resolution, naturally smaller features would be expected to be found.

This was shown in an anecdotal way but follows logically from the previous observation. Arguments for better spatial resolution due to more better defined diffraction spots led to discussion on how these result in a possible sensitivity increase in reciprocal space. Intragrangular orientation variation was studied, and generally more physical-looking IGM and KAM maps were returned when using the LoG method. Due to the differences seen in FMM results depending on the way diffraction images were segmented, microstructure variation with segmentation routine and parameters was investigated to see how sensitive the resulting microstructure was to reduction parameters. The LoG method was found to result in a much more stable microstructure even as reduction parameters were varied. These studies and observation make it clear that improved image segmentation is beneficial to the already robust FMM and that the original method should be abandoned and replaced with the LoG method in all cases of nf-HEDM experiments. Constrained inputs to the FMM method do indeed produce higher fidelity results. The improved speed and flexibility in handling various types of materials studied makes user intervention minimal at this stage of the data processing pipeline and allows for more time to be spent actually doing science.

At this stage in development, nf-HEDM and FMM, experiment through meshed result, is not a black-box from which fine detailed results can be produced without any knowledge of the inner workings. Various automation, such as the proposed advanced segmentation method, is being developed to eliminate user intervention or expertise when not necessary. It is the author's opinion that this will never become a fully-robotic technique (drop and measure), but it will become less and less of a heroic feat to do a detailed non-destructive microstructural investigation.

# Chapter 3

# Plastic Deformation of HCP Zirconium

## 3.1 Introduction

Characterizing and understanding of material properties (e.g. electrical or thermal conductivity, magnetic permeability, Young's modulus, refractive index, etc.) are essential to applicability in modern industry and technology. For a particular purpose, a selecting the appropriate material is based in one or few of these properties and how they can be modified to suit the desired purpose. One example of this would be the use of silicon for transistors because of its sensitivity to electrical conductivity change as a function of doping [30]. The entire electronics industry is predicated on this single material property of silicon – its electrical conductivity. Various techniques or instruments are created for measuring these properties; processing methods are developed to modify and typically enhance those properties. Through much characterization large materials databases have been compiled and make decision on which material to use for a specific purpose. Research and development to understand how processing affects these properties allows for optimization of the material. Selection and refinement of a material for the targeted function is only possible with these kinds of studies and can lead to monumental breakthroughs in ~~*applicability*~~.

The current importance of zirconium and its alloys lies in its small absorption cross-section ($\sigma_A$) of thermal neutrons. This property allows for thermal neutrons to pass through virtually undisturbed. Zirconium's permeability to thermal neutrons makes it an ideal for cladding to surround fuel rods in nuclear power plants. The cladding allows for fission to occur within without the cladding itself becoming radioactive. One of the initial stages in nuclear core meltdowns occur when internal high-pressures tear the cladding away from the radioactive core [31].

Controlling tensile forces that could ultimately lead to core rupture depends on proper interlocks to prevent macroscopically unfavorable internal pressures. Engineering to produce specifically textured cladding taking advantage of the crystal

anisotropy could provide larger working ranges for safe operation. The ability to engineer this advanced cladding would require better fundamental understanding of crystal plasticity at the polycrystalline level as well as manufacturing techniques to generate desired textures. Refinement of models through experimental validation are critical in this goal. The advancement of grain-boundary engineered (GBE) materials then presents a reasonable development cycle that could be emulated.

In this chapter, an in-situ study of the bulk polycrystalline response of zirconium to tensile deformation is presented. Near-field High Energy X-ray Diffraction Microscopy (nf-HEDM) is used to measure the same volume of material as it undergoes increasing levels of plastic deformation. Investigation into microstructure evolution is discussed both at the global microstructure level, grain-to-grain (or grain boundary) interaction level, and single grain level. Results will be placed in context with previously observed texture development, expected single crystal behavior, and comparison with polycrystalline micromechanics simulations.

## 3.2 Crystal elasticity simulation

The way in which a polycrystal deforms depends on many variables such as its orientation, its neighbor orientation, and the resulting local stress state. Depending on the microstructure grain ensemble, there are innumerable configurations of stress distribution in each grain that can satisfy the overall macroscopic stress constraints. Since nf-HEDM output currently does not resolve the strain tensor and thus cannot determine the stress tensor, a purely elastic FFT-based polycrystal mechanics models [32] is employed to estimate the stress state for each individual point in the experimentally measured microstructure.

To perform the elastic FFT calculation, the voxelized S0 data is converted onto a rectangular-grid of comparable mesh resolution with element sizes ($2.18\mu m \times 2.18\mu m \times 4\mu m$). The appropriate input file format is a list of grid elements (one per line) indicating orientation, position, grain ID, and phase: $[\phi_{1,i}\ \Phi_i\ \phi_{2,i}\ x_i\ y_i\ z_i\ GID_i\ N_{ph,i}]$. The resulting input structure represents $512 \times 512 \times 50$ elements. Material elasticity properties are also supplied including the shear modulus ($\mu$), bulk modulus ($K$), Young's modulus ($E$), and the symmetric stiffness tensor ($C_{ijkl}$). These single crystal material properties will guide the simulation in equilibrating the macroscopic stress applied. The elastic FFT method will produce the stress and strain state of each element through an iterative process that allows the microstructure stress to equilibrate to the imposed macroscopic stress. Figure 3.1 presents a few of the grains. A single component of the strain tensor ($\epsilon_{22}$) is presented to illustrate the output that is generated from the simulation. There is a noticeable variation in strain (and stress) between grains and also within grains. Due to the single crystal elastic anisotropy, different grains are expected to bear different amounts the overall stress according their orientation, and this figure presents that case. Up until this point in this document, any reference to $\tau_{RSS}$ has been calculated under the assumption of

a homogenous stress state in all grains that is equivalent to the macroscopic stress. Clearly this assumption is naïve, and this simulation should provide a more reliable representation of the internal grain stresses. Several experiments have validated the model [33, 34].

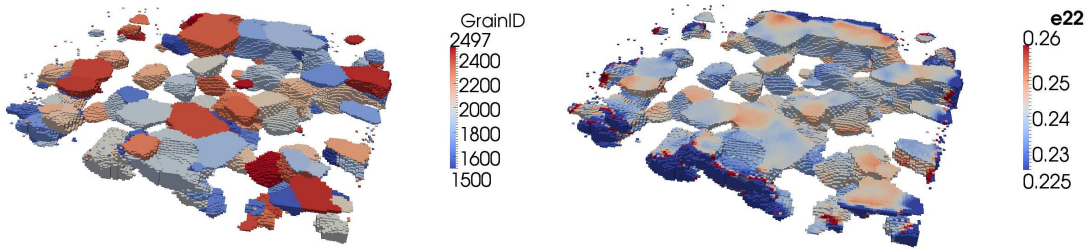


(a) (b)

Figure 3.1: (a) Some of the grains input to the 3D microstructure simulation. (b) One of components of the elastic strain tensor returned by the simulation. Local strains are returned for every Fourier grid point in the microstructure.

## 3.3 Motivation

The study of plastic deformation of polycrystals cannot proceed without first treating the case of single crystals. In the chapter, Miller indices will be used to define specific crystal directions, $[uvw]$, or the family of symmetrically equivalent directions $< uvw >$. Similarly, specific crystal planes are defined as $(hkl)$, or family of planes, $hkl$. For HCP materials, sometimes a 4-index convention is used with non-orthogonal direction such that directions are labeled as $[uvtw]$ or $< uvtw >$, and planes labeled as $(hkil)$ or $hkil$. Elasticity is the reversible stretch and shear of the lattice; plasticity is deformation is the irreversible. One recognizes that the material properties depend on the orientation of the lattice and is encompassed by the term "crystal anisotropy". Figures 3.2 and 3.3 represent inverse pole figures (IPF) for the variation in resolved shear stress (RSS,$\tau_{RSS}$) on a particular slip system depending on crystal orientation using Schmid's Law [35].

$$\tau_{RSS} = \cos(\theta)\cos(\phi)\ \sigma = m\ \sigma \tag{3.1}$$

In this case, $\sigma$ is constant (100 MPa). $\theta$ and $\phi$ are the angles between slip direction and tensile direction, and slip plane normal and tensile direction. The product of the cosines of those angles ($m$) is the Schmid factor which can vary from [-0.5 0.5] owing to the orthogonality of slip systems. For face-centered cubic (FCC) metals in figure 3.2 and away from extreme values, $\tau$ will vary by a factor of roughly 1.4. For hexagonal close-packed (HCP) zirconium in figure 3.3 and away from extreme values, $\tau$ will vary by a factor of roughly 7. Numerous single crystal tension and compression

experiments are performed to determine the critical resolved shear stress of a given slip system ($\tau_{CRSS}$, a material constant) and also validate Schmid's Law. Due to this large difference in RSS depending on direction of applied force, zirconium is considered more mechanically anisotropic (shows more anisotropy for this mechanical property). Zirconium is more anisotropic in other lattice properties as well, and typically lower symmetry lattices tend to exhibit more pronounced anisotropic effects.

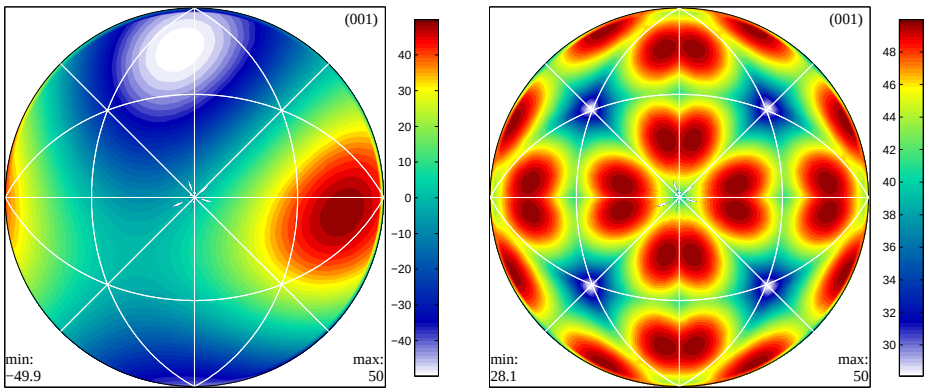


(a) (b)

Figure 3.2: IPF indicating the RSS on one or several slip system depending on the direction of applied force for a typical FCC metal. IPF plots are shown in the lattice frame. White lines represent the inherent crystal symmetry planes. The horizontal direction corresponds to the [001], vertical to the [010], and out-of-the-page to the [001]. (a) is an IPF of RSS values for a single slip direction and planes. (b) is an IPF of RSS values for all FCC slip systems, slip in the $<1\bar{1}0>$ direction and on {111} planes (denoted $\{111\}<1\bar{1}0>$). Note the 24 copies of symmetric stereographic standard triangles in (b).

Figures 3.2 and 3.3 demonstrate the level of anisotropy in yielding for FCC metals compared with HCP zirconium. Due to the fact that $\tau_{CRSS}$ is the same for all active slip systems for FCC metals, there are particular orientations favorable for every slip system. For HCP zirconium, figure 3.3(e) shows that pyramidal<a> has no orientation favorable for its activation revealing that this type of slip is expected to be suppressed. Orientations that favor pyramidal<a> overlap heavily with those that favor prismatic slip, but $\tau_{CRSS,pyramidal<a>} \approx 2.5 \times \tau_{CRSS,prismatic}$. When stresses are applied roughly perpendicular to the c-axis([0001]), the prismatic $\tau_{CRSS}$ criteria will be reached before any other slip system has generated sufficient RSS to become active.

Above is a single crystal example of material property dependence on microstructure is the Hall-Petch effect [36, 37]. This observed phenomena finds the yield point in a stress-strain curve for polycrystalline material to depend linearly on the inverse square root of average grain diameter of the microstructure ($\sigma_y \propto d^{-\frac{1}{2}}$) [38]. Com-

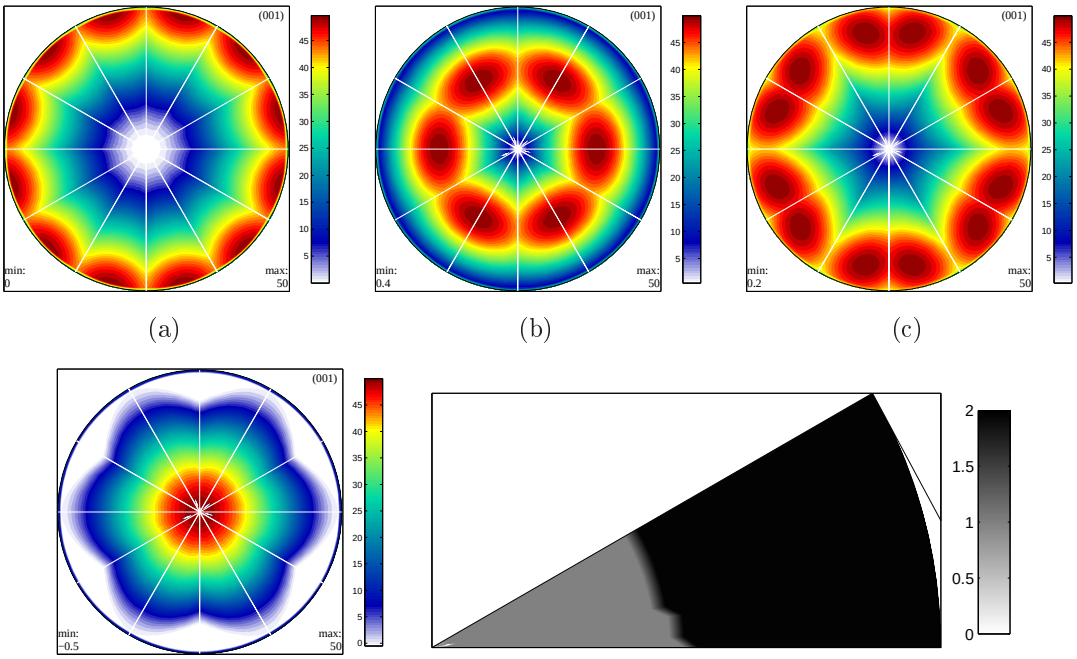


Figure 3.3: IPF indicating the RSS on several slip system depending on the direction of applied force for zirconium. (a) is IPF of RSS values for all prismatic slip systems $<2\bar{1}\bar{1}0>$ and $\{01\bar{1}0\}$. (b) is IPF of RSS values for all basal slip systems $<11\bar{2}0>$ and $\{0001\}$. (c) is IPF of RSS values for all pyramidal<a> slip systems $<11\bar{2}0>$ and $\{10\bar{1}1\}$. (d) is IPF of RSS values for all tensile twin systems $<\bar{1}011>$ and $\{10\bar{1}2\}$. Note the 12 copies of symmetric stereographic standard triangles in (a)–(d). Given the redundancy in showing symmetrically-equivalent standard triangles, typically a single triangle is plotted with the remaining implied. This will be the standard convention for IPFs later in the chapter. (e) shows the single standard triangle with grayscale value denoting which slip system will activate first depending on orientation and weighted by $\tau_{CRSS}$ of the different slip systems. White (0) corresponds to pyramidal<a> slip, gray (1) to basal slip, and black (2) to prismatic slip.

plementary to the findings of yield strength dependence on crystal orientation, the Hall-Petch effect demonstrates that grain size, and most likely shape, need to also

One recognizes that a polycrystal does not deform as N-independent single grains would deform. Stress and strain compatibility at grain boundaries requires shape change and force transfer. Models with either macroscopic stress or strain assumptions have been developed (Taylor, Sachs, Taylor-Bishop-Hill[TBH]) which predict a grain's deformation within its polycrystal framework [39, 40, 41, 42]. The Taylor model assumes iso-strain for all grains in the polycrystalline aggregate leading to a grain stress state that represents the contribution of weighted multiple slip systems

that minimizes the work performed by the strain. Boundaries are preserved but stress continuity cannot be imposed. The Sachs model, on the other hand, assume iso-stress for all grains in the polycrystalline aggregate leading to single slip activation by CRSS criteria. Boundaries are not preserved but stress continuity is guaranteed [43].

The development of more modern computationally-based crystal plasticity modeling has helped overcome the assumptions required with earlier models. These new models make no assumption about individual grain stress or strain from macroscopic boundary conditions. These macroscopic conditions are applied, and local stress and strain conditions are found iteratively while obeying stress and strain compatibility within the grain-to-grain network. One of these methods is crystal plasticity finite-element (CPFE) modeling [44]. This is simply application of crystal plasticity rules in the confines of a meshed structure. FE modeling is currently extremely successfully practiced in academic and industrial research at predicting stresses, heat flow, dynamics, etc of designed simulated parts before creation and distribution. It is utilized so heavily due to being based on sound physical models which in this case are physical laws (Newton's laws, laws of thermodynamics). The crystal plasticity fast Fourier transform (CP-FFT) method relies on computation time saved by converting a convolution integral into a product in Fourier space [32]. Its temporal improvement over traditional CPFE allows one to potentially investigate larger more representative microstructure volumes with the same spatial resolution as CPFE while having shorter runtimes. It is through experimental validation that confidence in CP models can be achieved.

Phenomenology guiding simulations defines the current approach of microstructure research. The physical phenomenology of various deformation mechanisms is understood through numerous empirical observations. Single crystal properties are well understood; it is how they interact as polycrystalline materials that is not completely straightforward. More sophisticated modeling techniques are currently being developed with need for access to 3D data for validation. Recent developments in non-destructive experimental microstructure mapping techniques, such as nf-HEDM, are capable of providing calibration and validation of models at multiple steps of microstructure evolution. The experiment here can define the physically observed progression while the model can try to replicate and predict the microstructure transformation.

Further the present study of deformation evolution in HCP zirconium might provide insight for future modeling efforts in other HCP metals of interest. Given the lack of available non-destructive 3D microstructure data and limited on-going research on HCP metals, results might have while potentially more wide-spread benefits to the entire field. Looking forward from an engineering perspective, lightweight HCP magnesium is expected to overtake aluminum in many structural capacities. Understanding deformation mechanisms then in HCP metals will be crucial given the strong anisotropic effects.

## 3.4 Sample preparation

One of drawbacks to performing synchroton experiments that the ratio of actual experiment time to preparation time is low. Targeted experiments are performed usually with one or two beam time allocations. Waiting time from proposal submission to beam time can take multiple run cycles which amounts to months or even years. For this reason, a considerable amount of preparation is performed to obtain initial microstructures suitable and appropriate for measurement. If most scientists were only given a few days per year to collect data rather than having the option of repeating measurements daily in their own lab, considerable care would be taken to pick the best sample for measurement. This rational is the reason for the considerable amount of initial preparation and lead-time that were used for this experiment.

A plate of clock-rolled high purity (99.95%) zirconium was obtained initially for testing purposes from Los Alamos National Laboratory. The plate measured approximately $175mm$ in diameter and $9mm$ in height. Two small $400\mu m$ square cross-section samples were cut from the plate to determine the as-received microstructure properties of the plate (grain size and texture).

These samples were measured at APS using the nf-HEDM setup in August 2010. One sample was measured with no annealing treatment to find the as-received properties. The other was annealed in a quartz-tube furnace setup while flowing forming gas ($97\%N_2$, $3\%H_2$) for 1 hour at $T = 850°C$. This temperature was chosen because the homologous temperature (fraction of melting temperature) for recrystallization is typically taken as $T_H = 0.4$; T was chosen slightly above this such that T=$0.5T_{melt}$ [45]. This would ensure that if substantial deformation was initially present, large grains would be present in this sample.

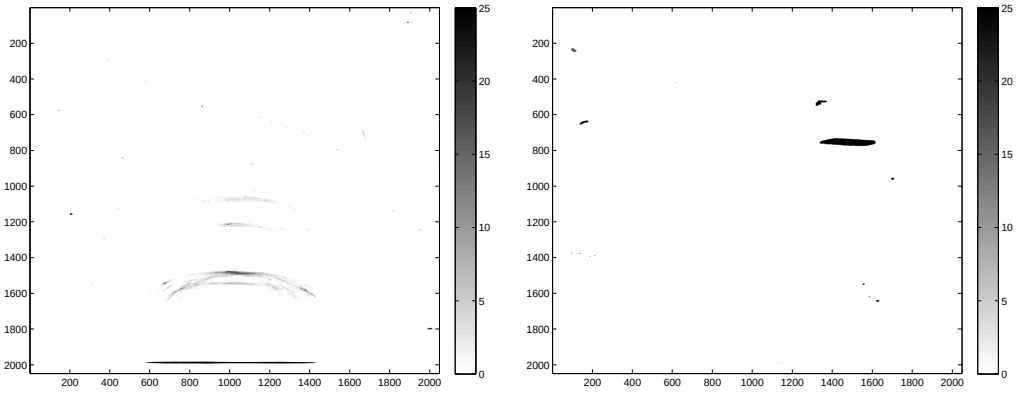


(a) (b)

Figure 3.4: (a) shows single scattering image for as-received zirconium. (b) shows for the sample annealed for 1 hour at 850°C.

From figure 3.4, the two samples showed very different underlying microstructures. Figure 3.4(a) shows essentially a powder diffraction pattern when sample size to de-

tector distances are of the same order; this is the near field operating regime. Figure 3.4(b) shows one very large peak and a few small spots. By analyzing just the size of the large peak, its width is roughly the size of the entire sample. FMM reconstructions confirmed this fact, the annealing schedule was at too high temperature for too long resulting in a mostly single crystal piece of zirconium. This measurement and reconstruction represented the first successful venturing of nf-HEDM into non-cubic materials (no small feat).

After considerable care was taken to put in place software required to analyze HCP materials, an annealing schedule still needed to be determined to produce *polycrystalline* zirconium. One could perform this task through a series of optical microscopy of polished surfaces after annealing or EBSD measurements; however the longer lead-times allowed for using residual beam time to characterize a few more prepared samples with sample anneal times but lower temperatures (600°C and 750°C ). These samples were $750\mu m$ diameter zirconium cylinders obtained by electric discharge machining (EDM). A single nf-HEDM layer measurement was performed on each of these samples shown in figure 3.5. Each layer measurement required roughly 30 minutes of beam time. This short measurement provided considerable calibration on how to obtain desired grain sizes. Initial analysis of the diffraction spots leads to an estimate of $\sim 20\mu m$ grain sizes for the 600°C sample, while the analysis for the 700°C measurement estimates $\sim 200\mu m$ grain sizes. Ultimately the grains obtained by 600°C might be too small to resolve orientation gradient development during deformion, while 700°C would not provide enough grains in the volume to constitute a large statistical sampling of microstructure boundaries to investigate.

While waiting several months to do a grain size versus annealing schedule study seems completely infeasible, this was completely overcome by the efficiency in which it yielded results. The total amount of human time required for generating sample, performing anneals, collecting diffraction images, and analyzing results was on $\mathcal{O}(10^1 Hr)$; Performing the same study with optical microscopy or EBSD would have taken $\mathcal{O}(10^0 Month)$. The expertise gained and availability of synchrotron x-rays allowed for this study to be performed with little effort. The ability to absorb such large lead-time to perform studies also helps. As a result, 650°C for 1 hour was chosen as the final anneal schedule for samples to be used in the in-situ deformation experiment.

## 3.5 nf-HEDM compliant load frame

In this section, the design and building of an in-situ micromechanical load frame is presented that complies with the nf-HEDM geometry while allowing all goals of the experiment to be acheived unhindered. Some of the necessary requirements put forth included

1. **Radial footprint $< 150mm$.** HEDM experiment is a rotating crystal method which implies the main parts of the entire apparatus with rotate above or below

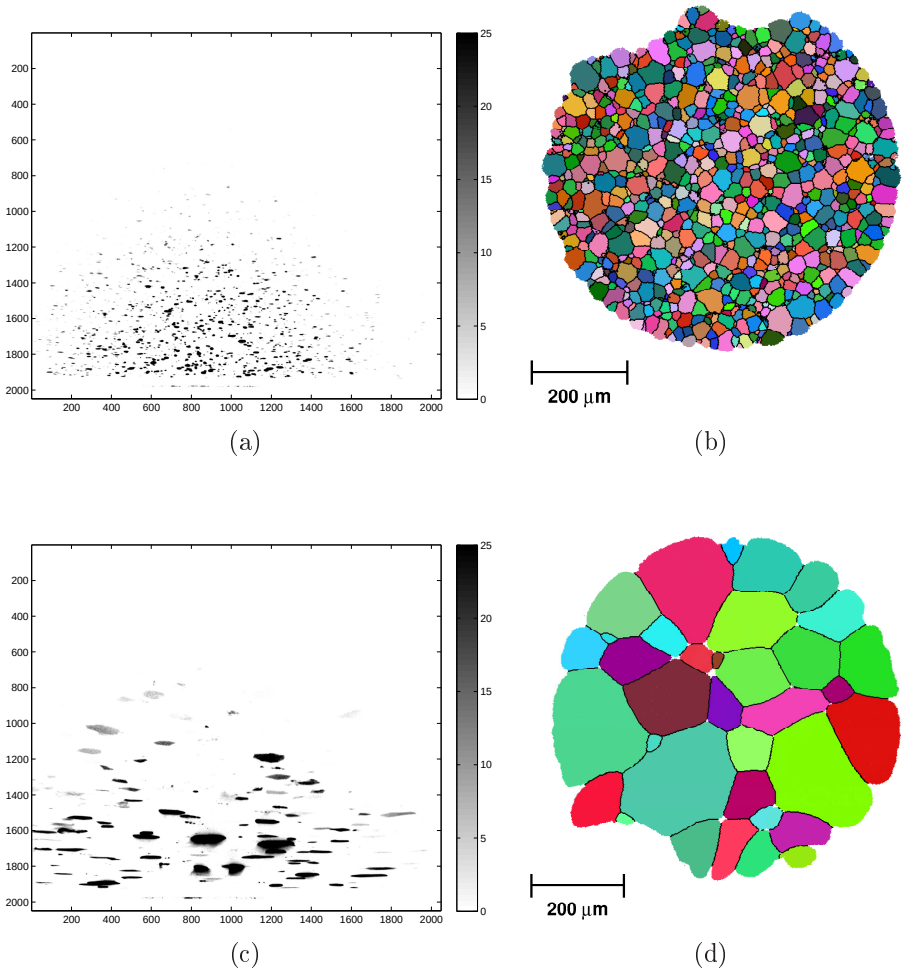


(a) (b)

(c) (d)

Figure 3.5: (a) and (c) shows single scatterings image for the sample annealed for 1 hour at 600°C and 700°C, respectively. (b) and (d) show the reconstructed orientation maps linked to (a) and (c).

the x-ray plane (in this case, below). To avoid hitting the detector housing below during rotation, the entire frame needed to have a compact rotational footprint. This restriction could not be relaxed without a complete redesign of the detector housing.

2. **Total height** $< 200mm$**.** Constraints on the height of the mechanical frame come from the fixed veritcal position of the x-ray plane and the stack of motorized stages below it on the lowered optical bench. This restriction could not be relaxed without replacing tearing down the experiment, removing or replacing translation and rotation components, and completely recalibrating the entire setup.

3. **Total weight $< 100N$.** This represents the total weight allowed on the translation stages that would hold the load frame before causing mechanical damage to the motor teeth.

4. **Enhanced x-ray transparency through load bearing element (LBE).** Previously deformation experiments used a semi-transparent ceramic LBE which produced added background on the detector. During deformation signal dimishes, this is an attempt to maximize signal-to-noise reduction as plastic deformation proceeds.

5. **Minimal thickness of LBE.** nf-HEDM requires rotation-axis-to-detector distances $\sim$ 5-10$mm$ puts an upper-bound on LBE's outer radius (OR) $\leq 5mm$. Practically, this should be closer to 2-3$mm$. The largest OR ceramic LBE would break at desired higher loads.

6. **Maximum force delivered $\approx 200N$.** Interest in tracking $\sim 1mm$ zirconium samples from an initially undeformed state through ductile failure yields a minimum force requirement due to the material's ultimate tensile strength (UTS) and minimum cross-sectional area probed.

7. **Strain displacement steps $\lesssim 1\mu m$.** Interest in mapping elastic strains at expected experimental resolution ($\frac{\Delta L}{L_0} = \epsilon = 10^{-3}$) requires displacement control at or below this value.

8. **Force sensitivity.** Better monitoring on loading allows for determination of the onset of yielding. Experimental force-displacement (stress-strain) curves are necessary for determining modelling parameters later.

Items 1–4 represent the main geometric and x-ray considerations put forth by the nf-HEDM setup. Items 5 and 8 represent the requirements relating to inducing plastic deformation in $\approx$ 1mm size zirconium samples.

Before this load frame was designed and constructed, a decision was made whether this new apparatus was necessary. At this point, a nf-HEDM compliant load frame existed which was used in previous copper tensile experiments [21, 22]; however, these experiments had been performed on samples of $\leq 250\mu m$ diameter with copper which is a relatively soft material. Ultimately this apparatus could not meet the needs of items 3 and 5, it could only provide up to $10N$ of force (max). For a zirconium sample, this would restrict the measured cross-sectional area of a sample to be very small ($r_{eff} \approx 100\mu m$).

See figures 3.6 and 3.7 for better illustration of the load frame and sample geometry. The general load frame design can be described as a 4-post cage with stepper motor enclosed to provide tensile forces/strains. A force sensor is attached to the motor. A $4.0mm$ hole lies at the center of the top plate of the cage. A hollow cylinder ($2.83mm$ ID, $4.0mm$ OD) with part of its side cut-away is attached to the force

sensor and one end lies above the top plate through the hole. An x-ray transparent beryllium LBE tube with same OD and ID is placed above this. Another similar hollow tube of shorter length is place above the beryllium with one side tapered to accept the sample. The sample is then slide through this stack of tubes, a dowel pin is then slid through the cut-away of the first tube and the radial hole at the bottom of the sample. The stepper motor is moved up, moving the entire stack up until the dowel pin contacts the top plate. As the stack is driven further up pushing the top part of the sample upward, the fixed dowel pin keeps the bottom part of the sample fixed. The main mechanical components of this load frame (pillars, plates, sample, beryllium tube, and tube with cut-away) were tested virtually using ABAQUS [46] before fabrication.

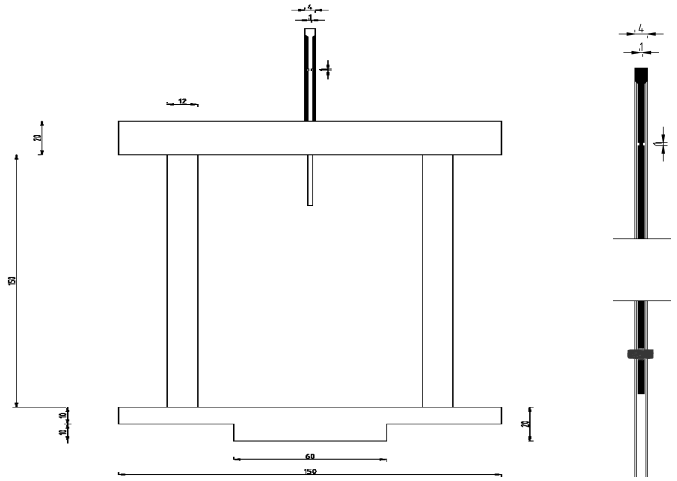

(a) (b)

Figure 3.6: Load frame design figures. (a) shows the drawing for the 4-post load frame cage with sample and load bearing sleeve. The bottom plate is mounted directly to the nf-HEDM setup. Not pictured is the force generating stepper-motor and force sensor which sit between the two posts and is mounted to the bottom plate. (b) shows a close-up representation of the sample and sleeve design with pin inserted.

The bulk of the design involved around obtaining a fine step resolution, lightweight, and compact z-stage to generate tensile forces; the rest of the design concerned building a framework around this stage. For this purpose, an *OWIS HVM-200* elevator stage was purchased with specifications

Radial footprint = $144mm$
Height at full extension = $59mm$
Weight = $50N$
Max force = $200N$
Full-step resolution = $2\mu m$

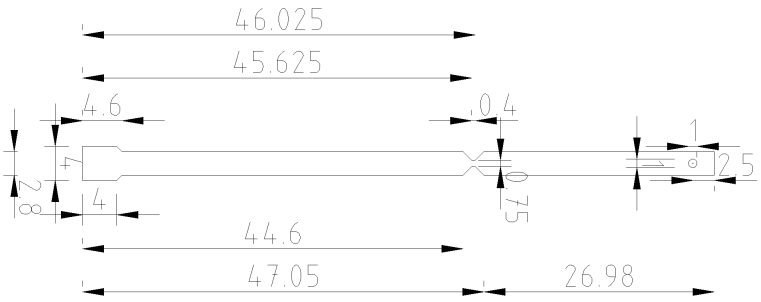


(a)

(b)

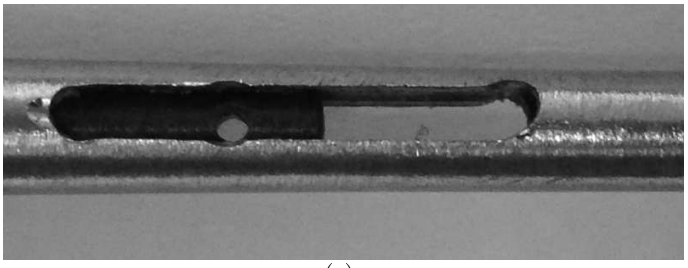

(c)

Figure 3.7: (a) and (b) shows the digital and physical sample. (c) shows the mechanism devised to allow for tensile force reversal.

which fulfilled items 1–3, 6, and 7. Also a 20mm length beryllium tube of S-200F grade with ID of $2.83mm$ and OD of $4.0mm$ was order and machined by *Materion*. Beryllium was chosen to be the LBE due to its high strength-to-weight ratio and also low Z value which makes it transparent to high energy x-rays. The thickness of the beryllium was conservatively chosen such that it could withstand up to $1500N$ in its elastic regime; given the sample itself can only support $\approx 200N$ and the stage can only provide this much force, the beryllium LBE is guaranteed to stay below 15% of its yield strength (YS). This somewhat extreme safety precaution was taken to avoid entire hazardous material containment of the experimental hutch if it broke. Use of beryllium over the original ceramic LBE accomplish items 4–6. Finally a *Transducer Techniques MPL-75* load cell was utilized with range up to $335N$ and sensitivity of $0.67N$ accomplishing item 8. All of the parts were designed such that the breaking of the sample neck would provide a fail-safe mechanism to avoid damaging any of critical components the apparatus.

## 3.6 Deformation experiment

A few zirconium samples of geometry and were machined and annealed in preparation of beam time at the APS in August 2011. Measurement of the a single specimen proceeded starting on August $14^{\text{th}}$ at 9:30PM until August $20^{\text{th}}$ at 9:00AM with a single beam shutdown on the $16^{\text{th}}$. Typical shutdown days for the APS are Tuesday, and when an experiment begins on a Wednesday users have the advantage of installing their apparatus when there is no beam being delivered. This has the advantage of not wasting any precious x-ray time. Since apparatus installation requires several hours and this experiment started on a Sunday, the load frame was installed in the B-hutch (APS-1ID-B) on the shutdown day, August $2^{\text{th}}$, to maximize usage of allocated beam time.

The x-ray energy was set to 64.351 keV as a compromise between competing factors. Unlike conventional lab x-ray sources whose energy is linked to differences in energy of a target's electron shells, synchrotron radiation uses tunable period undulators allowing for selection of appropriate energy. The quantum efficiency of the 20 $\mu m$ thin LuAG ($Al_5Lu_3O_{12}$) scintillator used in this experimental setup was found to be peaked at $\sim$ 50keV, however, zirconium (Z=40) is found to have an attenuation length ($\frac{1}{e}$) = $250\mu m$ at this energy. This would amount to ($(\frac{1}{e})^4 \simeq 1.8\%$) x-rays being transmitted by a $1mm$ zirconium sample. The attenuation length of zirconium doubles to $500\mu m$ at 64.351 keV leading to a 14% transmission rate. This is an $e^2$ improvement at the cost of scintillating efficiency. Further, x-ray absorption tomography will suffer, if not fail, when attempting to image through many $\frac{1}{e}$ lengths of material. For this reason, 64.351keV was selected as the operating x-ray energy.

(a) (b)

Figure 3.8: X-ray absorption images of the top (a) and bottom (b) fiducial marks used to measure the gauge length. A red mark indicates the observed fiducial mark. Note in the image, black represents no attenuation.

Prior to any loading, the zirconium piece was measured using $1mm$ tall x-ray absorption tomography in a sequence of 10 white field images, 10 dark field images, 901 still-action images from -90° to 90° in 0.2° step, and a final 10 more white field images. Exposure times for tomography images were $0.14s$. Then 50 layers of nf-HEDM data were collected with spacing of $4\mu m$ between layers (S0). The layers

| Strain State | Neck length ($L$) $mm$ | Force reading $N$ | $Y_{max}$ $\mu m$ | $Y_{min}$ $\mu m$ | $Tomo_{max}$ pixel | $Tomo_{min}$ pixel |
|---|---|---|---|---|---|---|
| 0 | 2.094 | 0 | 126 | -74 | 1554 | 1689 |
| 1 | 2.106 | 41 | 130 | -68 | 1516 | 1650 |
| 2 | 2.172 | 109 | 98 | -102 | 1520 | 1655 |
| 3 | 2.192 | 106 | 96 | -105 | 1519 | 1655 |

Table 3.1: nf-HEDM measurement volume and conditions for the 4 states of deformation and their correspondence in absorption tomography measurements. Neck length was determined as the distance between two fiducial marks that marked the end of the gauge section shown in figure 3.8. $Y_{max}$ represents the position of the first HEDM layer ($z_1$) measured with respect to the minimum cross-sectional area of the necked region which is approximately the same as the mid-point between the fiducials. $Y_{min}$ represents the position of the last HEDM layer ($z_{50}$) measured with respect to the minimum cross-sectional area of the necked region. $Tomo_{max}$ and $Tomo_{min}$ are the pixel rows that match directly to $z_1$ and $z_{50}$, respectively. Higher pixel row values correspond to lower physical positions on the sample.

were collected at either 2 (or 3) detector distances which were 5.3, 7.3, (and 9.3) $mm$. Measurement at each detector distance consisted of 180 images pertaining to 180 contiguous sweeps of $\delta\omega = 1^\circ$. Exposure time for each image was $4.5s$. In the S0 state, measurement proceeded about the mid-point between the fiducials which is $50\mu m$ below the true mid-point of the gauge section as defined by smallest cross-sectional area. This fact was determined after S1 and measurement volumes were adjusted to be symmetric about that point. The sample was then subjected then loaded by upward motion produced by the stepper motor. The displacement of the sample was then held fixed while x-ray measurement took place so this was a stop-action measurement. This $1^{st}$ loaded measurement constituted the S1 state. Another $1mm$ tomography measurement was made, and 50 nf-HEDM slices were taken about the same point as in S0. The sample was pulled further, tomography was taken, and 50 more slices collected this time about the true mid-point of the gauge section (S2). The sample was driven even further at which point change in force per unit step became negative indicating the sample was well into the plastic regime. Diffraction spots had shown significant smearing at S2 and became worse at this point. Tomography was taken and 50 nf-HEDM layers collected about the true mid-point. With only $\sim$ 12 hours remaining of beam time and not enough to collect another state, 11 layers were mapped at $25\mu m$ spacing below the measured region to potentially map out strain level as a function of distance from the necking point. Finally the sample was pulled several more times with only tomography measurements made to track the sample shape. Note that tomography measurements of $1mm$ height only required 15 minutes to run whereas the nf-HEDM diffraction volume of $200\mu m$ required 16 hours. The sample was pulled until finally breaking with a total of 10 intermediate

tomography measurements taken. Correlation between the on-set of void formation with the initial microstructure measured in S0–S3 is discussed in section 3.14. Large voids were apparent visually during collection of the final tomographic scan.

The remaining sections in this chapter will present and discuss results from this data collection.

## 3.7 FMM Results and Grain Network

Diffraction images collected for the 4 x 50 layers plus the extra 11 layers were initially reduced by the original image processing method. The output was directed into the FMM routine for orientation map reconstruction. FMM routines were originally conceptualized and implemented by R. M. Suter in the form of analysis code called xdmmpi (X-ray Diffraction Microscropy-MPI), and further advanced by S. F. Li as IceNine. Experimental geometry was optimized via parameter monte-carlo routines. First initial S0 state was reconstructed layer by layer to a equaliteral triangle grid of sidewidth $2.81\mu m$. Each map had $240k$ voxels of independently assigned orientations; the entire volume consists of $12M$ spatially-resolved orientations. Due to recent speed-ups in the FMM reconstruction algorithm [3], each layer in the S0 state required $1k$ CPU-hr. Each orientation was fit using scattering vectors up to a $|\vec{Q}|_{max}$ of $8\text{Å}^{-1}$. For most orientations, this criterion meant that each orientation returned from the FMM routines uses $\sim$100 diffraction projections.

Reconstructions of the 50 layers of S1 were produced in the same way ($240k$ voxels at $2.81\mu m$ grid resolution using $1k$ CPU-hr). Considerable plastic deformation had been initiated at S2 requiring much longer reconstruction times. Initially little of the S2 volume would reconstruct necessitating some of the work presented in chapter 2. After that development, the diffraction images were re-processed. A few layers (z1, z24, z5) in S2 were reconstructed to this resolution but at a cost of $25k$ CPU-hr per layer. The remaining layers were fit to a coarser $5.63\mu m$ grid resolution. Reconstructions of the 50 layers of S3 were produced in the same way as S2 ($60k$ voxels at $5.63\mu m$ grid resolution using $2.5k$ CPU-hr). Some specific targeted grain neighborhoods eventually required finer resolution reconstructions in S2 and S3; these sub-regions were also reconstructed at $2.81\mu m$ grid resolution.Figure 3.9 shows the FMM reconstructions of the true mid-point of the gauge section from S0–S3. Those shown are z37 in S0, z37 in S1, z24 in S2, and z24 in S3 which is consistent with the volume mapping provided in table 3.1. Visual correspondence between the four orientation maps seems to indicate that nominally the same layer of material has been tracked across deformation states. Since this is the layer at smallest sample cross-section, it should represent the region of highest stress.

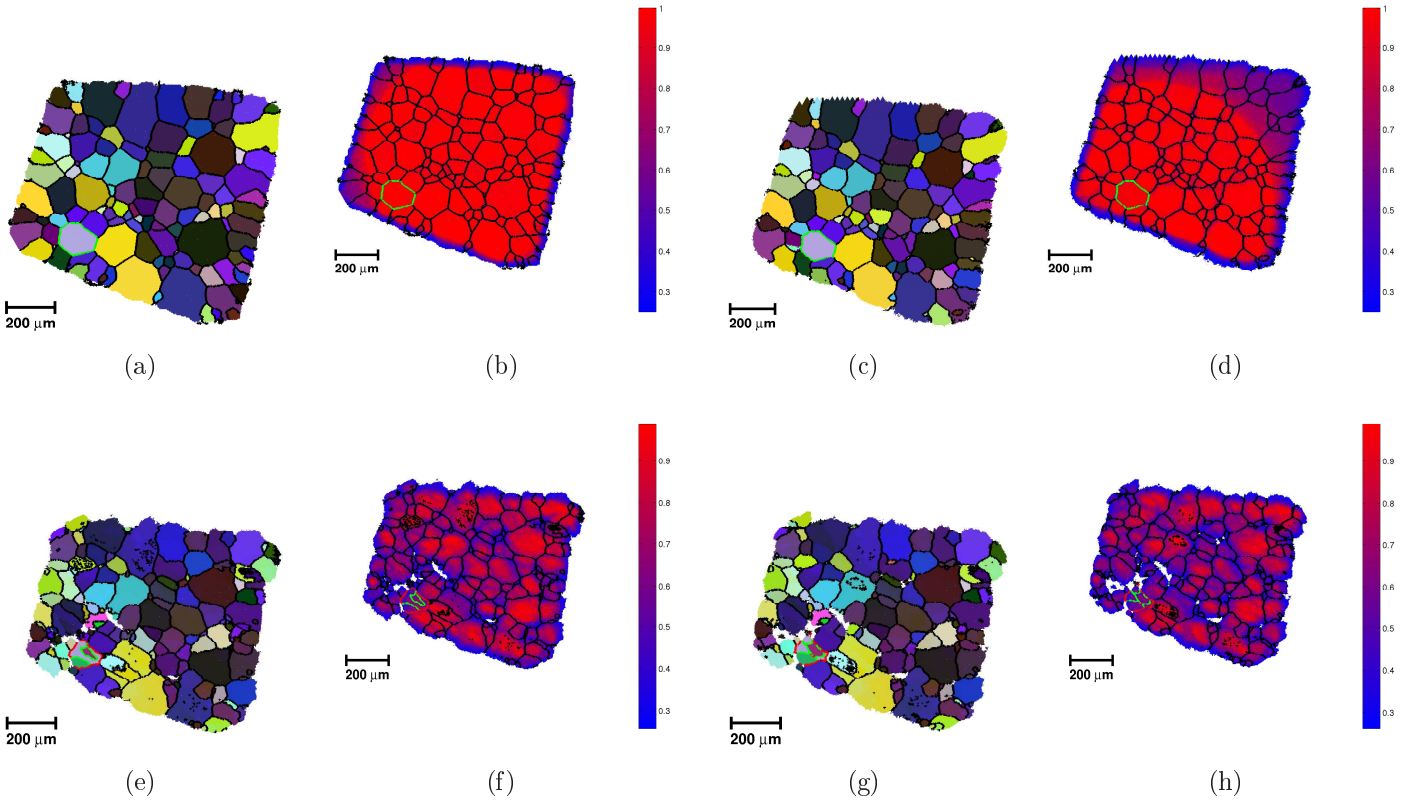


Figure 3.9: (a)-(h) Reconstructed maps of a single layer of the Zr microstructure in four different strain states. The circular shadow in (d) is due to an error in centering of the sample which lead to the upper right portion in the figure passing out of the x-ray beam as it rotated through the 180° measurement range. Black lines are drawn between neighboring voxels that have ≥5° misorientation, thus outlining grain boundaries in (a)-(d) and also indicating the onset of intragranular orientation variations in (e)-(h). The highlighted grain forms two $\{10\bar{1}2\}$-type tensile twins by S2 and these twins have increased volume in S3. Green lines in state S0 and S1 correspond to boundaries between the parent grain and all of its neighbors in this plane. Red lines in state S2 and S3 correspond to boundaries between the parent grain and neighbors, while green lines represent boundaries satisfying the twin misorientation relation 85.2°$<10\bar{1}0>$ within a 2.5° misorientation for each boundary segment. Two other grains in this section form twins as well.

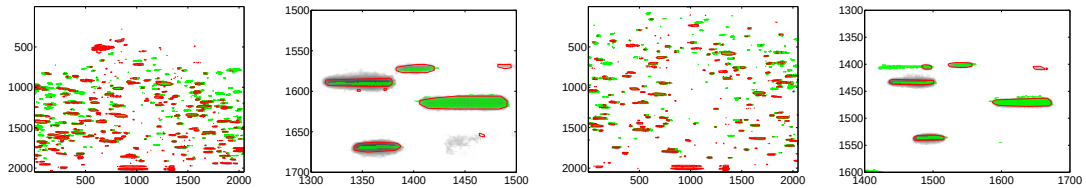


Figure 3.10: Scattering images of the same layer and rotation interval at different detector distances in S0. (a)–(b) were taken at L=5.3$mm$, while (c)–(d) were taken at L=7.3$mm$. (b) and (d) are zoomed in regions of (a) and (c). Red lines outline the reduced data that is input into the FMM reconstruction. Green dots are placed where the reconstructed microstructure places scattering.

To compare how well the returned microstructure replicates the scattering which was collected experimentally, one can generate the simulated scattering and overlay on top of the original scattering images as shown in figure 3.10. While the confidence metric proves to be useful at quickly ascertaining fit quality, there can be cases of artificially high confidence when reconstruction quality is poor. This check provides assurance that grain shapes returned do in fact match closely to shapes observed in the diffraction images.

Data mining can proceed on the stack of 50 reconstructed layers for each state or this collection of microstructure can be reduced into a grain network structure. Choosing the the later option, a grain map is defined by defining spatially connected (clustered) voxels with some similarity, in this case orientation, and defining them collectively as a grain. Here a grain has average properties including volume, center-of-mass position, and average orientation. Considering that the FMM makes no assumptions about the existence of grains, post-processing like this must be performed to obtain the grain network (GN), or grain graph (GG). Henceforth, all utilities developed to study grain network connectedness were developed in C++ with use of the $XDM++$ library. $XDM++$ is an in-house library primarily developed by S. F. Li with synergy between FMM reconstruction formats (.mic files), mic voxel grid, crystal orientation support, and connected component analysis through the C++– boost library.

After constructing a GN from the microstructure data, its representation is $\sim 10^4$ times smaller than the raw reconstructed microstructures. Temporarily ignoring the fine details of the entire microstructure, one can easily compute standard global microstructure statistics for individual states such as grain size distribution, neighbor number distributions, neighbor misorientation distributions, number of faces as a function of grain size, etc. Figure 3.11 represents a few of the simple statistics extracted from the reduced form of the entire microstructure volume. This form of the data makes searching and moving through the microstructure fast and efficient. While still being able to connect to the finely detailed 3D FMM reconstruction, this

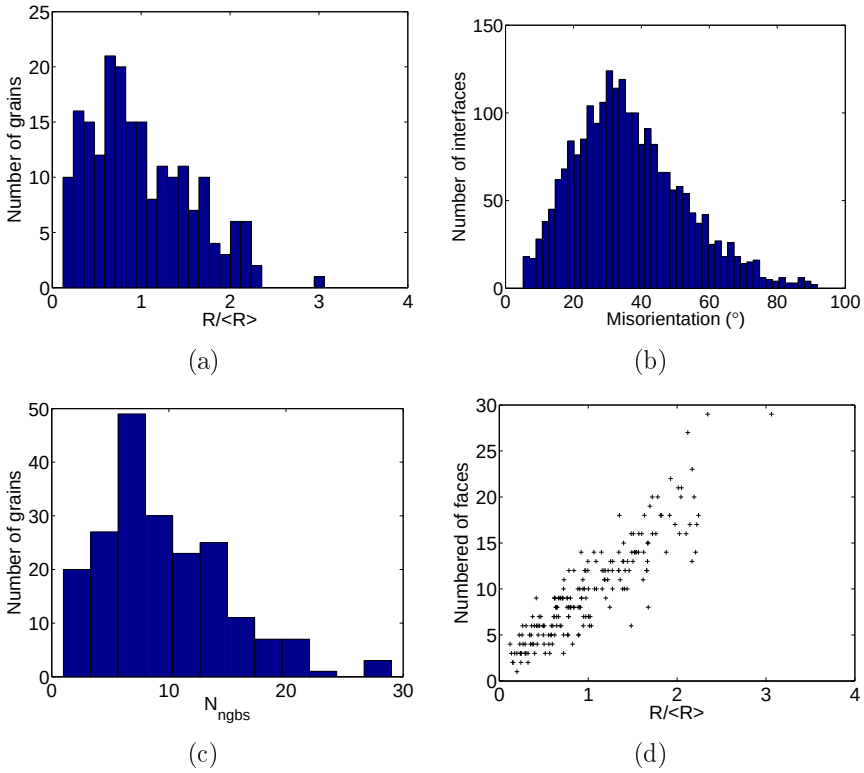


Figure 3.11: General 3D grain statistic for the initially measured zirconium microstructure. (a) shows grain statistics in the form of grain size (reduced radius) distribution. (b) shows grain-to-grain statistics from GN in the form of neighbor grain misorientation distribution. (c) the statistics of the GN itself. (d) shows the linear relationship between number of interfaces and grain size.

affords a multi-scale approach for studying microstructures.

One concrete example of how this data architecture could be beneficial in searching for deformation in so-called rogue grain pairs [47]. These are particular pairs of distinct grain orientations relative to a loading direction which One could easily locate these rogue grain pairs in the GN, which amounts to filtering out all edges in the grain graph that do not correspond to rogue grain pair criteria. One could then search the pairs that remain in the full high-resolution reconstruction for evidence of slip accumulation in the soft grain. For a system of $10k$ grains, this initial filtering could be performed in less than 30 minutes using $MATLAB$. Connections between the coarse GN scale and the FMM 3D microstructure will be used later to probe efficiently various microstructural scales.

At this point a digital representation of the $0.166mm^3$ experimentally measured zirconium sample has been reconstructed in at 4 levels of deformation (S0–S3) in the form of $12M$, $12M$, $3M$, and $3M$ spatially-resolved orientation elements. The data have further been reduced to a more manageable GN structure. Some pre-

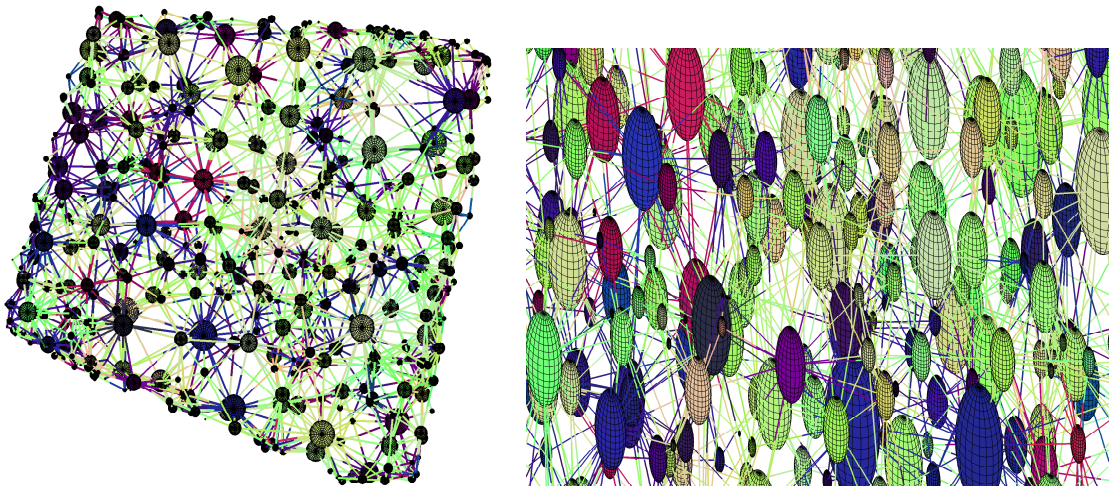

(a) (b)

Figure 3.12: Visual representation of the reduced form GN of the reconstructed 3D microstructure of zirconium in S0. Each sphere represents a single grain with 464 grains/spheres shown; here there radii are represented as 25% of actual size for better visualization. Lines show how grains are connected to other grains; they are dual-colored by the colors of the grains they connect. (a) depicts the vertical (+z) view of the S0 GN. (b) shows a more detailed zoomed-in side view of the same S0 GN.

liminary characterization of general grain statistics have been shown. A multi-scale microstructure search approach has been presented and looking forward will be used more specifically in the next sections.

## 3.8 Grain tracking

Until recently, access to experimentally generated 3D orientation data across multiple states was limited. Advances in electron back-scatter diffraction (EBSD) orientation imaging microscropy (OIM) in 2D has made this technique robust such that it is commonplace in the material science community [48, 49]. Focused ion-beam (FIB) milling systems in conjunction with EBSD-OIM has allowed collection of high spatial resolution ($\sim 50nm$) 3D orientation data at the expense of being a destructive measurement [50]. Dynamical studies of microstructure deformation evolution are performed routinely in 2D, but dynamical studies of 3D microstructure evolution can only really be accomplished through high energy x-ray experiments [51, 52, 53, 54]. Modeling of microstructure evolution through simulation inherently tracks grains and individual elements 1:1. The problem of connecting the same microstructure through deformation states is a form of registration problem.

Complete tracking of a microstructure's character from experimental nf-HEDM data is accomplished through three separate data structures which provide access to local(grain) shape information, local (grain) orientation information, and connectivity grains. These structures are produced through three separate utilities developed in XDM++ to partition the microstructure data into three standard microstructure working domains. Local shape information is provided through the $BoundaryLineInfo$, or $BLI$, for each state. An input stack of microstructure images is read in, grains are defined, and boundary lines between voxels with different grain IDs are returned. The data structure for each boundary segment includes x, y, z for segment end-points, orientations of the triangle on each side of the line segment, misorientation between those orientations, and the grain IDs of the two triangles sharing that segment. This has the form $[\vec{r_i}, \vec{r_f}, q_{G1}, q_{G2}, \Delta q_{G1 \to G2}, ID_{G1}, ID_{G2}]$. See figure 3.13 for visual depiction of the data generated.

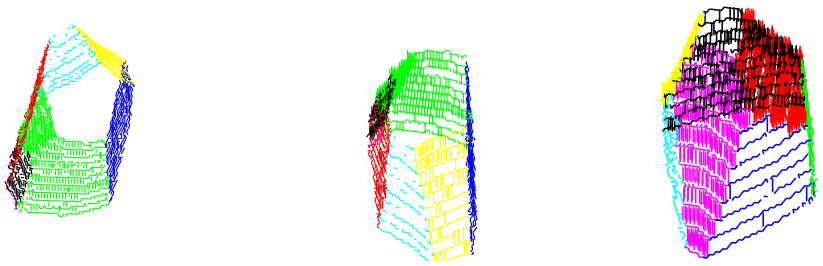

(a) (b) (c)

Figure 3.13: (a) and (b) are two projections of the boundary line information for a single grain and $40\mu m$ height only. Boundary lines are colored by the grain ID of the neighboring grain. Similarly colored patches show that faceted grain boundaries are identified properly. (c) shows a second visual example of a different grain in the S0 dataset.

The three data formats are later integrated together but allowing for adaptability depending on how finely probing of the microstructure is desired. The second format, $CombinedMetrics$ or $CM$, takes in the entire stack of .mic files, defines grains, and calculates standard meaningful metrics from the orientation data. For current studies this includes IGM, KAM, and Schmid factors, as well as grain ID and grain volume information. Since this structure takes the raw orientation data which is already quite large and adds significantly more information to it, memory consumption can be quite large. For example just the S0 state requires $6Gb$. This has the form $[Voxel\ info, GID, Volume, IGM, KAM, m-factor_{1 \to N}]$ where each entry has N slip systems. It is a standard .mic file with added columns for the computed metrics at each point on the voxel grid. Since typically the entire structure is not required, the format can be burst into individual grain files which can be read in whenever needed.

The third format, $GeneralGrainNetworkProperties$ or $GGNP$, is a representa-

tion of the GN introduced earlier. This has the form of [$GID$, $q$, $Volume$, $bEnclosed$, $COM$, $N_{Ngbs}$, $GID_{Ngb1}$, $GID_{Ngb2}$, ..., $GID_{N_{Ngbs}}$]. The format is $\sim 50k\times$ smaller than the $CombinedMetrics$ for the zirconium data presented.

**Algorithm 5** Mapping $CM$ to $GGNP$

```
d̄ = 65μm;// average grain diameter
fVolChangeThresh = 20%;
fMinMis = 180°;
for i = 1; i ≤ NGrains_CM; i++ do nMatchingID = –CM(i).GID;
    for j = 1; j ≤ NGrains_GGNP; j++ do
        if |CM(i).Volume−GGNP(j).Volume| / GGNP(j).Volume ≤ fVolChangeThresh then
            if |CM(i).COM − GGNP(j).COM| ≤ d̄ then
                if Misorientation( CM(i).q, GGNP(j).q ) < fMinMis then
                    fMinMis = Misorientation( CM(i).q, GGNP(j).q );
                    nMatchingID = GGNP(j).GID;
                end if
            end if
        end if
    end for
    CM(i).GID = nMatchingID;
end for
```

Currently these three data structures are generated separately, but they all require segmenting grains from the input microstructure. Since these utilities are not completely integrated, the corresponding grain IDs across the the structures are not exactly the same. Some post-processing is performed to re-map grain IDs in $BoundaryLineInfo$ and $CombinedMetrics$ to the $GeneralGrainNetworkProperties$. Mapping IDs in $CM$ is performed simply by bounding the volume and distance of grains in $GGNP$, and returning the grain in that subset with minimum misorientation to the original grain (should be $\sim 0°$). See algorithm 5 for implementation details.

The mapping of $BLI$ is performed in a similar manner except the main filtering is performed by a convex hull bounding box from the boundary lines instead of via differential volume change and center-of-mass distance. The center-of-mass of the GGNP matched grain must coincide within the convex hull's interior, its volume must be $\leq 120\%$ of the convex hull's volume, as well as having a minimum misorientation with the boundary points' average orientation. In this way, a linked surface data strucutre, volume data structure, and grain network define a single state of experimentally measured microstructure.

The next step is to map them across states so that one can evaluate individual grain and grain neighborhood evolution effectively. Plastic deformation is expected to induce grain rotations, cause grains to change shape, and center-of-mass posi-

tions move, but we assume that this orientation change is gradual, volume change due to plasticity is negligible, and center-of-mass motion is less than the size of average size of grains. This approach takes advantage of the assumption made for an in-situ experiment and should not be generalized to ex-situ measurements without some pre-alignment steps. Mapping the $GGNP$ of S1 $\rightarrow$ S0 is performed in a similar manner to algorithm 5 except that reassignment of IDs does not take place ($MapID\_SNtoS[N-1]$). The mapped ID to S0 is retained rather than overwritten. The other difference is the assumption of minimum misorientation between tracked grains $\simeq$ 0° will not be true. Mapping S2 to S1 is next performed since these states should be more similar than S2 to S0. Mapping S3 to S2 is performed last. Figure 3.14 represents the connections made between functionally different data types and deformation levels of the microstructure data. In this way, a grain in S3 is mapped to S0 indirectly through S2 and S1. For example, to obtain the grain ID in S0 of a grain of interest in S3, one would call something like

$$GID_{S0} \;=\; MapID\_S1toS0(\; MapID\_S1toS0(\; MapID\_S1toS0(\; GID_{S3} \;)\;)\;);$$

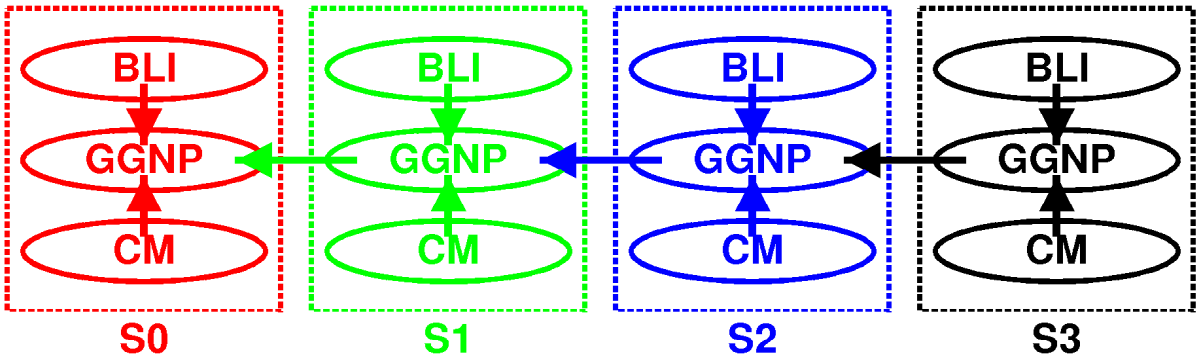


Figure 3.14: Conceptual architecture of the digital microstructure across deformation states. Internal mapping of elements in the three data structures in a single state are enclosed by dashed lines. Mapping between structures is signified by arrows.

Integration of information provided is performed by linking the FFT results to the S0 GGNP by algorithm 5.While the advantage of setting up this connected structure might not be apparent yet, its necessity will become clear in section 3.12. An interesting feature can be located from observation in a map and tracked throughout the entire microstructure through states of deformation. The multi-scale microstructure search approach presented in the section 3.7 has been described in detailed implementation here and its utility will be made apparent in section 3.12.

## 3.9 Texture characterization and evolution

Electron, x-ray, and neutron diffraction pole figures (PF) have been the standard representation of texture in materials. Knowing the experimental scattering geometry is sufficient to determine how a specific crystallographic family of planes are distributed for an entire sample [55]. A pole figure represents the distribution of orientations of a particular set of crystallographic plane normals (the pole). These orientations can be represented by positions on the unit sphere which can then be projected on a chosen plane in a two dimensional figure. Typical pole figures plot the distribution of some high symmetry plane normals in a sample reference based on processing history (ex., a rolling, normal, and transverse direction). Similarly, inverse pole figures are used to show the distribution of some external sample direction (ex., the tesile direction) in the crystal frame.

After inclusion of crystal symmetry, the pole figure can be represented in a unique reduced form. PFs are incomplete orientation information. They represent a projection of orientation space; through a collection of PFs, orientation and strain distributions can be reconstructed by various inversion methods [56, 57, 58]. If one then begins with the full orientation information as obtained from the FMM, PFs can be readily constructed. This is performed here so as to compare with most diffraction deformation experiments which rely on the interpretation of a small collection of orthogonal PFs.

PF representation can easily show initial texture or preferred orientation directions in a sample. Tracking the evolution of PFs points to slip activity through gradual small lattice rotations. They can point to more abrupt orientation changes as in the case of deformation twinning. When a slip system is activated, rotation of the lattice proceeds in a plane define by the primary slip directions. Their evolution can tell how the orientation distribution is changing.

A pole figure can be described as a histogram on a sphere of the orientation distribution of a family of crystal planes in the entire sample weighted by their volume fraction. For uniform grain-sizes and a completely random sampling of orientations, the PF for each family of planes will appear as an even distributions on the sphere if equal-area binning is performed. The general procedure to produce a PF for given {hkil} from complete orientation data is to discretize the sphere, run through all equally-weighted orientations (or grains weighted by volume); for each orientation run through all crystal planes in the family, find the bin in which the plane normal resides and add that weight to the bin (algorithm 6).

In the HCP system the three relevant families that will be investigated are the $\{10\bar{1}0\}$, $\{0001\}$, and $\{10\bar{1}1\}$ in the 4-index notation. These families of planes can equally be represented in the 3-index notation as $\{100\}$, $\{001\}$, and $\{101\}$ by dropping the redundant index, $i$, such that $\{hkil\} \rightarrow \{hk.l\} \rightarrow \{hkl\}$. For 4-index directions, dropping the 3rd index does not generate corresponding directions ([uvtw] $\neq$ [uvw]). $\{10\bar{1}0\}$, $\{0001\}$, and $\{10\bar{1}1\}$ are the slip planes for the prismatic, basal,

**Algorithm 6** PF from $GGNP$

$PF(\phi, \theta) = [\ ]$;// pole figure data
**for** $i = 1; i \leq NGrains_{GGNP}; i++$ **do**
  R = RMatXtalToSample( GGNP(i).q );
  **for** $j = 1; j \leq NPlanes_{hkil}; j++$ **do**
    $\hat{n}_{j,sample} = R \times \hat{n}_{j,xtal}$;
    $[\phi_j, \theta_j]$ = PhiThetaFromR( $\hat{n}_{j,sample}$ );
    $PF(\phi_j, \theta_j) += GGNP(i).Volume$;
  **end for**
**end for**
PlotOnSphere( PF );

and pyramidal<a> slip systems, respectively. Figure 3.15 presents the poles figures for these slip system normals from the volumetric FMM results from S0–S2. Texture changes are apparent between states but are somewhat subtle. The trends are not clear given that multiple spots on the PF can correspond to the same grain. The focus on texture changes here is too broad; we will later investigate the evolution of each point in the PF on a grain-by-grain basis.

A general observation is the {0001} shows clustering of this direction along a direction perpendicular to the tensile axis. In HCP metals this is the basal texture that forms during rolling. The c-axis (or [0001] which is parallel to {0001}) tends to align with the rolling normal direction (ND) [59, 60]. Further knowing that the c-axes are somewhat fixed in one spatial direction, one can interpret the $\{10\bar{1}1\}$ (which is lies in the basal plane) pole figure as grains with different twists about the c-axis. Returning to the 1-D grain-to-grain misorientation distribution in figure 3.11(b), one can explain the peak at 30° by symmetry in the basal plane. These symmetry operators are just $60° \times N$ about [0001], with N = {1,2,...,6}. Grains with a shared c-axis direction cannot be misoriented by more than 30°. Values in the distribution larger than 30° reflect the fact that all c-axes are not completely aligned, and the {0001} pole figure validates that. An untextured, radomly orientated microstructure would have misorientation distribution and pole figures more like those simulated in figure 3.16 [61, 62].

The basal texture in the sample has implications on which deformation modes will be active. If one is to project the tensile axis onto the crystal axes of the somewhat average texture orientation, it would most likely lie in the basal plane, and thus be perpendicular to the c-axis ([0001]). Returning to figure 3.3, most of the grains are oriented such that the tensile axis will lie along the edges in the IPF. Ignoring neighboring effects and assuming single crystal behavior, one expect this sample will deform mostly via prismatic slipping.

Another standard representation of an orientation distribution is obtained by plotting data in the symmetry group restricted fundamental zone (FZ) of orientations in

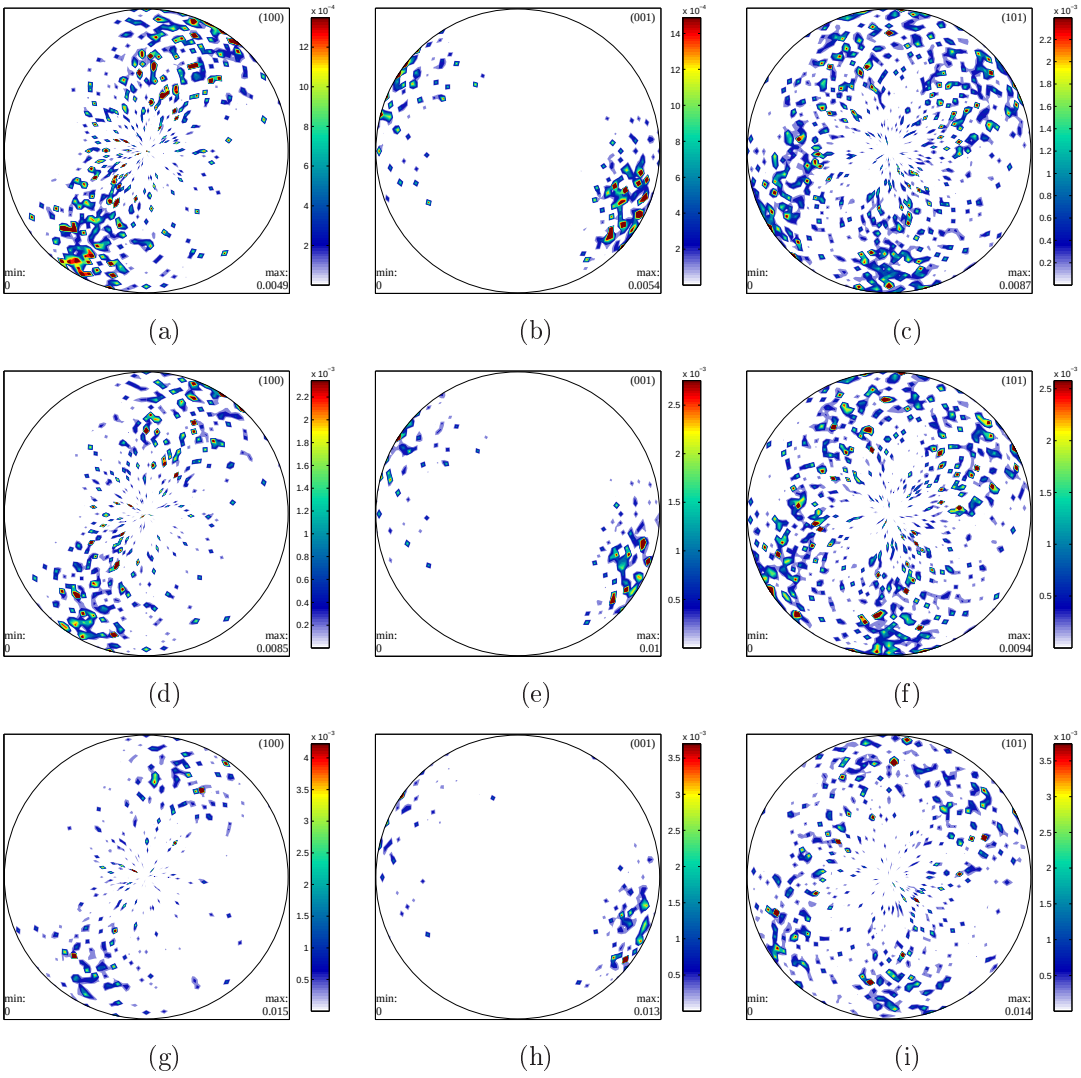


Figure 3.15: Experimental equal-angle pole figures for the slip plane families of the three types of slip in HCP zirconium across multiple deformation states. Note these are generated from grain-averaged orientations showing the average, rather than local, lattice rotations. (a)–(c) correspond to $\{10\bar{1}0\}$, $\{0001\}$, and $\{10\bar{1}1\}$ pole figures, respectively, in S0. (d)–(f) are in the same order for S1. (g)–(i) are in the same order for S2. The direction out of the page is the sample $+z$ direction which corresponds to the tensile direction.

Rodrigues-Frank space. The Rodrigues-Frank vector representation of an orientation is an axis-angle representation such that $\vec{v}_{RF} = \tan(\frac{\theta}{2}) \times \vec{v}_{RotAxis}$. The rotation axis, $\vec{v}_{RotAxis}$, is the common axis between sample frame and crystal frame that the rotation is performed about to go between frames. $\theta$ is the angle by which the rotation must occur. Due to the HCP crystal symmetry, there are 12 symmetrically

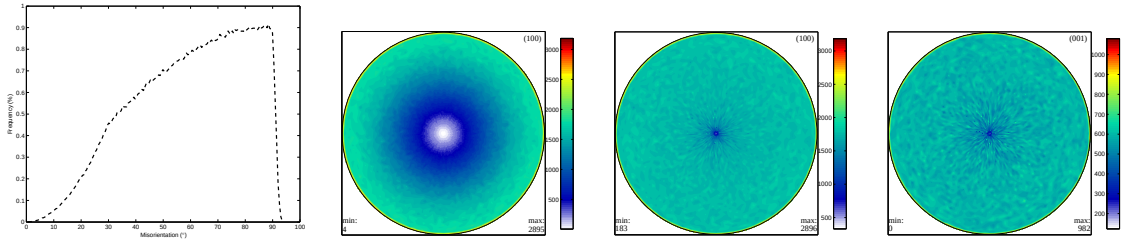

(a) (b) (c) (d)

Figure 3.16: Misorientation distribution and pole figures of a simulated microstructure with random orientations. (a) is the misorientation distribution. (b) is the equal-angle $\{10\bar{1}0\}$ pole figure while (c) represents the same pole figure data with $\frac{1}{\sin(\theta)}$ weighting applied to each bin for normalization by area. (d) is the equal area $\{0001\}$ pole figure normalized in the same way as (c).

equivalent ways to represent an orientation in the entire S0(3). A fundamental zone is the sub-space in S0(3) for HCP crystals where all orientations can be physically distinguished. "The" conventional fundamental zone is taken as the zone where the $\theta$ values are minimum. The resulting 12-fold symmetry is apparent in the figure 3.3 where each standard triangle is equivalent to the others. There exist 24 symmetry operators for cubic crystals which is also apparent in figure 3.2. Only one one standard triangle for cubics and hexagonals is normally shown, for example see figure 3.3(e), just as only one fundamental zone is required. The boundaries of the fundamental zone are formed by the symmetry elements.

Figure 3.17 shows the predicted and experimental orientation distribution evolution. In the figures, the strong basal texture manifests itself by the clustering of grain orientations near the edges of the FZ. The visco-plastic self-consistent (VPSC) simulation is a mean-field approach for modeling multi-slip deformation in polycrystals [63]. The simulation is performed with the texture measured in S0 as input. There is considerable discrepancy between experiment and simulation which is shown by figures 3.18 and 3.19. The underlying level of lattice rotation seems to agree when comparing figures 3.18(a) and 3.18(b); however, figure 3.18(c) shows that the amount of lattice rotation is uncorrelated. Experimentally some grains show a large amount of lattice rotation where the simulation predicts little and vice versa. Figure 3.18(d) shows essentially that the distance between experimentally measured orientations in S2 and those simulated for S2 are further apart than either of those with the original starting orientations.

Several between the elastic FFT and VPSC simulations must be emphasized. The VPSC treats each grain as a single orientation in a homogenous matrix; it returns a grain's plastic response to strain in the form of slip activity and lattice rotation. It does not consider the geometry of the grains or its internal evolution as deformation proceeds. The elastic FFT spatially treats the entire microstructure geometry while

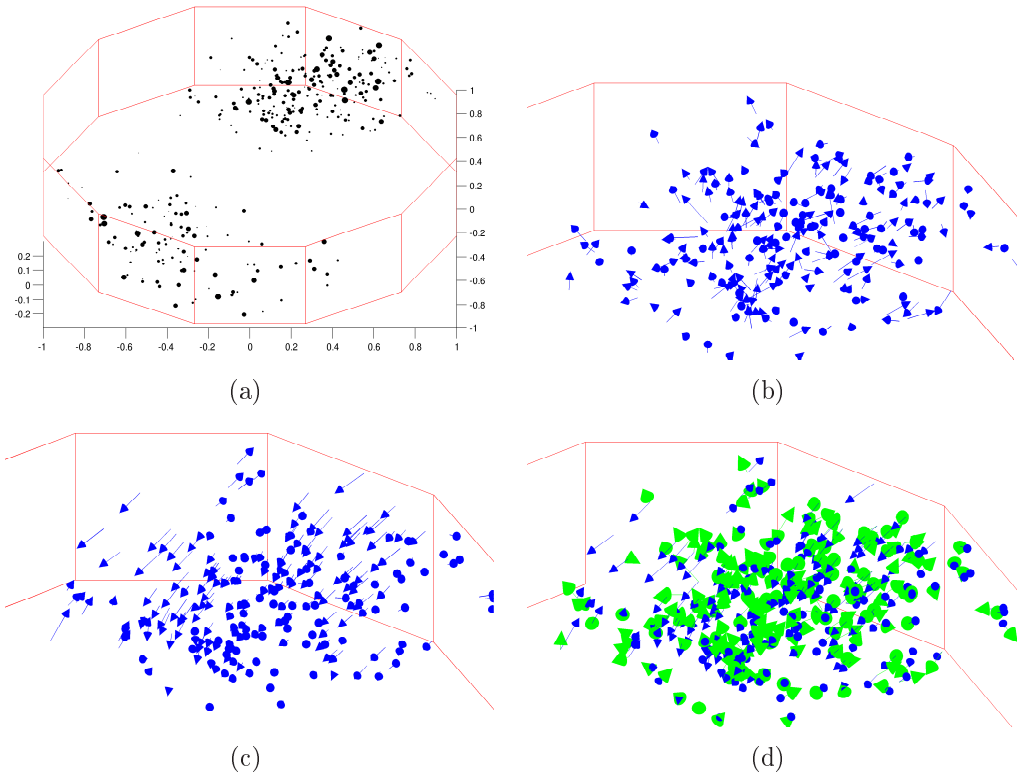


Figure 3.17: Rodrigues-Frank plots of the zirconium orientation distribution in the fundamental zone. (a) is the initial texture in S0. (b) is a zoomed-in region of the top right region of (a) where arrows point from a grain's RF position in S0 to that in S2. (c) is a zoomed-in region of the top right region of (a) where arrows point from a grain's RF position in S0 to where the VPSC simulation predicts them to be in S2. (d) is the data from (b) in (green, experimental) and(c) in (blue, simulated) to show correspondence or difference between experimentally measured grain rotation to predicted rotation.

neglecting activation of plastic activity in grains or updating orientations due to lattice rotations. For the purposes of this study, the returned stresses will be used to compute $\tau_{RSS}$ on relevant slip and twin systems. The integration of the $\tau_{RSS}$ values into the already tracked GN will add another layer of microstructure detail to aid in locating potential twin nucleation and even void formation.

While the magnitude of experimental lattice rotations might not match due to constraints imposed by the neighborhoods in polycrystal, the direction of the lattice rotations do appear to be somewhat correlated. Figure 3.19 compares the direction of lattice rotations for both data sets. Considering the lattice rotations colored in green, which correspond to primary slip on the prismatic system, $\frac{134}{196}$ (68.5%) of these arrows are correlated between experiment and simulation. Considering the lattice rotations

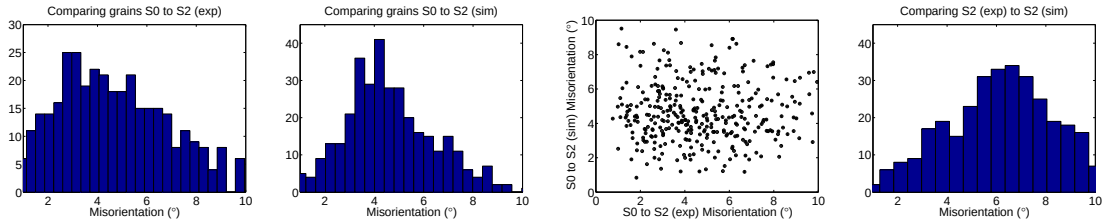


(a) (b) (c) (d)

Figure 3.18: 1D representation of figure 3.17. (a) is a histogram of the number of grains that rotate through a given angle (misorientation angle) in going from S0 to S2. (b) is the corresponding histogram obtained from a VPSC simulation. (c) shows the experimental misorientation of each grain in the dataset (horizontal) versus the simulated misorientation (vertical). (d) is the histogram of misorientations between the experimental S2 and simulated S2.

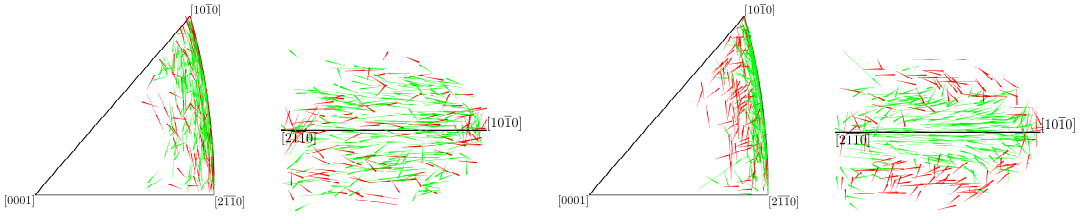


(a) (b) (c) (d)

Figure 3.19: Lattice rotations from S0 to S2 represented in the stereographic triangle. The location of the tensile axis is presented in each crystal's local coordinate system. (a) shows an IPF plot corresponding to experimentally measured lattice rotation of 314 tracked grains viewed from the standard [0001] direction, and (b) shows the same information from the [2$\bar{1}\bar{1}$0] direction. (c) shows IPF plot corresponding to VPSC simulation of the same grains, and (d) shows the same information from the [2$\bar{1}\bar{1}$0] direction. Arrows have been segregated into two colors depending on their direction. Green arrows correspond to lattice rotations toward the [10$\bar{1}$0] while red arrows correspond to lattice rotations toward the [2$\bar{1}\bar{1}$0].

colored in red, $\frac{42}{118}$ (35.6%) are correlated between experiment and simulation. This yields a total of 56.1% correspondence in general lattice rotation direction between simulation and experiment.

Returning to figure 3.3, the initial texture and loading conditions for this sample make prismatic slipping the most likely active slip system along with the fact that $\tau_{CRSS,prismatic} \leq \{\tau_{CRSS,basal},\ \tau_{CRSS,pyramidal<a>}\}$. From the direction of lattice rotations, the simulation (experiment) results suggest 62.4% (66.7%) of grains do indeed primarily deform by prismatic slip. Below, direct investigation into slip activity will be performed on a grain-by-grain basis.

In this section, several different standard representations of polycrystal texture

were presented for the measured tensile deformed zirconium sample. It was found to have an initial basal texture, and combined with the tensile direction, prismatic slip is expected to be the primary slip system. The evolution of the texture was presented in several visual formats, and comparisons made with VPSC simulation with less than satisfactory correspondence. The local texture evolution of specific grains will be taken up later in the chapter.

## 3.10 Using absorption tomography as a strain gauge

Reconstruction of the ten tomographic volumes measured was performed by standard inverse Radon transform. [64]. Each experimental tomographic scan consists of collection of 901 images similar to figure 3.20(a) collected at a succession of rotation positions ($\omega$) spanning 180°. Figure 3.20(a) demonstrates the physical profile of the tensile sample through this single projection. The vertical limit of the beam (650 pixels, $\sim 1mm$) is the limiting scan volume size per collection. The same high resolution imaging detector (with $1.5\mu m$ pixels) used for HEDM is used here. Due to the limited height of the x-ray beam, the profile of the sample is truncated below pixel row 1250 and above 1900. Each of horizontal rows of pixels (containing an absorption profile of a quasi-planar section through the sample), is collected into a sinogram like through a scan are collected into a single sinogram like the one shown in figure 3.20(b). This represents 900 $\times$ 650 single absorption measurements through the sample for each of the ten tensile strains. The inverse Radon transform converts the collection of absorption profiles into a spatially resolved (electron) density map.

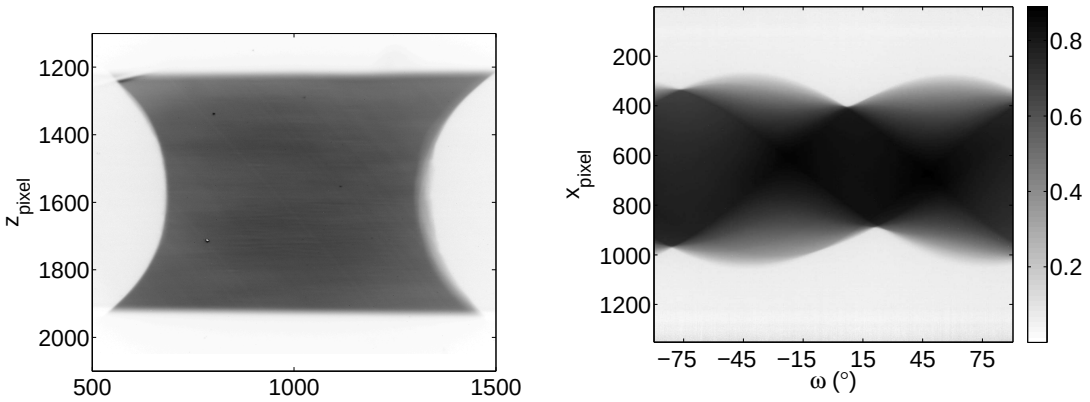


(a) (b)

Figure 3.20: (a) is a single absorption image taken in a tomography data collection for a single state. (b) is a sinogram of a single pixel row in a single state through 180° of rotation.

The curved profile of the tensile sample, observed figure 3.20(a), is used to follow the shape change through tensile deformation. Each tomographic reconstruction for a

single cross-section (single pixel row) is binarized to retain only pixels corresponding to absorption coefficients matching material (zirconium). The number of pixels corresponding to material per cross-section is summed, and an effective cross-sectional area is found for each tomographic reconstruction. Figure 3.21(a) presents the reconstructed tomographic area of the sample, colored by strain state, as a function of vertical position on the sections.

For each strain state, a least-squares fit is performed to the model parabolas in equation 3.2 :

$$s(z_{pixel}) \;=\; \sqrt{Area(z_{pixel})} \;=\; s_0 \;+\; \frac{\mu^2}{4p} \times (z - z_0)^2 \tag{3.2}$$

$s_0$ corresponds to the square root of the minimum cross-sectional area for the strain state (effective side width), $\mu$ is the pixel size which gives physical scale to the images ($\mu = 1.48\mu m$), $p$ corresponds to the distance to the focus of the parabola, and $z_0$ corresponds to the pixel row with minimum cross-sectional area reconstructed. The position $z_0$ will be referred to as the center of sample or center of the neck.

The numerical results of these parabolic fits can be found in table 3.2, and their correspondence with the actual shape compare in figure 3.21(a). The table shows that the minumum cross-sectional area decreases as a function of strain. The $z_0$ values are used as the reference point. $z_0$ is assumed to correspond to the same physical material through states. $z_0$ also is used for the registering of nf-HEDM layers presented in 3.1. The general shape evolution of the sample is depicted in figure 3.21(b).

| State | $s_0$ $\mu m$ | p $\mu m$ | $z_0$ $pixel$ |
|---|---|---|---|
| S0 | 882.6 | 150.5 | 1638.9 |
| S1 | 882.5 | 150.9 | 1603.8 |
| S2 | 824.6 | 149.1 | 1587.6 |
| S3 | 810.4 | 149.3 | 1586.3 |
| S4 | 804.0 | 150.5 | 1647.7 |
| S5 | 794.4 | 152.0 | 1587.3 |
| S6 | 784.5 | 153.9 | 1588.4 |
| S7 | 754.7 | 162.9 | 1590.7 |
| S8 | 676.0 | 201.0 | 1595.2 |
| S9 | 544.0 | 137.0 | 1578.0 |

Table 3.2: Least-square fit parameters for the sample profile fit to a model parabola across strain states.

The cross-sectional area information is then used to estimate the amount of plastic strain present in the sample at each of the measurement states. The true strain, $\epsilon_T$, can then be calculated as

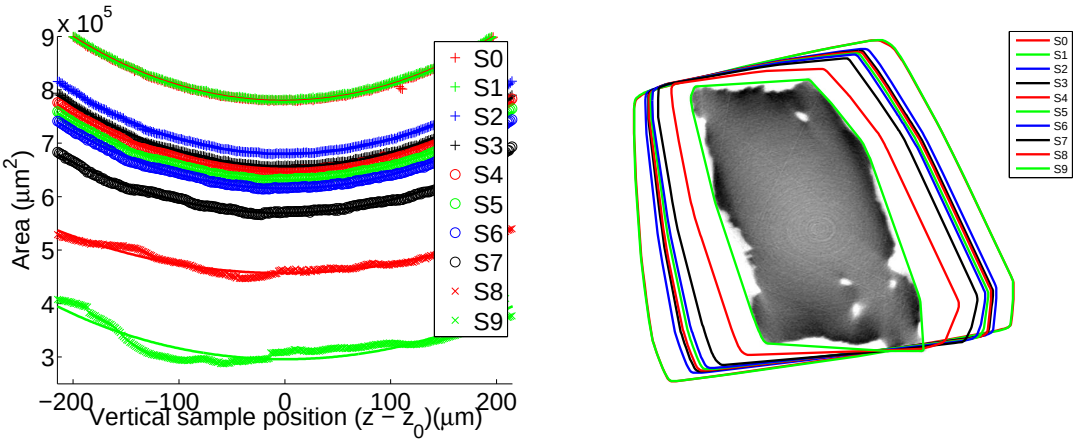


(a) (b)

Figure 3.21: Shape change of the zirconium sample as a function of strain state. (a) is a plot of the cross-sectional area for ± 150 *pixel rows* (± 220 $\mu m$) about the center of the sample through all 10 strain states. Solid lines represent fits to the parabolic function to describe the sample shape. (b) shows the density plot (grayscale) of a single tomographic reconstruction in S9 with voids present. Colored lines represent the narrowing sample shape for that cross-section as tension is applied.

$$\epsilon_T = \int d\epsilon = \int_{l_0}^{l_f} \frac{dl}{l} \tag{3.3}$$

where $l$ is the material length along the tensile axis; and with the substitution, $l = \frac{V}{A}$, $dl = -\frac{V}{A^2}dA$

$$\epsilon_T = \int_{A_0}^{A_f} \frac{(-\frac{V}{A^2}dA)}{\frac{V}{A}} = -\int_{A_0}^{A_f} \frac{dA}{A} = \int_{A_f}^{A_0} \frac{dA}{A} = \ln(A)|_{A_f}^{A_0} = \ln(\frac{A_0}{A_f}) \tag{3.4}$$

Combined with $s_0$ values in table 3.2 the largest values of $\epsilon_T$ are computing in table 3.3 by $\epsilon_{T,S_i} = \ln(\frac{A_{min,S_0}}{A_{min,S_i}}) = \ln(\frac{(s_{min,S_0})^2}{(s_{min,S_i})^2}) = 2\ln(\frac{s_{min,S_0}}{s_{min,S_i}})$.

| S0 | S1 | S2 | S3 | S4 | S5 | S6 | S7 | S8 | S9 |
|---|---|---|---|---|---|---|---|---|---|
| 0 | 0.0 | 13.6 | 17.1 | 18.7 | 21.1 | 23.6 | 31.3 | 53.3 | 96.8 |

Table 3.3: True strain via x-ray tomography.

At this point, the measurement, reconstruction, and characterization of the tensile sample has been performed. The digital microstructure has been registered and linked across states by tomographic shape, grain orientation, and grain position. Simulations have been performed to estimate the elastic and plastic response of the measured microstructure to tensile deformation. The following sections present observed results

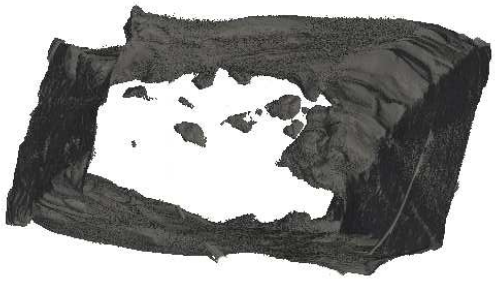

Figure 3.22: 3D rendering looking down the wire axis of the zirconium sample. The sample contour from S9 is presented as produced via X-ray tomography. Internal voids can be seen inside the main contour.

of the physical phenoma of slip activation, twinning, and void formation in the deformed microstructure. The purpose of such detailed characterization and mapping will become apparent.

## 3.11 Quantifying damage through slip activation

### 3.11.1 Introduction

The on-set of plastic deformation at this point has been shown through shape changes as seen by x-ray tomography. One of the main mechanisms for plastic deformation is crystal slip, or dislocation glide. The overall grain rotation during plastic deformation is produced by the gradual accumulation of lattice rotations produced by slipping on preferential planes ($\vec{n}$) and direction ($\vec{b}$) (slip systems). Active slip planes tend to be those crystal planes with the closest packing. This corresponds to shorter lattice displacement vectors (Burgers vector) which are less energetically costly induce. For FCC metals, there are 12 independent slip systems that occur on the $(111)[1\bar{1}0]$. Three classes of slip in the HCP case were introduced in figure 3.3(e), the prismatic systems (3), the basal systems (6), and the pyramidal<a> systems (3). There exist other classes of slip in the HCP system, but for the purpose of this study they are not relevant. There are infinitely many slip systems also available for FCC metals as well, but their appearance is suppressed due to longer Burgers vector which imples a larger energy barrier. In the previous section, comparisons were made between the grain average lattice rotations and a mean-field plasticity simulation. Here the spatially resolved local lattice reorientation will be investigated in the context of demonstrating slip system activation. This will be compared with single crystal expectations and insight into the unique macroscopic shape change that occurred in our sample.

Figure 3.23 shows that the three classes of slips for HCP zirconium all share a common $<11\bar{2}0>$ slip direction. The direction of their slip plane normals, however, are quite different. The basal systems have plane normals that point parallel to

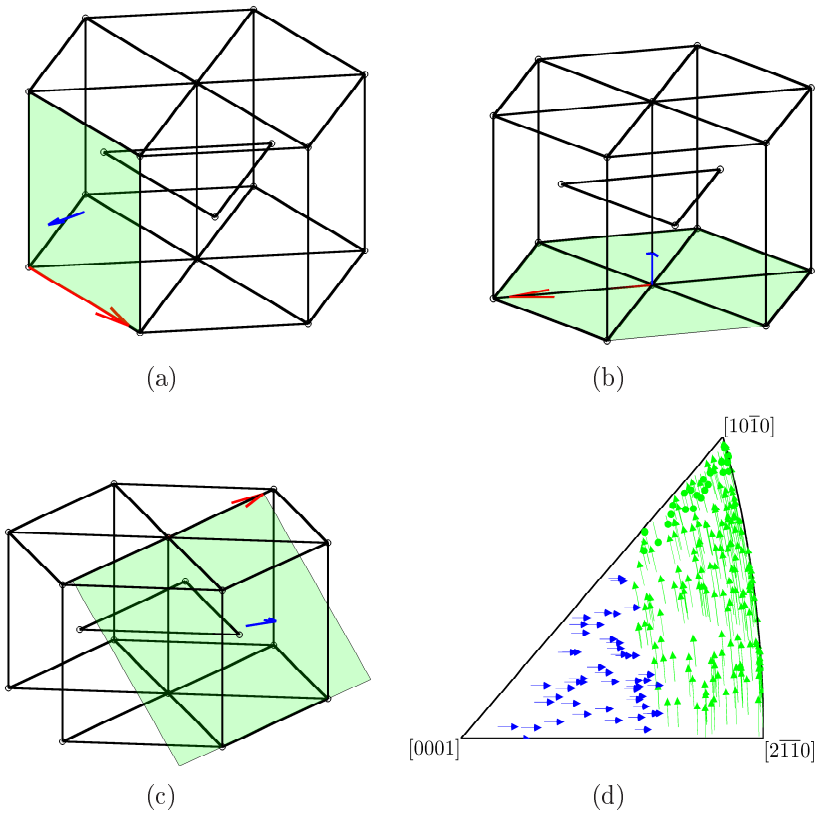


Figure 3.23: Geometric depiction of the different classes of slip systems in the HCP zirconium lattice. (a) depicts a single prismatic system, (b) a basal system, and (c) a pyramidal<a> system. Green represents the slip plane, blue the slip plane normal, and red arrows the slip direction. (d) shows an IPF of a random selection of orientations with simulated grain rotations for single slipping. Arrows point in the direction of rotation. Green corresponds to orientations proceeding with prismatic slipping, blue with basal, and red (not present) to pyramidal <a>.

[0001], the prismatic systems have planes that are perpendicular to the basals and their normals lie in the basal plane. We see in figure 3.23(d) that pyramidal<a> slipping will be suppressed which is consistent with figure 3.3(e) shown in section 3.3. Pyramidal<a> will be ignored from here as it is not expected be observed. Depending on the active slip system, the nature of the local grain lattice rotation is considerably different. This is a direct consequence of local crystal rotation axis (CRA) being parallel to $\hat{b} \times \hat{n}$. The CRA for each class of slip is distinct owing to their shared basal slip vector but different plane orientations. This fact will allow local lattice rotations to be associated with single slip system.

### 3.11.2 Slip Activity

The texture present in our sample implies that most grains are preferentially oriented for only prismatic slipping. Other forms of slipping can expected as a consequence of non-uniform stress in individual grains and geometric shape compatibility constraints. One then expects the dominant signature of lattice rotation to be associated with prismatic slip.

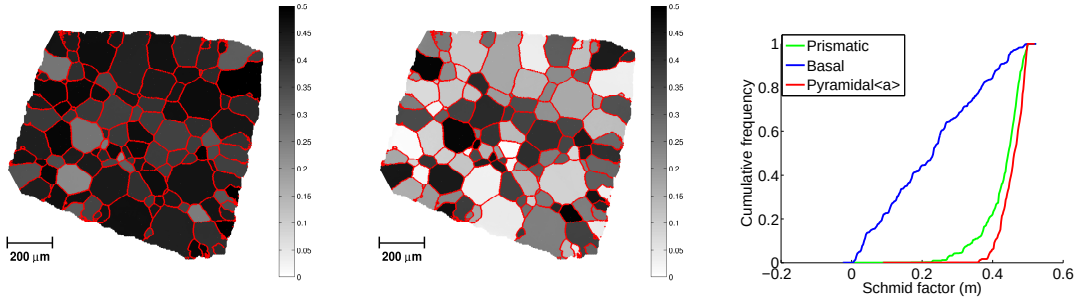


(a) (b) (c)

Figure 3.24: Schmid factor maps for the (a) prismatic systems and the (b) basal systems. Scales are between 0 and 0.5. Red lines are drawns to indicate grain boundaries. (c) shows the cumulative distribution of Schmid factors in S0. In each casem the highest Schmid factor among the variants is plotted.

Initially the Schmid factor calculation for each orientation in the volume provides an indicator of the fact that prismatic slip is expected. Figure 3.24 shows that for a single reconstructed map, the majority of the grains have high Schmid factor prismatic slip, and only a few are well oriented for basal slip. Figure 3.24(c) indicates that the dominant slipping is expected to be via prismatic slip. Figure 3.19 shows with the green arrows the expected grain rotation axis consistent with prismatic slipping in tension. More than half of the rotations point to prismatic slip as the mechanism for those grain rotations. A large population of grains do follow the expected deformation from single crystal predictors. Later we will look at slip activation on the individual grain level.

Another indication that the primary slip system activated in this sample comes directly from the observation of shape change in the tomographic data. It was shown in figure 3.15 that the basal texture of this sample meant that the basal plane normals mostly point in the $^{-}x$ direction of the sample frame and prismatic plane normals point within the basal plane. When elongation proceeds in single crystals on a given slip system, compression of the crystal will proceed in a direction parallel to the slip plane normal [35]. This is the crystallographic description of the Poisson ratio. The tomographic data shows that the sample shape change occurred mainly by compression along the sample $^{+}y$ direction. Minimal compression occurred parallel to the {0001} direction indicating minimal basal slip activation. The tomographic

data showing uni-directional compression of the sample along with initial texture measurement is evidence for strong activation of prismatic slipping.

To investigate direct evidence of local grain rotation, a modified approach to the kernel-average misorientation (KAM) is taken. Typically KAM is calculated as the average misorientation angle from a given point with its kernel (usually $1^{st}$ or $2^{nd}$ nearest neighbors). The average angle is the only information retained ($KAM_{\phi}$). In this modified KAM form, a local CRA for each kernel element is extracted ($KAM_{\vec{v}}$). If their angles are all of similar magnitude, the average CRA is returned. If one element is much larger than the rest, the CRA for the large misorientation element is returned. In this way, the KAM angle is returned as well as added information about the local CRA.

Using the CRA approach on S2, each $KAM_{\vec{v}}$ is assigned to a particular slip system depending on how closely it aligns with the expected axis. KAM values less than 0.25° are removed from the analysis. Axes within a cone of 10° are collected for the prismatic, basal, and pyramidal<a> slips. 64.4% of the KAM axes are associated with prismatic slip, 1.1% with basal slip, and 2.5% with pyramidal<a>. When a cone of 15° is used, the numbers are 82.2%, 9.0%, and 2.4%, respectively. When the KAM threshold value is reduced from 0.25° $\rightarrow$ 0.1° approaching the resolution limit of nf-HEDM, the population of slip activity increases slightly for basal and pyramidal<a> and decreases slightly for prismatic slip. This can be attributed to either random scattering of axes for orientation differences near the orientation resolution or perhaps the less likely slip systems are bound to generate smaller magnitude lattice rotations. Either way, the predicted activation of predominantly prismatic slip is confirmed by using the CRA returned from the modified KAM analysis. Further, local lattice rotations due to prismatic slip tend to be of larger overall magnitude.

Finally we present evidence for prismatic slip in grains by way of analyzing slip bands in the reconstructed microstructure. We recognize in the confidence maps that there are clear bands of low confidence that run along the [0001] direction within grains which correspond to mostly the $^{+}x$ direction in the sample space (see figure 3.9(f)). Given the observation about the uni-directional compression as seen through tomography, it is hypothesized that these are the appearance of prismatic slip bands. In figure 3.25, one example grain with this feature is plotted. This specific grain's initial Schmid factor for prismatic slip is $m_{Prismatic} = 0.489$. The large jumps in the misorientation correspond to positions where the angle between the CRA and [0001] are close to 0° indicating local lattice rotation consistent with prismatic slip. Further, the physical direction of these bands match with the prismatic slip plane traces. These features are consistent with prismatic slip bands.

One last example is shown of the gradual lattice rotation for a grain with high prismatic Schmid factor ($m_{Prismatic} = 0.437$). The point-by-point spread of the grain is shown via an IPF in figure 3.26. The grain average motion is represented by connecting the red and black points. Internally there are some elements of the grain which exhibit a much larger rotation from the the initial orientation. This example

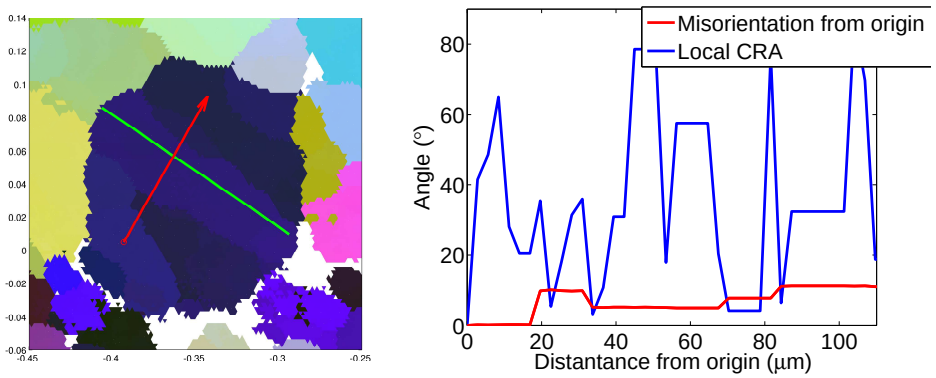


(a) (b)

Figure 3.25: (a) presents a single grain oriented for prismatic slip showing slip bands. The green line indicates the trace of the prismatic slip plane onto the ~~sample~~ plane. The red arrow represents the path in which misorientation (from the tail of the red arrow in 3.25(a)) is plotted. (b) represents the misorientation fin red beginning at the origin of the red arrow in (b). The blue line represents the angle between the local CRA and the [0001] direction.

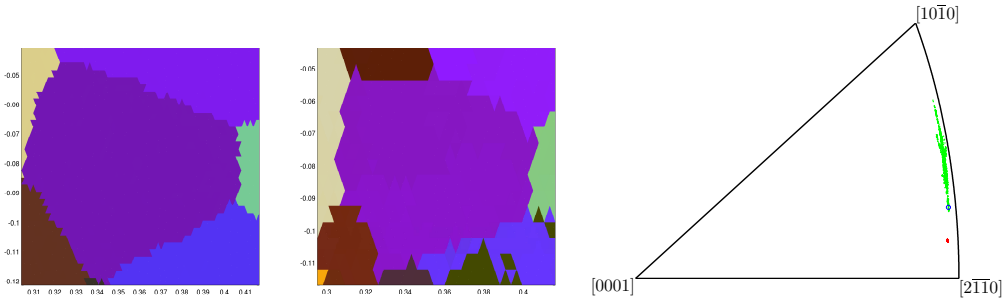


(a) (b) (c)

Figure 3.26: IPF showing grain rotation and the spread of a single grain's orientation. (a) and (b) represent Rodrigues-colored orientation maps for corresponding layers of the same grain in S0 and S2, respectively. (c) represents the initial spread of the grain S0 in red and its later rotation and spread in green in S2. The black 'o' marks the grain orientation's average orientation in S2.

illustrates the point-by-point slip that is tracked in the reconstruction, and its lattice rotation is consistent with the expected slip system.

### 3.11.3 KAM and GAM

The concept of KAM and GAM were originally introduced in chapter 2. The amount of dislocation density has been directly linked to local orientation variations such as

KAM [65]. By deformation state S2, sufficient tensile force has been generated in the crystal structure to generate dislocations. These dislocations move along the slip planes already discussed. Pile-up of dislocations results in considerable distortion of the lattice.

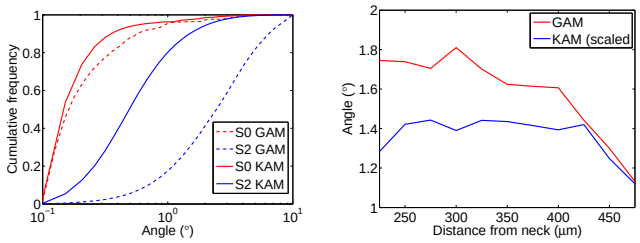


(a) (b)

Figure 3.27: (a) shows a semi-log plot of the cumulative distributions of KAM and GAM in S0 and S2. (b) shows the Poisson distribution $\lambda$ values of KAM and GAM as a function of position away from the sample center. KAM values are scaled for better visualization.

The local lattice distortion is seen through the increase in both KAM and GAM values. Figure 3.27 shows the cumulative distribution for these metrics before and after severe plastic deformation. A fit to a Possion distributions yields a $\lambda = 0.33°$ for the S0 GAM distribution, $\lambda = 0.25°$ for S0 KAM, $\lambda = 3.05°$ for S2 GAM, and $\lambda = 0.73°$ for S2 KAM. Looking at the final 11 layers measured in S3 away from the neck, a decrease in both KAM and GAM is observed as the distance from the neck increases. For each layer, $\lambda$ is tracked as a function of moving away from the center of the sample. As expected, KAM and GAM increase with plastic deformation and deformation content is localized to the gauge section.

### 3.11.4 Remarks

It was shown in this section that a considerable amount of deformation occurred in the zirconium sample by S2. The shape change observed was linked to the initial texture of the sample. Deformation by the most likely slip systems available (prismatic) is consistent with the contraction seen perpendicular to the tensile axis. A single example of slip bands in the microstructure was presented as well as a single example of grain rotation and spread matching the expected single crystal behavior.

While that examples show cases where the grain behaves as expected from the external load direction, one issue still unresolved is the mismatch in grain rotations about the [0001] by comparison with simulation shown in section 3.9. One possible explanation for this is that some of the grains may experience tensile forces when the geometrical constraint by the microstructure would have produced compressive stresses locally. The different stress state would then lead to completely different

states of either tension or compression which would manifest in reversed lattice rotations. This would account for the mismatch in the direction of rotation of some grains. The simulation used ignored grain-to-grain boundary constraints.

While slipping is a major component of the deformation observed in this uniaxial tensile experiment, the next section will discuss another deformation mode for zirconium, tensile twinning.

## 3.12 Twin Nucleation and Growth

One alternative deformation mechanism to slip that is available in low symmetry materials is deformation twinning. Until recently the observation of tensile twin nucleation was limited to 2D surface measurements. In this section, results from this zirconium tensile experiment are presented with focus on observed twinning in the bulk and how that compares with the standard view on twin nucleation.

Twinning is a plastic deformation mechanism that produces a fixed amount of lattice shear in a given volume. It occurs frequently in materials with crystal symmetry less than cubic and in hexagonal metals such as Zr in particular. Twinning occurs during plastic deformation because of a lack of slip systems (dislocation glide) that operate at sufficiently low resolved stresses. Twinned volumes generally appear as thin plates whose surfaces correspond to the twinning plane; this morphology minimizes the accommodation required in the surrounding material. Twinning is distinct from slip in that it produces a discrete jump in orientation, as opposed to the gradual lattice rotation associated with slip. Thus distinctive signatures of mechanical twinning are that new orientations appear in a material and subdivision of grains occurs. These responses enhance work hardening and are therefore an important component of the plastic response.

Twins have a specific orientation relationship with the parent crystal (or grain), which is determined by the twin plane, twinning direction, and magnitude of the shear [66]. In the tensile test performed here, the relevant twin plane is the $\{10\bar{1}2\}$ with shear displacement in the $<\bar{1}011>$ direction. This is called a tensile twin because its operation results in extension of the grain along the c-axis (of the parent grain) and compression in the transverse plane, thus accommodating the imposed macroscopic strain. The geometry of the twin is such that the orientation relationship is equivalent to a rotation of $2\tan^{-1}\left(\frac{1}{\sqrt{3}}\frac{c}{a}\right)$, or, in Zr, $\sim 85.2^\circ$ about $<10\bar{1}0>$ with a shear strain of 0.167. This corresponds to a $\Sigma 11b$ coincident site lattice relationship; as in all such relationships it is useful to keep in mind that crystal symmetry provides for a large number (viz. 288) of crystallographically equivalent descriptions, including $180^\circ$ about the twinning direction [67, 68]. Figure 3.28 shows 1 of the 6 twin variants and how a twin transformation will drastically rotate the entire unit cell after reflection about the twin plane. In figure 3.28(b) the c-axis is drawn to see the large ($\sim 85.2^\circ$) difference between parent and twin crystals.

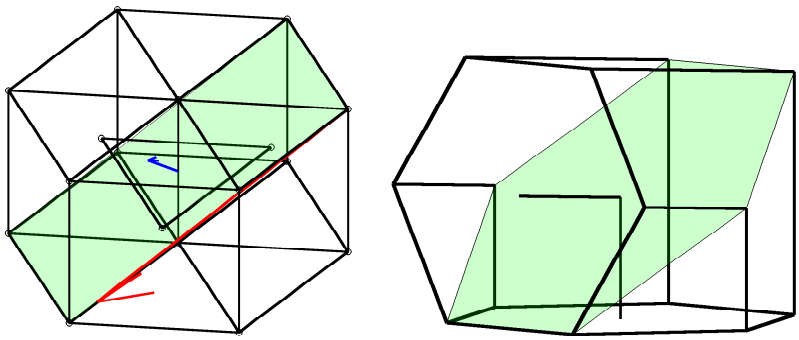

(a) (b)

Figure 3.28: Diagram showing the $\{10\bar{1}2\}<\bar{1}011>$ tensile twin system. (a) represents the HCP unit cell with green representing the twin plane, blue arrow the twin plane normal, and red arrow the twin shear direction. (b) represents the parent and twin orientation as reflected about the green twin plane.

Tensile twins were observed to appear by S2 where none had existed previously.

### 3.12.1 FMM detection

Utilizing the data structure described in 3.8, a brute force search through boundary lines is performed. Any elements' with misorientation satisfying the twin misorientation relation ($85.2^\circ$ $<10\bar{1}0>$) within an accepted tolerance of $2.5^\circ$ in both axis and angle is classified as a twin boundary. The boundary element grain pairs are recorded along with the grain in the graph with which they are associated in the initial S0 state (if they could be mapped back). Newly formed twins cannot be traced back to an original grain since no twins existed initially, but the original parent is successfully tracked back. These grains are then tagged as parent grains which eventually twin. The selected twin variant of the found twin can then be identified easily by the shared common $\{10\bar{1}2\}$ twin plane of the two boundary elements. With this identification and mapping in place, Table 3.4 is easily generated. Figure 3.9 demonstrates the identification of a single twinning event across strain states. The initial texture implies that most grains are unfavorably oriented for twin activation so we expected at most a select few events. This can be best illustrated through figures 3.19(a) and 3.3(d). None of the twinning grains initially have their c-axes aligned with the tensile axis which results in small $\tau_{RSS}$ on the twinning system. Through the boundary search method, 14 unique grain ID pairs are found in the S2 BLF structure. Their association with other states, within the grain network, and the simulated elastic FFT stresses is accomplished through the mapping shown in figure 3.8. Characterization

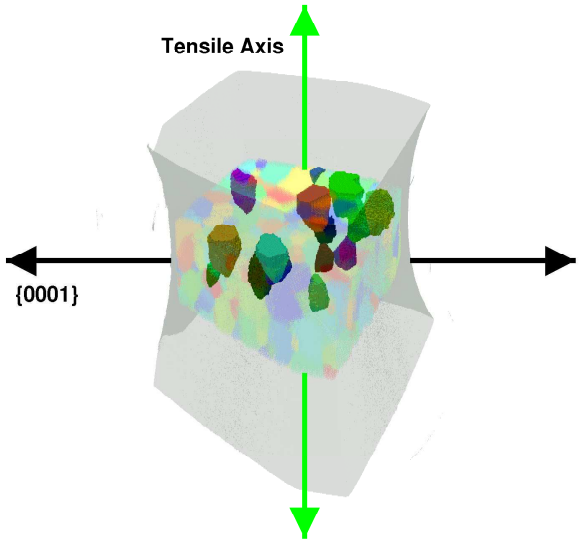


Figure 3.29: Overhead view of a 3D representation of the probed Zr microstructure. The semi-transparent envelope represents a $600\mu m$ tall contour as produced via x-ray tomography showing the initial tensile sample shape. Semi-transparent colored grains represent the full extent (200 $\mu m$ tall) of orientation mapping in the central region. Solid colored grains represent the true shape and location of parent grains in the initial state (see Table 3.4). Texture and tensile axes are added to illustrate the loading conditions.

of the twin population can then proceed.

Table 3.4 characterizes fourteen parent grains that twin by state S2. A large range of parent grain sizes and consequently numbers of nearest neighbors is represented in the twinning population but the distribution of twinning grains is correlated with larger sizes compared to the overall distribution. In two cases, grains 11 and 12, two variants form within the same parent; no secondary twins [69, 70] are observed. As demonstrated by the example shown in Fig. 3.30, extended interface planes between parents and twins tend to follow the common $\{10\bar{1}2\}$ plane containing the relevant $<\bar{1}011>$ shear direction, thus forming coherent interfaces [59]. Some twins have large, $\sim 50\mu m$, thicknesses across an entire parent while others are close to the spatial resolution limit of the measurement. All share a boundary with at least one of the parent's neighbors; none are completely enclosed by the parent grain. By state $S3$ some twins occupy more than 50% of the volume of the original parent.

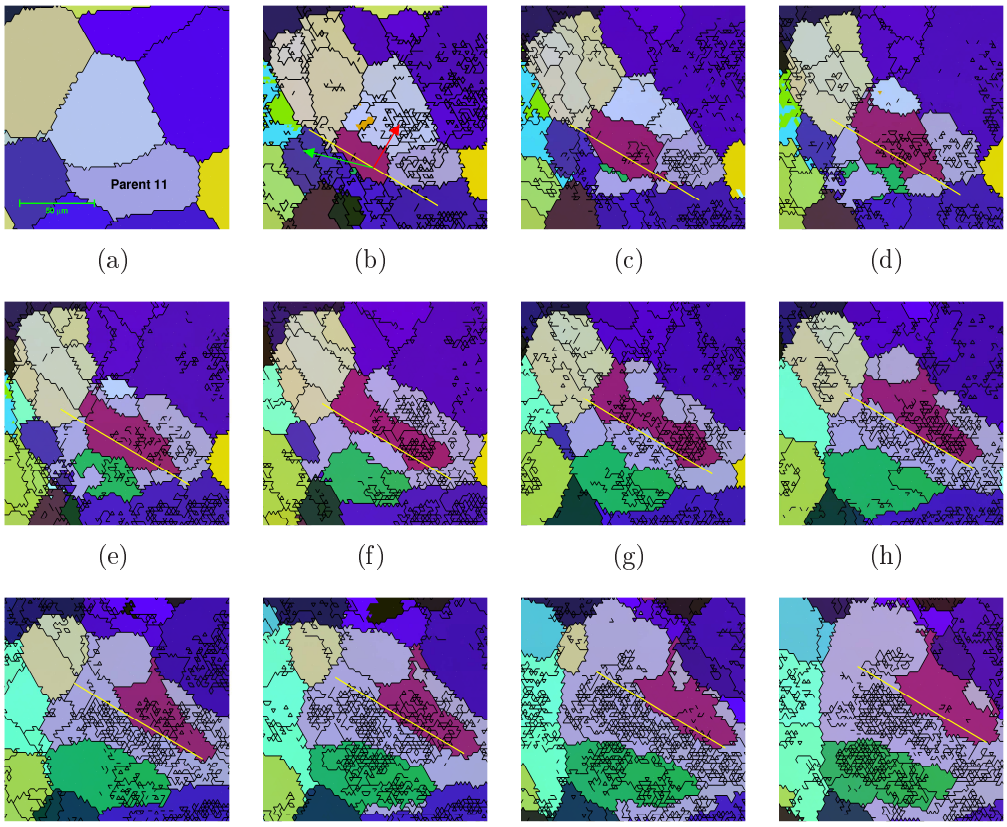


Figure 3.30: Three dimensionally resolved twinning in parent 11 of Table 3.4 shown through a series of orientation maps containing $\approx 15000$ elements of a small sub-space of the measured microstructure. Black lines are drawn between elements having $\geq 1^{\circ}$ misorientation. (a) Unstrained orientation map with below resolution intragranular orientation variation positioned 10 $\mu m$ below the tip of the grain which will twin in later states. (b) - (l) Successive layers, spaced 4 $\mu m$ apart, in strain state S2 (13% tensile strain). The layer in (b) corresponds closely to that in (a). Note the appearance of low angle boundaries indicating the break-up of the grain structure. The maroon and green regions are two different active twin variants associated with grain 11. In (b) the red arrow represents the common $\{10\bar{1}2\}$ twin plane normal, the green arrow the common $<\bar{1}011>$ twin shear direction. These unit arrows have been projected into the image plane. The yellow lines in (b) - (l) are the twin plane trace for the maroon variant displaced in each image according to its tilt relative to the image plane. The yellow line follows the same physical plane through successive maps. Note also the pronounced correlation between the maroon twin and the rotated region of the grain to the upper left in (c) through (h).

Table 3.4: Information for 14 consistently tracked grains showing tensile twinning at 13% strain. "Consistently tracked" is defined as keeping the change in volume $\leq 20\%$, change in average orientation $\leq 10°$, and position $\leq 50\mu$m between state S0 and state S2. Grain size is given as sphere-equivalent radii ($\mu$m). $N_{GB}$ is the number of grains that share a boundary with the parent grain in state S0. Average orientation is given as Euler angles of the parent grain in state S0 relative to the sample reference frame with tensile axis along the $z$-coordinate. Maximum Schmid factors, $m_{max}$, for the grains are given as well as that for the twin system which was activated, $m_{act}$, as quoted from S0 because these ranks change as the microstructure is deformed. Similar numbers are given for RSS from a fast Fourier transform (FFT) based elastic simulation. The rank (by Schmid factor) of the activated twin variant is also given.

| Parent ID | Grain Size ($\mu m$) | $N_{gb}$ | Enclosed bool | Orientation (°) | | | $m_{max}$ | $m_{act}$ | $RSS_{max}$ (MPa) | $RSS_{sel}$ (MPa) | Rank |
|---|---|---|---|---|---|---|---|---|---|---|---|
| 1 | 49.0 | 11 | 0 | 73.5 | 54.0 | 290.7 | 0.145 | 0.066 | 142.54 | 45.38 | 3 |
| 3 | 44.2 | 15 | 1 | 226.6 | 56.0 | 123.8 | 0.106 | 0.072 | 89.09 | 60.88 | 2 |
| 4 | 63.5 | 22 | 0 | 66.2 | 50.1 | 295.2 | 0.170 | 0.170 | 186.27 | 186.27 | 1 |
| 6 | 33.9 | 10 | 1 | 229.0 | 69.4 | 113.9 | 0.001 | -0.073 | 10.67 | -70.63 | 3 |
| 7 | 70.3 | 16 | 1 | 65.2 | 58.6 | 270.4 | 0.136 | 0.136 | 140.54 | 140.54 | 1 |
| 8 | 57.5 | 18 | 1 | 230.7 | 63.6 | 112.1 | 0.054 | -0.032 | 45.29 | -41.40 | 3 |
| 9 | 52.3 | 14 | 0 | 60.7 | 71.0 | 323.3 | 0.050 | 0.043 | 41.37 | 35.95 | 2 |
| 10 | 71.8 | 17 | 0 | 67.3 | 81.0 | 303.2 | -0.081 | -0.126 | -77.64 | -125.92 | 3 |
| 11 | 68.8 | 19 | 0 | 213.0 | 44.4 | 124.3 | 0.227 | 0.200 | 178.04 | 139.61 | 2 |
| 11 | 68.8 | 19 | 0 | 213.0 | 44.4 | 124.3 | 0.227 | 0.190 | 178.04 | 146.92 | 3 |
| 12 | 45.7 | 13 | 1 | 204.1 | 47.8 | 145.5 | 0.227 | 0.074 | 178.45 | 44.44 | 3 |
| 12 | 45.7 | 13 | 1 | 204.1 | 47.8 | 145.5 | 0.227 | 0.227 | 178.45 | 178.45 | 1 |
| 13 | 59.4 | 14 | 1 | 79.0 | 50.0 | 273.6 | 0.207 | 0.202 | 207.69 | 203.25 | 2 |
| 14 | 24.9 | 2 | 0 | 225.0 | 87.7 | 120.5 | -0.118 | -0.129 | -94.63 | -102.43 | 4 |
| 15 | 81.9 | 27 | 0 | 71.2 | 68.6 | 307.2 | 0.015 | 0.015 | 9.67 | 9.67 | 1 |
| 16 | 61.9 | 17 | 0 | 67.9 | 65.2 | 320.4 | 0.081 | -0.181 | 73.58 | -145.10 | 4 |

### 3.12.2 Detector evidence

While the FMM reconstruction uses $\sim 100 - -120$ Bragg peaks per orientation to reconstruct the crystal orientation field, it should be possible to locate twinning associated changes in scattering directly on detector images. Evidence is presented here through changes in $\{0002\}$ scattering since the c-axis, and there, this scattering, is reoriented through a large angle when twinning occurs. Note that if one mistakenly looked at the shared $\{10\bar{1}2\}$ scattering, there would be no changes associated with twinning since parent and twin share this scattering.

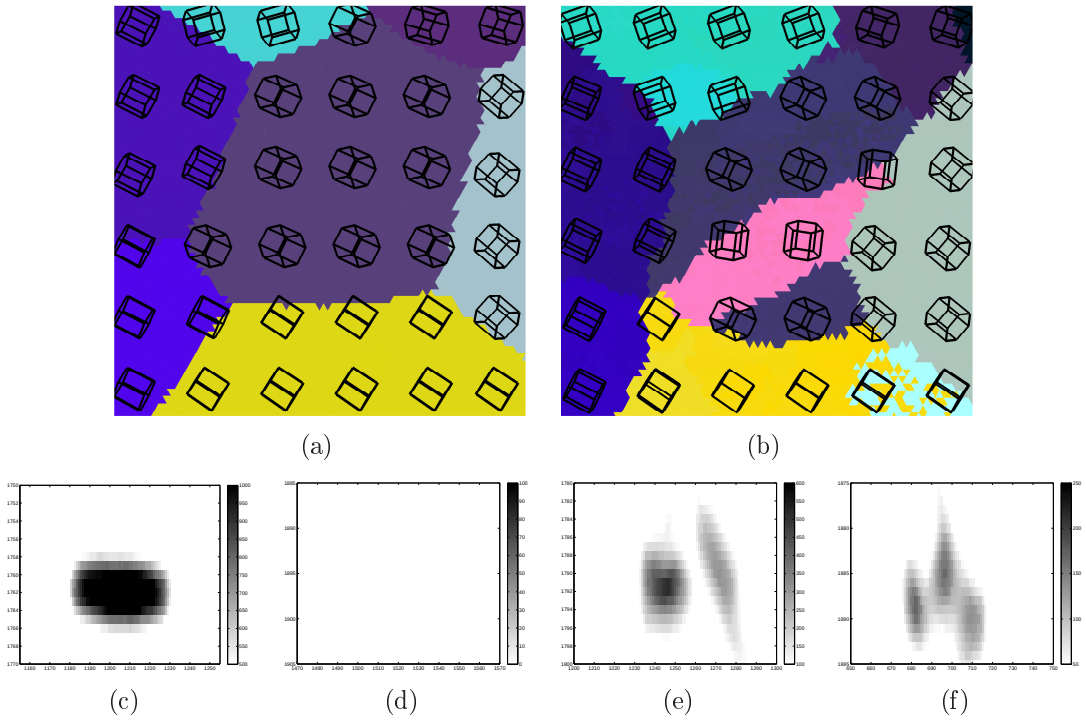


Figure 3.31: (a) and (a) shows $140\mu m \times 140\mu m$ region of the orientation map for the same grain cross-section in S0 and S2, respectively, with the pink region being a twin that is observed by S2. Black hexagons represent the orientation of the crystal lattice at various spatial locations. (c) and (e) show the same $\{0001\}$ scattering for the purple parent grain in S0 and S2, respectively. (d) and (f) shows the location where the $\{0002\}$ scattering for the pink twin is expected to be present in S0 and S2, respectively.

Figure 3.31 shows the appearance of $\{0002\}$ scattering from the newly formed twin where scattering was not previously observed. The absence of scattering in 3.31(d) implies the lack of this twin variant in S0 and the presence of this scattering in 3.31(f) directly validates the reconstruction of the pink twin. Further, the clear gap in $\{0002\}$ scattering in 3.31(e) indicates the absence of this scattering from the twinned part of

the parent. The origin of the apparent three regions of tin scattering in 3.31(f) is not clear at this time but may indicate a complex strain state.

### 3.12.3 Re-orientation of c-axis

From the initial IPF figure 3.3(d) for tensile twinning, those orientations with c-axis exactly aligned with the tensile direction will have greatest RSS on all of its twin variants. Activation of any of these variants will produce a twin with angle between c-axis and tensile axis, $\theta(c, TA)$, that is 85.2°. The parent which had an orientation unfavorable for prismatic slip, now has its twin oriented favorably for prismatic slip.

The texture evolution of HCP metals oriented for twinning show a complete rearrangement of {0001} texture. If entire volume has {0001} poles initially aligned with the tensile axis, after considerable deformation the entire volume is aligned mostly perpendicular to the tensile axis [71]. Tensile twinning tends to reorient the {0001} axes away from the tensile axis. In figure 3.31, $\theta(c, TA)$ for the parent grain is 55.5°, and $\theta(c, TA)$ for the twin is 72.1°.

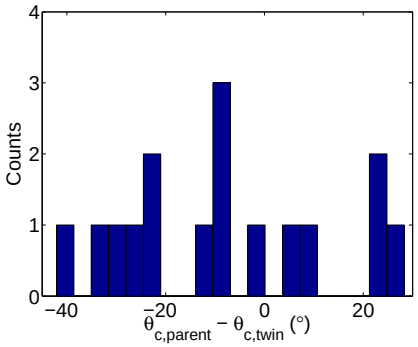


Figure 3.32: Histogrammed difference between $\theta(c, TA)$ for the parent and $\theta(c, TA)$ its twin in table 3.4 .

In the majority of the twin events observed, figure 3.32 shows that {0001} direction of the twinned volume has moved further away from the tensile axis than the parent, as is expected. The cases where angle decreased correspond to the entries in table 3.4 where $m_{sel} < 0$ and $RSS_{sel} < 0$. These twinning events are typically forbidden because they produce a shear strain opposite in sign to that favored by the external loading direction. These twin events must be driven by forces exerted by neighboring grains to due to their anisotropic properties.

## 3.13 Metrics for tendency of twins to nucleate

Schmid factors for twinning is a commonly computed to explain why certain grains twins. However owing to the sample's orientation texture, the largest Schmid factor

in all of the measured grains is $m = 0.31$. Thus, all observed twinning is in the "low Schmid factor" range. Table 3.4 and Fig. 3.33 show that, consistent with previous observations, [72, 73] the Schmid factor fails to predict the correct variant selection in roughly half the cases even allowing for the frequent parity between the first and second variants. Fig. 3.33(a) and (b) show that this remains the case whether we use the pristine state, S0, or the deformed state, S2, in which grains have been distorted and rotated and intra-granular orientation gradients have been established. Further, many grains with relatively high Schmid factors remain dormant and in some cases third and fourth ranked variants with negative factors become active.

Given that Schmid factor cannot alone predict the twinning that has been observed in this sample, twin plane RSS are calculated from the elastic FFT results. These stresses are used in an effort to account for local neighborhood effects. Local stresses computed from this model at each sample point allow for calculation of resolved-shear stresses,

$$RSS = \sum_{i,j} b_i \sigma_{ij} n_j \tag{3.5}$$

on all of the six available twin variant systems; $b_i$ and $n_j$ are the twin plane shear direction and twin plane normal for a particular system and $\sigma_{ij}$ is the local computed stress tensor. Table 3.4 indicates that this computation is qualitatively consistent with the Schmid factor analysis in the relative values of maximum and selected variant values. Fig 3.33(c) indicates the variation in computed $RSS$ within the twinning grains. These heterogeneities are not sufficient to re-order the stresses applied to the twin variant planes. Evidently, one has to resort to the *plastic* behavior of neighbor grains.

When a grain in a polycrystal undergoes slip, its neighbors must accommodate any deviations of the deformations from the polycrystal average, and this gives rise to complex and long range interactions. Given that the observed twins touch at least one neighbor grain, these cooperative effects between grains may be an important variable in determination of twin activity. This is supported by the observation that $N_{gb}$ and grain sizes shown in Table 3.4 tend to be larger for twinning grains than for the overall distribution in the measured volume [74]; the large neighbor number generates more opportunities for compatible slip-twin relations. Conversely, we observe four small grains, with radii near 30 $\mu m$, that have Schmid factors larger than any in Table 3.4 but that do not twin. In situations where a grain twins without being favorably oriented relative to the external load, (say, m $\lesssim 0.35$), neighborhood effects may well dominate as must also be the case for grains with higher Schmid factor that fail to twin [75].There exists little empirical evidence with which to quantify neighborhood effects because no measurement has characterized a complete neighborhood and then watched twin formation occur. Bulk texture measurements [71] observe macroscopic changes in c-axis orientation distributions associated with twinning but cannot identify specific grains or environments. Numerous surface studies using electron backscatter diffraction (EBSD) to map local crystal orientations have

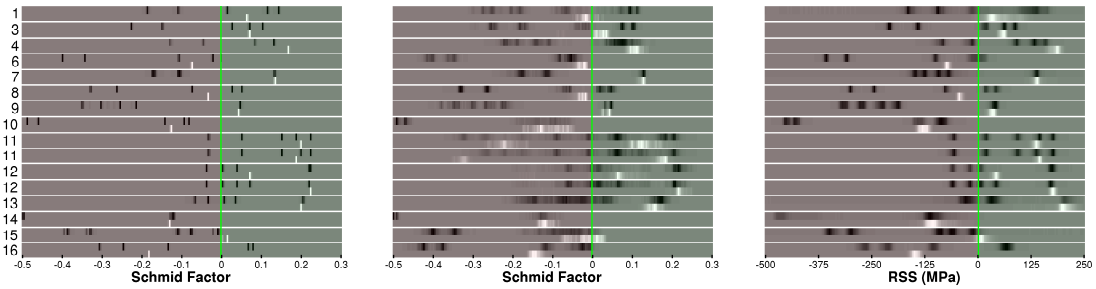


(a) (b) (c)

Figure 3.33: Grain orientation based predictions of twinning and twin variant selection. Horizontal rows correspond to those of Table 3.4. Green regions are favorable for twin formation while in the red regions the shear stress has the wrong sign. Observed variants are shown by white hash marks while others are shown in black. All results are computed on a voxel-by-voxel basis. (a) Schmid factors computed from the orientations in state S0; here, grain orientations are highly uniform so all voxels for a given grain yield essentially the same values. (b) Schmid factors computed from parent orientations in state S2 showing that deformation induced rotations and intragranular orientation variations do not strongly re-order the variants. (c) Resolved shear stresses in MPa obtained from a polycrystal elasticity computation based on the structure of S0. Inhomogeneous stresses again do not dramatically re-order the variants.

been performed but these lack neighborhood information below the surface, and the influence of the free surface on the transformation is unclear. Even dynamical experiments have been performed which allow the microstructure to evolve, but again EBSD can only capture the surface dynamics which could be very different from bulk response [76]. A recent hard X-ray measurement observed a twinning event that occurred inside of a bulk Mg sample, but did not resolve the microstructural neighborhood of the grain [77].

Moreover we observe coordinated deformation in numerous cases where the twins are large enough to produce observable effects in their neighbors. For example, consider grain 11 in Table 3.4 whose neighborhood is shown in Fig. 3.30. The maroon twin of interest appears geometrically coupled, in three dimensions, to a rotated region of a neighbor. The small angle boundary planes in the neighbor are roughly co-planar with the twin boundary plane in the central region of the twin seen in (c) - (g) and they extend across the entire neighbor. Note that, while the grains in Fig. 3.30 are neighbors in real space, their correlated features emerge from completely distinct sets of observed diffraction signals. To test for effects due to a single neighbor grain, analysis similar to that of Wang et al. [78] was performed by computing the geometric compatibility factor [79] between the active twin variant system and each of the possible slip modes in the correlated neighbor. A maximum value of 0.463 was

found indicating that this descriptor is also unable to fully capture the neighbor's influence on twin nucleation. A second example showing similar behavior is shown in [74].

Lattice compatibility calculations use the method shown in [78]. Given the variant that was selected in grain 11, the Luster-Morris parameter was computed for the prismatic ($\{10\bar{1}0\}\langle 11\bar{2}0\rangle$), basal($\{0001\}\langle 11\bar{2}0\rangle$), and pyramidal$\langle a\rangle$($\{10\bar{1}1\}\langle 11\bar{2}0\rangle$) slip modes in all of its neighbors. For the neighbor referenced in Fig. 3.30 as having roughly coplanar low-angle grain boundaries to the maroon variant twin plane, the highest m′ values were 0.416, 0.204, and 0.463, respectively for these sets of slip systems. None of these values are particular high since this indicator metric ranges from 0 to 1 with 1 being total alignment of the slip system from grain A with the twin system from grain B. For the other 18 neighbors, the highest m′ values were 0.877, 0.531, and 0.868; however, none of these high compatibility neighbors are in contact with the twinned region.

### 3.13.1 Twin growth

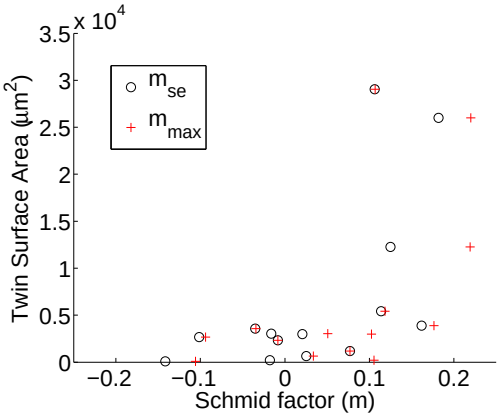


(a)

Figure 3.34: Surface area of the 14 tracked twins in S2 plotted against the selected and maximum Schmid factor variant.

### 3.13.2 Twinning discussion

Clearly, the current indicators for predicting twin activation (Schmid factor, elastic RSS, and single neighbor slip compatibility) do not perform adequately in cases where orientations are not favorable for twinning, i.e., low Schmid factor cases. It has been shown through current and former studies [75] that lower ranked variants are favored in this configuration, and we show that coupled deformation is observed in neighbors with low compatibility. This coupled deformation indicates that multiple neighbor

interactions need to be included in models of twin formation. We hypothesize that complete understanding will require the development and analysis of fully-coupled elasto-plastic full-field models that include slip-induced twinning and coupled plastic responses.

The nf-HEDM measurements presented here demonstrate the ability to track deformation and twin development in-situ and in three dimensions as tensile strain is applied to an initially well ordered Zr specimen. The results re-emphasize the need for such measurements since they indicate complex interactions in entire grain neighborhoods. Coupling these measurements with spatially resolved strain measurements as recently proposed in [53] or with far-field HEDM [80, 81, 82, 83] will offer a complete meso-scale characterization that can guide model development. Determining the influence of local microstructure on twinning is essential for prediction of overall material performance but it is only one example of the application of new non-destructive X-ray probes that can further our understanding of application critical materials responses.

## 3.14 Void formation

Finally, using the information in the tomographic reconstructions (section 3.10 and figure 3.21(b)), we can attempt to track locations of voids in the final S9 state back to earlier states in which HEDM reconstructions are possible. One can then look for correlations between void locations and various microstructural features; for example, specific grain orientations, grain boundary types, triple lines, or quadruple points. Preliminary analysis is presented here.

Once the layers of tomography have been aligned vertically, it becomes clear that the in-plane shape of the sample has drastically changed between the initial state and the final state. The overall trapezoidal cross-sectional shape of the sample remains the same but becomes compressed. To achieve estimates of locations in the initial orientation maps when voids will later occur, the tomography slices for a given matched cross-section are rescaled such that peak in the two absoption coefficient values are set to -1 and +1 for consistent thresholding. A convex hull on the sample perimeter is then defined from a binary thresholding of the image; this hull will provide the shape tracking back to the initial states. The outside of the sample is then flooded to match the binary values of the materials (1). The remaining pixels (voids) are run through a connected component analysis to define collections of connected pixels as a single void. These voids are located in the S9 state by their boundary pixel positions and void ID.

The convex hull from the tomography is then defined for all layers of tomography S0 through S9. An affine transformation is then determined between S9 and S8, which is then used to transform the voids to their estimated position ins S8. This process is repeated when going from S8 to S7, and so on. The iterative process proceeds until voids are tracked back to S0. The convex hull of the tracked layers through states is

seen in figure 3.21. Result of this back-tracking can be seen in figure 3.35.

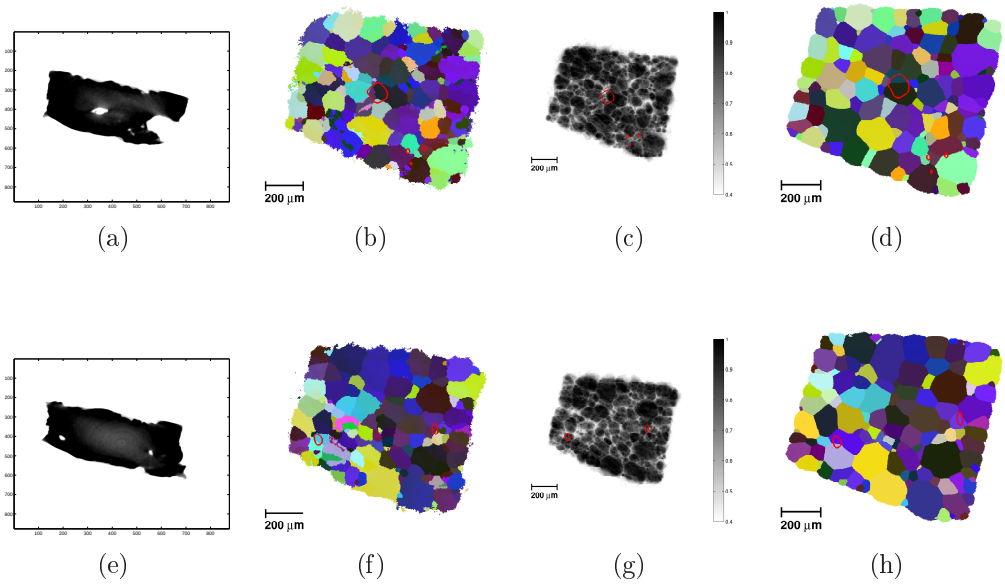


(a) (b) (c) (d)

(e) (f) (g) (h)

Figure 3.35: Two examples of void identification near the center of the tensile sample and tracking back to the states S0 and S2. (a) and (e) are tomography reconstructions for pixel rows 1530 and 1590 in S9, respectively. (b) and (f) are the orientation maps in S2 corresponding to (a) and (e) with transformed voids outlined in red. (c) and (g) are the confidence maps in S2. (d) and (h) are the orientation maps in S0.

One of the initial goals of this experiment was to pin-point where failure in ductile materials begin by comparing the inception of voids with respect to their placement in the microstructure. It appears that some of the larger voids are spatially nearer to regions where larger twins have formed. Whether the elevated stress state in parent grains that cannot be converted into larger twin volume fraction leads to void formation or the twin formation is a consequence of stress concentration in those regions cannot be determined from this experiment. These preliminary results do suggest a relationship between polycrystal failure and tensile twin formation in HCP zirconium.

## 3.15 Future work

There still exists considerable work that could be performed on the current experimental data to understand the grain deformation mechanics. The most straightforward would involve a crystal *plasticity* deformation simulation which incorporates the full geometry of the grains in the microstructure. This could be performed through vp-FFT or CP-FEM. This would enable one to search for stress "hot spots" that might

correlate with unexpected twin formation or void formation. The crystal plasticity simulation would also afford direct point-by-point comparison of simulated slip activity compared with experimental slip activity seen through CRA analysis. Further, a higher resolution reconstruction to the S3 state would allow the study of twin growth. Also, given the regular polygonal shapes

These results represent some observations on the deformation mechanisms of this particularly textured sample of zirconium from initially undeformed state to a later largely deformed state with no intermediate measurement. This study represents a single data point in a vast space of sample processing (sample material, texture, strain steps, etc). Future studies should involve multiple samples with varied initial textures. Each of these proposed measurements should be performed with larger volumes and through smaller strain steps to better match step-by-step with coupled simulations. This will serve to validate and constrain simulations. Experimentally resolved grain stresses should also be incorporated into future measurement through either nf-HEDM strain fitting or combined measurement with far-field HEDM (ff-HEDM).

While these suggestions appear unrealistic given usual experiment beam time constraints, current improvements at the nf-HEDM setup at APS-1ID-B and APS-1ID-E are being made to increase data collection speed by orders of magnitude. Combined nf-HEDM and ff-HEDM experiments have already been successfully performed by Air Force Research Laboratory (AFRL) led group (including AFRL, APS, CMU, LLNL) within the past year. The incorporation of continuous sweep data collection has already been implemented which has lead to a 2x speedup. Proposed multi-scintillator screen and muti-detector systems would create another 2x speedup. Planned APS upgrade includes the installation of a superconducting undulator at 1-ID which will increase the photon flux by 10x or more. Another part of the APS upgrade involves the increase in electron beam current from 100mA to 200mA will also lead to 2x increased photon generation. These current and soon-to-be realized improvements will drastically increase the output potential of measurement volumes with nf-HEDM making a detailed database of microstructures possible.

## 3.16 Conclusion and Discussion

In this chapter, preparation for an in-situ micro uni-axial tensile experiment on polycrystalline zirconium was discussed and results are presented. The development of the nf-HEDM compatible tensile apparatus was described. The experimental proceedure was detailed as well some analysis required to reduce the microstructure data into manageable form. Coarse grain statistics were presented as well as initial texture measurement.

The remainder involved describing the evolution of the microstructure and shape of the tensile sample. The sample response was compared against expected phenomenology and against both computation simulations and expected single crystal behavior. Experimentally measured grain rotation was compared with a mean-field

plasticity model resulting in limited correspondence. An elastic simulation was presented involving the full geometry of the microstructure which was hoped to provide accurate stress states in each grain that varied from the macroscopic stress state. The simulated stress would explain unexpected phenomena later described in the twinning section. Strain evolution through tomographic data was analyzed and the sample shape change development was interpreted as a consequence of initial texture.

Deformation of the sample was described by evidence for slip activation, twin nucleation, and void formation. The active slip systems in HCP zirconium were presented, as well as evidence for slip bands in the FMM reconstruction, and consistent overall grain rotation of the sample due to expected slip. Twin nucleation was also observed with consistent shape and crystallography. The twin variants observed were compared against a simple Schmid factor approach, resolved shear-stresses from the elastic simulation, and comparison with a neighbor induced nucleation theory. In many of these cases, none of these explanations were sufficient to explain why the variants that formed did so. Finally, initial attempts were made to back-track voids found through tomography in later strain states to their placement in the initial unstrained microstructure. There appears to be some correspondence between location of large voids and twins. Ideas for future work with this dataset and proposed experiments were made.

The results presented here represent the first attempt at studies of polycrystalline HCP metals using nf-HEDM. A considerable amount of experimental and computational development was required to get this far in the microstructural analysis. Moreover, the lack of textbook problem/solutions, general rules of thumb, and described intuition that exist for fcc systems required hard fought solutions to be generated, rules of thumb produced, and intuition gained through much investigation. This was even further complicated by the fact that the system did not always behave the way one might expect it to, and this required much thought and reconciliation with those facts. The single direction compression shape change of the sample, for example, was a fact that mystified the author for quite a while. At this point, a body of knowledge as well as code has been developed that allows for interpretation and data mining of HCP microstructures at an equal level available for FCC microstructures.

The dearth of mechanical studies in HCP metals is most likely related to their anisotropy and scarcity. The somewhat unpredictable response of hexagonals is one reason for their limited use today. Only with advanced understanding and research in their complex response to applied stresses at the mesoscale will their anisotropy be seen as an engineering advantage. Unfortunately the lack of confidence in modeling their response is currently seen as a liability. The ability to develop so-called n̈ext generationm̈aterials requires them to have unique properties that can be utilized when properly understood. For structural/mechanical materials, this will almost definitely require them to be lower-symmetry metals. Further efforts in understanding other HCP metals, such as titanium and magnesium, are already currently underway. Building reliable predictive models will require experimental validation with full char-

acterization in the form of variables the simulation can compare against, i.e. local lattice information, stress tensor, grain boundary plane inclination, shape change, etc. Only through further study of can the underlying mechanism of deformation in the bulk of polycrystalline HCP metals understood.

# Chapter 4

# Conclusion

The following final pages are meant to summarize the main results presented here and give an outlook on future research.

## 4.1 Recap & interpretation

Chapter 2 introduced the importance of image processing to the nf-HEDM data pipeline. The need for stable, robust signal extraction was argued. The original image processing algorithm applied to these diffraction images was presented and examples shown for clarification. Its recent short-comings were revealed through the development and testing of the whole nf-HEDM technique by looking at varied types of microstructures (fine-grained, larger volumes, plastically deformed, etc). Given the image processing is the first level of data processing in the pipeline, the types of errors and how they might affect the outcome from the FMM was discussed. The requirements for a new approach to data processing was listed, and the Laplacian of Gaussians (LoG) zero-cross edge detection algorithm was offered an algorithm that could fulfill those requirements. Its implementation was described in detail, and the remaining parts of the chapter presented the differences between the two methods in signal extraction and its result on FMM reconstruction. The stability of peak extraction versus reduction parameter was shown. Comparison of the results for a single image was presented to see the difference in output between the two algorithms. This is done to appeal to the human eye and brain which are extremely good at segmenting visual information. A 1D illustration of the LoG algorithm was given for demonstration. Through a series of FMM microstructure comparisons, it is shown that for the LoG method applied to the FMM, 1) grain boundary sensitivity is improved, 2) reconstructability of deformed microstructures increases, 3) the shapes of boundaries match physical expectation better, 4) there is evidence for improved spatial resolution, 5) the orientation resolution in finer, and 6) the variability in reconstruction as reduction parameters is greatly reduced. This chapter presents a significant improvement of the nf-HEDM technique by examining and confirming the improved fidelity

of FMM results when stable peak information is provided by the LoG method of data reduction.

The next chapter (3), presented the results from the first in-situ plastic strain measurement of an HCP metal (zirconium) using nf-HEDM. Its main signatures of plastic deformation, slipping and tensile twinning, were compared against both simulations and single crystal behavior. Moderate agreement existed in the case of slip, but the previously proposed mechanism for tensile twinning did not match the experimental results. Development of the experimental apparatus and sample preparation was presented. Software required for tracking the microstructure features across strain states in a meaningful way was explained. Texture characterization confirmed the rolling texture of the sample, and shape change as seen through absorption tomography of the gauge section witness the compression of the sample most likely due to heavy prismatic slip activation. Lattice rotations due to slip is discussed and its comparison made with the VPSC simulation. An example of the ability to resolve prismatic slip bands was shown. Observation of multiple bulk tensile twinning events is characterized. Finally an attempt is made to track voids found in later strain states via x-ray absoption tomography to the initial measured microstructure in S0–S3.

This thesis represents both the advancement of the nf-HEDM technique and detailed characterization of plastic deformation using it. The image processing chapter was completely necessary for observations obtained in the zirconium deformation chapter. Both appealed to physically relevant phenomena to reassure that results from software and experiment were in good agreement with expected physical phenomena ($\Sigma 3$ boundaries, slip band shape and rotation axis, tensile twin boundaries). This thesis represents pushing of the boundary of the technique both in resolution (chapter 2)and in scientific scope (chapter 3).

## 4.2 Future Outlook

As further experiments such as these become more commonplace, many questions still remain. One involves how the technique needs to evolve further. Another would be what scientific boundaries can be pushed currently and in the future.

On the issue of technique development, in the near future, $mm^3$ volumes of bulk microstructures will be able to to be mapped routinely in a semi-automated way. The nf-HEDM technique will serve as a scientific tool of discovery for researchers requiring studies of bulk dynamics. Integration of nf-HEDM with ff-HEDM is currently underway to infuse spatially resolved orientations with grain-average stress information. Further, experiments are being performed to attempt to incorporate spatially resolved strain information from nf-HEDM measurements directly. Hardware upgrades at APS will improve spatial resolution of the technique and also increase volume sizes that can be probed. Fusion with tomographic and potentially phase-contrast tomography could add even further layers of characterization to measured samples.

The other main question revolves around what important scientific results can be

obtained. Increases in experimental data collection will either lead to being overwhelmed in data or development of reducing microstructures to meaningful representative forms for comparison. The incorporation of stress information into the spatially resolved microstructure will allow for unprecedented statistics to be compiled on bulk twin nucleation, for instance. Full plasticity, either FFT or FEM, models will be able to be checked step-by-step in 3D during deformation experiments. This will lead to direct validation of models, invalidation of models, or elucidate changes that are required. Crack initiation or void formation will be predictable events, and metal processing methods will be developed to minimize microstructures with less desirable weak links.

Until a complete research center is created to advance this type of materials characterization, it will be necessary for students in the future to be pushing both boundaries, experimental technique and microstructure scientific exploration. Appreciation for having a scientific result in context is just as necessary as understanding the limit of the experiment technique. If these two components become separated, the entire endeavor will be lost in a sea of misunderstanding. If dual core expertise continues, new science will be unlocked.

# Bibliography


[1] Derek R Ney, Elliot K Fishman, Donna Magid, Douglas D Robertson, Akira Kawashima, et al. Three-dimensional volumetric display of CT data: effect of scan parameters upon image quality. *Journal of computer assisted tomography*, 15(5):875, 1991.

[2] R M Suter, D. Hennessy, C. Xiao, and U. Lienert. Forward modeling method for microstructure reconstruction using X-ray diffraction microscopy: Single-crystal verification. *Rev. Sci. Instr.*, 77(12):123905–123905, 2006.

[3] S F Li and R M Suter. Adaptive reconstruction method for three-dimensional orientation imaging. *J. Appl. Crystallogr.*, 46(2):512–524, 2013.

[4] W. Ludwig, P. Reischig, A. King, M. Herbig, E M Lauridsen, G. Johnson, T J Marrow, and J. Y. Buffiere. Three-dimensional grain mapping by x-ray diffraction contrast tomography and the use of Friedel pairs in diffraction data analysis. *Rev. Sci. Instr.*, 80(3):033905–033905, 2009.

[5] Henning Friis Poulsen. *Three-dimensional X-ray diffraction microscopy: mapping polycrystals and their dynamics*, volume 205. Springer, 2004.

[6] M P Miller, J. S. Park, P R Dawson, and T. S. Han. Measuring and modeling distributions of stress state in deforming polycrystals. *Acta Mat.*, 56(15):3927–3939, 2008.

[7] Abraham Taylor and M Sc. *X-ray Metallography*. Wiley New York, 1961.

[8] Bulent Sankur and Mehmet Sezgin. Image thresholding techniques: A survey over categories. *Pattern Recognition*, 34(2):1573–1583, 2001.

[9] Milan Sonka, Vaclav Hlavac, Roger Boyle, et al. Image processing, analysis, and machine vision. 1999.

[10] John Canny. A computational approach to edge detection. *Pattern Analysis and Machine Intelligence, IEEE Transactions on*, (6):679–698, 1986.

[11] Mohsen Sharifi, Mahmoud Fathy, and Maryam Tayefeh Mahmoudi. A classified and comparative study of edge detection algorithms. In *Information Technology: Coding and Computing, 2002. Proceedings. International Conference on*, pages 117–120. IEEE, 2002.

[12] David Marr and Ellen Hildreth. Theory of edge detection. *Proceedings of the Royal Society of London. Series B. Biological Sciences*, 207(1167):187–217, 1980.

[13] Luis Ibanez, William Schroeder, Lydia Ng, and Josh Cates. The itk software guide. 2003.

[14] William Gropp, Ewing L Lusk, and Anthony Skjellum. *Using MPI-: Portable Parallel Programming with the Message Passing Interface*, volume 1. MIT press, 1999.

[15] David L Olmsted, Stephen M Foiles, and Elizabeth A Holm. Survey of computed grain boundary properties in face-centered cubic metals: I. grain boundary energy. *Acta Materialia*, 57(13):3694–3703, 2009.

[16] Diana Farkas, Eduardo Bringa, and Alfredo Caro. Annealing twins in nanocrystalline fcc metals: A molecular dynamics simulation. *Physical Review B*, 75(18):184111, 2007.

[17] Gregory S Rohrer. The distribution of grain boundary planes in polycrystals. *JOM*, 59(9):38–42, 2007.

[18] C M Hefferan, S F Li, J. Lind, U. Lienert, A D Rollett, P. Wynblatt, and R M Suter. Statistics of high purity nickel microstructure from high energy X-ray diffraction microscopy. *Comput., Mat., & Continua*, 14(3):209–220, 2010.

[19] C. M. Hefferan. *Measurement of Annealing Phenomena in High Purity Metals with Near-field High Energy X-ray Diffraction Microscopy*. PhD thesis, Carnegie Mellon University, 2012.

[20] V Randle. Mechanism of twinning-induced grain boundary engineering in low stacking-fault energy materials. *Acta materialia*, 47(15):4187–4196, 1999.

[21] S F Li, J. Lind, C M Hefferan, R. Pokharel, U. Lienert, A D Rollett, and R M Suter. Three-dimensional plastic response in polycrystalline copper via near-field high-energy X-ray diffraction microscopy. *J. Appl. Crystallogr.*, 45(6):0–0, 2012.

[22] S. F. Li. *Imaging of Orientation and Geometry in Microstructures/ Development and Applications of High Energy X-ray Diffraction Microscopy*. PhD thesis, CARNEGIE MELLON UNIVERSITY, 2011.

[23] B.S El-Dasher, B.L Adams, and A.D Rollett. Viewpoint: experimental recovery of geometrically necessary dislocation density in polycrystals. *Scripta Materialia*, 48(2):141 – 145, 2003.

[24] S.K. Mishra, P. Pant, K. Narasimhan, A.D. Rollett, and I. Samajdar. On the widths of orientation gradient zones adjacent to grain boundaries. *Scripta Materialia*, 61(3):273 – 276, 2009.

[25] Y. Huang and F.J. Humphreys. Subgrain growth and low angle boundary mobility in aluminium crystals of orientation 110ãĂĹ001ãĂĽ. *Acta Materialia*, 48(8):2017 – 2030, 2000.

[26] D.P. Field, P.B. Trivedi, S.I. Wright, and M. Kumar. Analysis of local orientation gradients in deformed single crystals. *Ultramicroscopy*, 103(1):33 – 39, 2005. <ce:title>Proceedings of the Ninth Conference on Frontiers of Electron Microscopy in Materials Science</ce:title>.

[27] Luke N Brewer, David P Field, and Colin C Merriman. Mapping and assessing plastic deformation using ebsd. In *Electron backscatter diffraction in materials science*, pages 251–262. Springer, 2009.

[28] Frank J Massey Jr. The kolmogorov-smirnov test for goodness of fit. *Journal of the American statistical Association*, 46(253):68–78, 1951.

[29] C. M. Hefferan, J. Lind, S. F. Li, U. Lienert, A. D. Rollett, and R. M. Suter. Observation of recovery and recrystallization in high-purity aluminum measured with forward modeling analysis of high-energy diffraction microscopy. *Acta Mat.*, 60(10):4311–4318, 2012.

[30] William Shockley et al. *Electrons and holes in semiconductors*, volume 1. van Nostrand, 1963.

[31] Erich Tenckhoff. *Deformation mechanisms, texture, and anisotropy in zirconium and zircaloy*, volume 966. ASTM International, 1988.

[32] Ricardo A Lebensohn, Anthony D Rollett, and Pierre Suquet. Fast fourier transform-based modeling for the determination of micromechanical fields in polycrystals. *JOM*, 63(3):13–18, 2011.

[33] Ricardo A Lebensohn, Renald Brenner, Olivier Castelnau, and Anthony D Rollett. Orientation image-based micromechanical modelling of subgrain texture evolution in polycrystalline copper. *Acta materialia*, 56(15):3914–3926, 2008.

[34] AK Kanjarla, RA Lebensohn, L Balogh, and CN Tomé. Study of internal lattice strain distributions in stainless steel using a full-field elasto-viscoplastic formulation based on fast fourier transforms. *Acta Materialia*, 60(6):3094–3106, 2012.

[35] Erich Schmid, Walter Boas, and FIG Rawlins. Kristallplastizität. *J. Phys. Chem.*, 39(9):1248–1248, 1935.

[36] EO Hall. The deformation and ageing of mild steel: Iii discussion of results. *Proceedings of the Physical Society. Section B*, 64(9):747, 1951.

[37] N. J. Petch. *J. and Iron Steel*, 173:25, 1953. Cited By (since 1996):1.

[38] Rob Phillips. *Crystals, defects and microstructures: modeling across scales*. Cambridge University Press, 2001.

[39] Geoffrey Ingram Taylor and H Quinney. The plastic distortion of metals. *Philosophical Transactions of the Royal Society of London. Series A, Containing Papers of a Mathematical or Physical Character*, 230:323–362, 1932.

[40] Geoffrey Ingram Taylor. The mechanism of plastic deformation of crystals. part i. theoretical. *Proceedings of the Royal Society of London. Series A, Containing Papers of a Mathematical and Physical Character*, 145(855):362–387, 1934.

[41] G Sachs. Plasticity problems in metals. *Transactions of the Faraday Society*, 24:84–92, 1928.

[42] JFW Bishop and Rodney Hill. Cxxviii. a theoretical derivation of the plastic properties of a polycrystalline face-centred metal. *Philosophical Magazine Series 7*, 42(334):1298–1307, 1951.

[43] A. D. Rollett. Texture, microstructure, & anisotropy lectures, 2011.

[44] F Roters, P Eisenlohr, L Hantcherli, DD Tjahjanto, TR Bieler, and D Raabe. Overview of constitutive laws, kinematics, homogenization and multiscale methods in crystal plasticity finite-element modeling: Theory, experiments, applications. *Acta Materialia*, 58(4):1152–1211, 2010.

[45] Miklós Tisza. *Physical metallurgy for engineers*. ASM International, 2001.

[46] Hibbett, Karlsson, Sorensen, and Hibbitt. *ABAQUS/standard: User's Manual*, volume 1. Hibbitt, Karlsson & Sorensen, 1998.

[47] FPE Dunne, A Walker, and D Rugg. A systematic study of hcp crystal orientation and morphology effects in polycrystal deformation and fatigue. *Proceedings of the Royal Society A: Mathematical, Physical and Engineering Science*, 463(2082):1467–1489, 2007.

[48] Brent L Adams, Stuart I Wright, and Karsten Kunze. Orientation imaging: the emergence of a new microscopy. *Metallurgical Transactions A*, 24(4):819–831, 1993.

[49] Do J Dingley and V Randle. Microtexture determination by electron back-scatter diffraction. *Journal of Materials Science*, 27(17):4545–4566, 1992.

[50] Anthony D Rollett, S-B Lee, R Campman, and GS Rohrer. Three-dimensional characterization of microstructure by electron back-scatter diffraction. *Annu. Rev. Mater. Res.*, 37:627–658, 2007.

[51] L Margulies, G Winther, and HF Poulsen. In situ measurement of grain rotation during deformation of polycrystals. *Science*, 291(5512):2392–2394, 2001.

[52] A. King, G. Johnson, D. Engelberg, W. Ludwig, and J. Marrow. Observations of intergranular stress corrosion cracking in a grain-mapped polycrystal. *Science*, 321(5887):382–385, 2008.

[53] L. Balogh, S. R. Niezgoda, A. K. Kanjarla, D. W. Brown, B. Clausen, W. Liu, and C. N. TomÃľ. Spatially resolved in situ strain measurements from an interior twinned grain in bulk polycrystalline AZ31 alloy. *Acta Mater.*, 61(10):3612 – 3620, 2013.

[54] R. Pokharel. *Spatially Resolved In-situ Study of Plastic Deformation in Polycrystalline Cu using High Energy X-Rays and Full-field Simulations*. PhD thesis, Carnegie Mellon University, 2013.

[55] FJ Humphreys. Selected areas of electron diffraction. *Textures and Microstructures*, 6:45–62, 1983.

[56] Ryong-Joon Roe. Description of crystallite orientation in polycrystalline materials. iii. general solution to pole figure inversion. *Journal of Applied Physics*, 36(6):2024–2031, 1965.

[57] MP Miller, JV Bernier, J-S Park, and A Kazimirov. Experimental measurement of lattice strain pole figures using synchrotron x rays. *Review of scientific instruments*, 76(11):113903–113903, 2005.

[58] Joel V Bernier and Matthew P Miller. A direct method for the determination of the mean orientation-dependent elastic strains and stresses in polycrystalline materials from strain pole figures. *Journal of applied crystallography*, 39(3):358–368, 2006.

[59] U Fred Kocks, Carlos Norberto Tomé, and H R Wenk. *Texture and anisotropy: preferred orientations in polycrystals and their effect on materials properties*. Cambridge University Press, 2000.

[60] Y N Wang and J C Huang. Texture analysis in hexagonal materials. *Mat. Chem. Phys.*, 81(1):11–26, 2003.

[61] JK Mackenzie. Second paper on statistics associated with the random disorientation of cubes. *Biometrika*, 45(1-2):229–240, 1958.

[62] A Morawiec. Misorientation-angle distribution of randomly oriented symmetric objects. *Journal of applied crystallography*, 28(3):289–293, 1995.

[63] RA Lebensohn and CN Tomé. A self-consistent anisotropic approach for the simulation of plastic deformation and texture development of polycrystals: application to zirconium alloys. *Acta Metallurgica et Materialia*, 41(9):2611–2624, 1993.

[64] Stanley Roderick Deans. *The Radon transform and some of its applications*. DoverPublications. com, 2007.

[65] Marion Calcagnotto, Dirk Ponge, Eralp Demir, and Dierk Raabe. Orientation gradients and geometrically necessary dislocations in ultrafine grained dual-phase steels studied by 2d and 3d ebsd. *Materials Science and Engineering: A*, 527(10):2738–2746, 2010.

[66] D. G. Westlake. Twinning in zirconium. *Acta Metall.*, 9, 1961.

[67] J. W. Christian and S. Mahajan. Deformation twinning. *Prog. Mat. Sci.*, 39(1):1–157, 1995.

[68] William F Hosford. *Mechanical behavior of materials*. Cambridge University Press, 2005.

[69] M. R. Barnett, Zohreh Keshavarz, A. G. Beer, and Xiang Ma. Non-Schmid behaviour during secondary twinning in a polycrystalline magnesium alloy. *Acta Mater.*, 56(1):5–15, 2008.

[70] Étienne Martin, L Capolungo, L Jiang, and John J Jonas. Variant selection during secondary twinning in Mg–3% Al. *Acta Mater.*, 58(11):3970–3983, 2010.

[71] D. W. Brown, S. R. Agnew, M. A. M. Bourke, T. M. Holden, S. C. Vogel, and C. N. Tomé. Internal strain and texture evolution during deformation twinning in magnesium. *Mat. Sci. Eng. A*, 399(1):1–12, 2005.

[72] Hamidreza Abdolvand and Mark R Daymond. Multi-scale modeling and experimental study of twin inception and propagation in hexagonal close-packed materials using a crystal plasticity finite element approach; Part I: Average behavior. *J. Mech. Phys. Solids*, 2012.

[73] J. J. Jonas, S. Mu, T. Al-Samman, G. Gottstein, L. Jiang, and Ė. Martin. The role of strain accommodation during the variant selection of primary twins in magnesium. *Acta Mater.*, 59(5):2046–2056, 2011.

[74] Information on materials and methods is available on Science Online.

[75] I. J. Beyerlein, L. Capolungo, P. E. Marshall, R. J. McCabe, and C. N. Tomé. Statistical analyses of deformation twinning in magnesium. *Philos. Mag.*, 90(16):2161–2190, 2010.

[76] Asmahana Zeghadi, Franck N'guyen, Samuel Forest, A F Gourgues, and Olivier Bouaziz. Ensemble averaging stress–strain fields in polycrystalline aggregates with a constrained surface microstructure–Parts 1 & 2. *Philos. Mag.*, 87(8-9):1401–1446, 2007.

[77] C. C. Aydïner, J. V. Bernier, B. Clausen, U. Lienert, C. N. Tomé, and D. W. Brown. Evolution of stress in individual grains and twins in a magnesium alloy aggregate. *Phys. Rev. B*, 80(2):024113, 2009.

[78] L. Wang, Y. Yang, P. Eisenlohr, T R Bieler, M A Crimp, and D E Mason. Twin nucleation by slip transfer across grain boundaries in commercial purity titanium. *Metall. Mat. Trans. A*, 41(2):421–430, 2010.

[79] J Luster and M A Morris. Compatibility of deformation in two-phase Ti-Al alloys: Dependence on microstructure and orientation relationships. *Metall. Mat. Trans. A*, 26(7):1745–1756, 1995.

[80] U. Lienert, S F Li, C M Hefferan, J. Lind, R M Suter, J V Bernier, N R Barton, M C Brandes, M J Mills, M P Miller, et al. High-energy diffraction microscopy at the Advanced Photon Source. *JOM*, 63(7):70–77, 2011.

[81] J. V. Bernier, N. R. Barton, U. Lienert, and M. P. Miller. Far-field high-energy diffraction microscopy: a tool for intergranular orientation and strain analysis. *J. Strain Analysis for Eng. Design*, 46(7):527–547, 2011.

[82] A J Beaudoin, M Obstalecki, W Tayon, M Hernquist, R Mudrock, P Kenesei, and U Lienert. In situ assessment of lattice strain in an Al–Li alloy. *Acta Mater.*, 61(9):3456 – 3464, 2013.

[83] J Oddershede, B Camin, S Schmidt, L P Mikkelsen, H O Sørensen, U Lienert, H F Poulsen, and W Reimers. Measuring the stress field around an evolving crack in tensile deformed Mg AZ31 using three-dimensional X-ray diffraction. *Acta Mat*, 60(8):3570–3580, 2012.